

Catalytic Effects of Electrodes and Electrolytes in Metal–Sulfur Batteries: Progress and Prospective

Linchao Zeng, Jianhui Zhu, Paul K. Chu, Licong Huang, Jiahong Wang, Guangmin Zhou,* and Xue-Feng Yu*

Metal–sulfur (M–S) batteries are promising energy-storage devices due to their advantages such as large energy density and the low cost of the raw materials. However, M–S batteries suffer from many drawbacks. Endowing the electrodes and electrolytes with the proper catalytic activity is crucial to improve the electrochemical properties of M–S batteries. With regard to the S cathodes, advanced electrode materials with enhanced electrocatalytic effects can capture polysulfides and accelerate electrochemical conversion and, as for the metal anodes, the proper electrode materials can provide active sites for metal deposition to reduce the deposition potential barrier and control the electroplating or stripping process. Moreover, an advanced electrolyte with desirable design can catalyze electrochemical reactions on the cathode and anode in high-performance M–S batteries. In this review, recent progress pertaining to the design of advanced electrode materials and electrolytes with the proper catalytic effects is summarized. The current progress of S cathodes and metal anodes in different types of M–S batteries are discussed and future development directions are described. The objective is to provide a comprehensive review on the current state-of-the-art S cathodes and metal anodes in M–S batteries and research guidance for future development of this important class of batteries.

1. Introduction


The development and progress of the modern society depends on clean and safe energy. However, supply of fossil fuels is limited and burning of fossil fuels emits pollutants that can cause global climate change. Therefore, alternative energy resources are urgently needed. There are different clean energy sources such as wind energy, tidal energy, and hydrogen energy, but their use is still limited in comparison with fossil fuels and furthermore, the proper energy-storage devices (ESDs) are required to store the energy generated by these green techniques.^[1] For example, Li-ion batteries (LIBs), which were commercialized by Sony Corporation in 1991, are the most widely used ESDs for portable electronics due to relative high energy density, absence of memory effects, and long cycling life.^[2]

However, due to the limited specific capacity of traditional cathode materials and the lack of Li resources, LIBs are increasingly unable to meet the requirements of high energy density and low price of energy-storage equipment in application scenarios. Therefore, other energy-storage systems with promising applications need to be further developed. So far, scientists have studied and developed a wide variety of batteries (e.g., sodium-ion batteries (NIBs), potassium-ion batteries (KIBs), and zinc-ion batteries (ZIBs)), and every kind of batteries have their own advantages. Compared to the “all-in-one-battery,” which boasts all merits (e.g., safety, durability, and low cost), the proper ESDs catered to specific applications appear to be more practical.^[3] Among the different types of ESDs, batteries composed of metal anodes and sulfur (S) cathodes have attracted great attention. S has many advantages.^[1] First of all, S is an earth-abundant element and exists as a solid at room temperature. Therefore, metal–S (M–S) batteries can be assembled relatively easily and economically. Second, S possesses high gravimetric specific capacity of 1672 mAh g⁻¹, which is larger than those of selenium (678 mAh g⁻¹) and tellurium (419 mAh g⁻¹). Thirdly, M–S batteries can be assembled in a closed configuration which is safer in terms of electrolyte loss. Fourthly, metal anodes possess many advantages including the high theoretical specific capacity (theoretical specific capacity of

L. Zeng, J. Zhu, L. Huang, J. Wang, X.-F. Yu
Materials Interfaces Center
Shenzhen Institute of Advanced Technology
Chinese Academy of Sciences
Shenzhen 518055, P. R. China
E-mail: xf.yu@siat.ac.cn

P. K. Chu
Department of Physics
Department of Materials Science and Engineering
and Department of Biomedical Engineering
City University of Hong Kong
Tat Chee Avenue, Kowloon, Hong Kong 999077, P. R. China

G. Zhou
Shenzhen Geim Graphene Center
Tsinghua-Berkeley Shenzhen Institute & Tsinghua Shenzhen
International Graduate School
Tsinghua University
Shenzhen 518055, P. R. China
E-mail: guangminzhou@sz.tsinghua.edu.cn

 The ORCID identification number(s) for the author(s) of this article can be found under <https://doi.org/10.1002/adma.202204636>.

DOI: 10.1002/adma.202204636

Li is 3861 mAh g⁻¹, which is more than 10 times larger than that of commercial graphite anode), large specific energy density, and small charging/discharging potentials.^[4]

So far, only high-temperature sodium–sulfur (HT Na–S) batteries have been used in commercial applications because of the high energy density, good cyclic stability, and low material cost.^[2b,5] HT Na–S batteries use ceramic materials as the electrolytes (NaAl₁₁O₁₇, β-alumina) and operate at a high temperature (more than 300 °C) in order to overcome the shuttle effect of intermediate products and slow reaction kinetics of S. However, the high operating temperature of HT Na–S batteries consume energy and are prone to safety problems. Owing to the low Na melting point (98 °C) and S melting point (115 °C), they become liquids at the high operating temperature and can even corrode the other components in HT Na–S batteries as well.^[6] HT Na–S batteries store energy by the following reaction^[7]



In this case, the final discharge product of the HT Na–S batteries is Na₂S₃ instead of Na₂S and therefore, it cannot be fully utilized.

Room temperature (RT) M–S batteries consisting of a liquid electrolyte are an emerging area in energy storage, as shown in **Table 1**.^[8] For instance, lithium–sulfur (Li–S) batteries have been widely investigated. The major advance of Li–S batteries is the use of the uniform CMK-3/S composite in 2009.^[6] The melted S infiltrates into the channels via the capillary force and then solidifies and contracts to form S nanofillers that are in close contact with the conductive carbon walls. This strategy has also been adopted by other RT alkali-metal batteries like Na–S, and potassium–sulfur (K–S) batteries.^[9] Compared to alkali-metal anodes, the multivalence metal anodes have higher capacity (theoretical specific capacity of magnesium (Mg) is 2205 mAh g⁻¹ and larger than that of Li) and better safety. This has spurred the development of batteries coupling alkali earth metals or transition metal anodes with S cathodes (e.g., aluminum–sulfur (Al–S), calcium–sulfur (Ca–S), and Mg–S batteries) (**Figure 1**).^[10] However, there are still some challenges as follow impede the applications of M–S batteries. First, the poor electrical conductivity and sluggish reactivity of S result in low utilization of the active electrode materials. Second, the intermediate products of long-chain polysulfides diffuse across the electrolytes to the metal anodes to initiate a redox reaction that causes fast capacity fading.^[11] Third, the large volume change of the cathodes/anodes during charging/discharging can cause early failure. Fourth, metal dendrites formed by uneven deposition processes on the metal anode during electrochemical cycling can penetrate the separator causing failure or even fire. Fifth, the multivalence metal ions are incompatible with conventional organic liquid electrolytes in alkali M–S batteries.^[1]

A widely used strategy is to introduce porous carbon materials as the hosts of S to inhibit diffusion of the polysulfide intermediates by exploiting the physical adsorption effects on the porous carbon matrix. The excellent electrical conductivity of the porous carbon matrix also provides excellent electron/ion conduction channels for the S cathodes and the porous carbon network buffers the volume change of S during charging/discharging to improve the stability. As for metal anodes, the 3D porous framework as the hosts and collectors is effective in

buffering the volume change of the metal anodes during cycling. The large specific surface area also facilitates uniform deposition of the metal, although metal dendrites are still formed during electroplating/stripping. Another common strategy to address dendrite formation on the metal anodes is to construct a robust artificial solid-electrolyte interface (SEI) to cover the metal anode surface, which can slow the dendrite formation and inhibit the corrosion of metal anode by polysulfides.^[55] This strategy can improve the electrochemical properties of M–S batteries but cannot overcome dendrite formation completely.

Electrocatalytic effects are important to the oxygen reduction reaction (ORR), hydrogen evolution reaction (HER), and oxygen evolution reaction (OER). The strategy has been adopted in the development of Li–S batteries and also applied to M–S batteries.^[10d,f,14,33,38,44,56] On the S cathodes, catalytic effect can reduce the reaction barrier between S and metal ions during the electrochemical cycling. It can be evaluated via the overpotential defined as the voltage difference between the charging and discharging plateaus. In this case, the reaction kinetics can be improved and higher conversion rate of the polysulfide intermediates can also be realized during charging/discharging process. The diffusion time of polysulfide intermediates can be reduced to mitigate the shuttle effect and improve the electrochemical stability and lifetime of the batteries. So far, the catalytic effect have effectively improved the utilization of S in the S cathode, and improved the electrochemical performance of M–S batteries. As for the metal anodes, the side reaction and uncontrolled growth of dendrites pose challenge. For instance, some Li/Na dendrites exfoliated from the Li/Na anodes are called “dead Li/Na” and the electrically isolated “dead Li/Na” can be generated constantly, resulting in the formation of a porous Li/Na anode and continuous deterioration of the electrochemical properties during cycling. To improve the performance of the metal anodes, an effective strategy is to use a substrate with abundant active sites to reduce the nucleation energy barrier of metal ions, so as to achieve the uniform deposition of metal and inhibit the growth of dendrites.

Up to now, there has been no commercial Li–S battery in the market. The Li–S battery industry is mainly stuck in the pilot-scale production stage of companies and universities.^[57] There is a huge gap between the Li–S industry and academic research, like two parallel lines. In terms of academic research, many papers have been published and achieved fruitful results in the past several decades. Many advanced carbon materials have been synthesized in the reported papers, but most are difficult to produce on a large scale. The commercialization process of Li–S batteries is slow due to the lack of carbon materials suitable for Li–S batteries in the market. Besides, the coulombic efficiency (CE) of Li–S batteries in academic studies is usually above 99%, while the CE of pouch cells can hardly reach 98%. Although the lithium nitrate (LiNO₃) additive can alleviate this phenomenon, it can also lead to safety risks for Li–S batteries.^[57] In addition, although great progress has been made on the fundamental scientific issues of the electrocatalyst application in Li–S systems, there is little research on their practical application.^[15,58] To accelerate the application of electrocatalysts for commercial Li–S batteries, more efforts are needed in the electrode design and component optimization under practical conditions.

Table 1. Properties of different types of M–S batteries.

Application	Species	Morphology	Final form	Performance	Electrolyte	Ref
Li–S batteries	N-doped carbon	Nanocages	S@hNCNC	1373 mAh g ⁻¹ at 0.2 A g ⁻¹ 539 mAh g ⁻¹ at 20 A g ⁻¹	1 m LiTFSI in 1,3-dioxolane (DOL)/ 1,2-dimethoxy ethane (DME) with 2% LiNO ₃	[12]
	Ni–N ₅	Rhombohedral-cuboctahedron shape particle	Ni–N ₅ /HNPC/S	1188 mAh g ⁻¹ at 0.2 C 684 mAh g ⁻¹ at 4 C	1 m LiTFSI in DOL/DME with 0.1 m LiNO ₃	[13]
	Fe–N–C	Mesocellular carbon foam	Fe–N–C/S-MCF	1244 mAh g ⁻¹ at 0.1 C 798 mAh g ⁻¹ at 5 C	1 m LiTFSI in DOL/DME with 2% LiNO ₃	[14]
	Co ₄ W ₁₈	Clusters	Co ₄ W ₁₈ /rGO	1426 mAh g ⁻¹ at 0.05 C 644 mAh g ⁻¹ at 5 C	0.5 m LiTFSI and 0.5 m LiNO ₃ in DOL/ DME	[15]
	P-doped NiTe ₂	Nanosheet	MSC/P–NiTe ₂	1318 mAh g ⁻¹ at 0.2 C 764 mAh g ⁻¹ at 5 C	1 m LiTFSI in DOL/DME	[16]
	Fe ₂ O ₃ /N-MC	Hierarchical structure	S@Fe ₂ O ₃ /N-MC,	1172 mAh g ⁻¹ at 0.2 C 740 mAh g ⁻¹ at 5 C	1 m LiTFSI in DOL/DME with 1% LiNO ₃	[17]
	Co ₉ S ₈ /Co	Nanoparticle	Li ₂ S–Co ₉ S ₈ /Co	1006 mAh g ⁻¹ at 0.1 C 616 mAh g ⁻¹ at 4 C	1 m LiTFSI and 0.2 m LiNO ₃ in tetraglyme	[18]
	Ti ₃ C ₂ MXene	Nanosheet	S/3D e-Ti ₃ C ₂ -2	1205.9 mAh g ⁻¹ at 0.2 C 772.4 mAh g ⁻¹ at 5.0 C	1 m LiTFSI in DOL/DME with 1% LiNO ₃	[19]
	MoS ₂	Monolayer	MoS ₂ -500	532 mAh g ⁻¹ at 5.0 C	1 m LiTFSI in DOL/DME with 2% LiNO ₃	[20]
	Halloysite TiO ₂	Nanoparticle	SC-TiO ₂ -Hal/S	1037.6 mAh g ⁻¹ at 0.2 C 566.9 mAh g ⁻¹ at 5.0 C	1 m LiTFSI in DOL/DME with 0.1 m LiNO ₃	[21]
	TiC	Nanoparticle	TiC@CNF/S	1058 mAh g ⁻¹ at 0.2 C 738 mAh g ⁻¹ at 5.0 C	1 m LiTFSI in DOL/DME with 2% LiNO ₃	[22]
	NiO–Ni ₃ N	Nanoparticle	NiO–Ni ₃ N-AC-S	1179 mAh g ⁻¹ at 0.2 C 652 mAh g ⁻¹ at 4.0 C	1 m LiTFSI in DOL/DME with 1% LiNO ₃	[23]
	Borophene	sheets	CNT/B	1329 mAh g ⁻¹ at 0.2 C 919 mAh g ⁻¹ at 4.0 C	1 m LiTFSI in DOL/DME with 1% LiNO ₃	[24]
	TiNb ₂ O ₇	Nanoparticle	ACC@TNO	1399 mAh g ⁻¹ at 0.1 C 885 mAh g ⁻¹ at 4.0 C	1 m LiTFSI in DOL/DME with LiNO ₃	[25]
	In ₂ S _{3–x}	Marigold-like Nanoparticle	In ₂ S _{3–x} /rGO	1182 mAh g ⁻¹ at 1.1 C 705 mAh g ⁻¹ at 5.5 C	1 m LiTFSI with 0.5 m LiNO ₃	[26]
	Ti ₃ C ₂ T _x /Ni–Co MOF heterostructure	Nanosheet	Ti ₃ C ₂ T _x /Ni–Co MOF	1260 mAh g ⁻¹ at 0.2 C 660 mAh g ⁻¹ at 2 C	1 m LiTFSI and 0.1 m LiNO ₃ in DOL/DME	[27]
	Pt	Nanoparticle	Pt/Ti ₂ C	890 mAh g ⁻¹ at 0.2 C 500 mAh g ⁻¹ at 2 C	1.0 m LiTFSI in 1:1 DME:DOL and 2 wt% LiNO ₃	[28]
	MoS ₃	Granular	MoS ₃ coated CNTs	585 mAh g ⁻¹ at 0.45 A g ⁻¹ 189 mAh g ⁻¹ at 9 A g ⁻¹	1.0 m LiTFSI in 1:1 DOL and DME with 0.1 m LiNO ₃	[29]
	Sb	Nanosheets	SbNs	997.7 mAh g ⁻¹ at 0.1 A g ⁻¹ 423 mAh g ⁻¹ at 1 A g ⁻¹	1.0 m LiTFSI in 1:1 DME: DOL and 1 wt% LiNO ₃	[30]
	Fluorinated covalent organic polymer	Porous network	S-COP-99	1287.7 mAh g ⁻¹ at 0.05 C 243.1 mAh g ⁻¹ at 5 C	1.0 m LiTFSI in 1:1 DOL and DME with 0.2 m LiNO ₃	[31]
DUT-177	–	S-DUT-177	720 mAh g ⁻¹ at 0.1A g ⁻¹ 276 mAh g ⁻¹ at 1 A g ⁻¹	LiTFSI in 1:1 DOL and DME with 0.1 m LiNO ₃	[32]	
RT Na–S batteries	Atomic Co	Cluster	S@Co _n -HC	820 mAh g ⁻¹ at 0.1 A g ⁻¹ 220 mAh g ⁻¹ at 5 A g ⁻¹	1.0 m NaClO ₄ in propylene carbonate (PC)/ethylene carbonate (EC) + 5 wt% fluoroethylene carbonate (FEC),	[2c]
	NiS ₂	Nanocrystal	NiS ₂ @NPCTs/S	760 mAh g ⁻¹ at 0.1A g ⁻¹ 203 mAh g ⁻¹ at 5 A g ⁻¹	1.0 m NaClO ₄ in PC/EC + 3 wt% FEC)	[33]
	AlOOH	Nanosheet	S@CB@AlOOH	865 mAh g ⁻¹ at 0.1 C 388 mAh g ⁻¹ at 1 C	1 m NaClO ₄ and 0.2 m NaNO ₃ tetra(ethylene glycol) dimethyl ether (TEGDME)	[34]
	CoP–Co	Hollow cage	S@CoP-Co/NCNHC	644 mAh g ⁻¹ at 0.1 C 208 mAh g ⁻¹ at 5 C	1.0 m NaClO ₄ in PC/EC + 3 wt% FEC)	[35]
	Ti ₃ C ₂ T _x MXene	Nanosheet	S–Ti ₃ C ₂ T _x	821.7 mAh g ⁻¹ at 2 C 610.3 mAh g ⁻¹ at 5 C	2.0 m NaClO ₄ in PC/EC + 3 wt% FEC)	[36]

Table 1. Continued.

Application	Species	Morphology	Final form	Performance	Electrolyte	Ref
	rGO/VO ₂	Nanoflower	rGO/VO ₂ /S	558.1 mAh g ⁻¹ at 0.2 C 194 mAh g ⁻¹ at 2 C	1 M NaClO ₄ in TEGDME	[37]
	Mo ₂ N–W ₂ N heterostructures	Spherical superstructure	S/Mo ₂ N–W ₂ N@PC	915 mAh g ⁻¹ at 0.2 A g ⁻¹ 190 mAh g ⁻¹ at 2 A g ⁻¹	2 M NaTFSI in ethylene carbonate (EC)/FEC	[38]
	Fe(CN) ₆ ⁴⁻ -doped polypyrrole	Fiber	CFC/S@FC-PPy	1071 mAh g ⁻¹ at 0.1 A g ⁻¹ 441 mAh g ⁻¹ at 2 A g ⁻¹	1 M NaFSI with 1% NaNO ₃ in TEGDME	[39]
	FeNi ₃	Hollow spheres	S@FeNi ₃ @HC	1102 mAh g ⁻¹ at 0.2 A g ⁻¹ 383 mAh g ⁻¹ at 5 A g ⁻¹	2 M NaTFSI in EC/FEC	[40]
	Fe ₃ N	Fiber	S@ Fe ₃ N-NMCN	1238.6 mAh g ⁻¹ at 0.1 C 658.4 mAh g ⁻¹ at 10 C	1 M NaPF ₆ in DOL/ Diglyme	[41]
	Co	Nanoparticle	MG-Co@S	705 mAh g ⁻¹ at 0.1 C 428 mAh g ⁻¹ at 5 C	1 M NaPF ₆ in DOL/ Diglyme	[42]
	MoS ₂ /MoN heterostructure	Nanosheet	MoS ₂ -MoN@CC	692 mAh g ⁻¹ at 0.1 C 227 mAh g ⁻¹ at 1 C	1 M NaClO ₄ and 0.2 M NaNO ₃ TEGDME	[43]
K–S batteries	N-doped Co	Nanocluster	S–N–Co ₅ –C	577.1 mAh g ⁻¹ at 0.02 A g ⁻¹ 415.2 mAh g ⁻¹ at 0.4 A g ⁻¹	0.8 M KPF ₆ in EC/diethyl carbonate (DEC)	[44]
	Microporous carbon	Nanoparticle	C/S	1198.3 mAh g ⁻¹ at 0.02 A g ⁻¹ 741.2 mAh g ⁻¹ at 2 A g ⁻¹	0.8 M KPF ₆ in EC/DEC	[9d]
	Pyrolyzed PAN	Nanoparticle	SPAN	697 mAh g ⁻¹ at 0.1 C 218 mAh g ⁻¹ at 3 C	0.8 M KPF ₆ in EC/DEC	[9e]
	CMK-3	–	CMK-3/S	522.5 mAh g ⁻¹ at 0.05 A g ⁻¹	1.0 M KClO ₄ in TEGDME	[45]
	Activated CNF paper	Nanofiber	S-CNF	1140 mAh g ⁻¹ at C/10 770 mA h g ⁻¹ at C/3	KCF ₃ SO ₃ in TEGDME	[46]
Ca–S batteries	Activated carbon cloth	–	ACC/S	900 mAh g ⁻¹ at 0.1 C	0.5 M Ca[B(hfp) ₄] ₂ in DME	[10b]
	Ketjenblack (KB)	–	S/C	760 mAh g ⁻¹	Ca[B(hfp) ₄] ₂ in DME	[47]
Mg–S batteries	Ag substrate	–	S@Ag	1000 mAh g ⁻¹	Mg(TFSI) ₂	[10d]
	Cobalt loaded mesoporous carbon matrix	Spherical shape	MesoCo@C-S	780 mAh g ⁻¹ at 0.2 C 380 mAh g ⁻¹ at 0.4 C	a mixture of MgCl ₂ , AlCl ₃ and Mg powder in DME/ PYR14TFSI	[48]
	Activated carbon cloth	–	ACCS	930 mAh g ⁻¹ at 0.1 C	0.4 M MgBhfp/DME	[49]
	Co ₃ S ₄ @MXene heterostructure	Nanosheet	Co ₃ S ₄ @MXene-S	1144 mAh g ⁻¹ at 0.1 C 297 mAh g ⁻¹ at 2 C	0.4 M (MgPhCl)- AlCl ₃ in tetrahydrofuran (THF)	[50]
Al–S batteries	Co-doped Carbon	Matrix	S@Co/C	1650 mAh g ⁻¹ at 0.1 A g ⁻¹ 300 mAh g ⁻¹ at 3 A g ⁻¹	[EMIM]Cl:AlCl ₃	[10f]
	Metallic Cu	Nanoparticle	S@HKUST-1-C	1200 mAh g ⁻¹ at 1 A g ⁻¹	[EMIM]Cl /AlCl ₃	[51]
	Mesoporous carbon	–	S@CMK-3	1390 mAh g ⁻¹ at 0.251 A g ⁻¹	NBMPBr /AlCl ₃	[52]
	CNF	Nanofiber	S/CNF	1250 mAh g ⁻¹ at 0.02 C 860 mAh g ⁻¹ at 0.1 C	Li ⁺ -Al[EMI]Cl ₄	[10e]
	CMK-3	–	S@CMK-3	1550 mAh g ⁻¹ at 0.1 A g ⁻¹ 688 mAh g ⁻¹ at 0.3 mA g ⁻¹	AlCl ₃ / AcA-1.3	[53]
	N-doped hierarchical porous carbon	Foam-like	S@HPCK	1330 mAh g ⁻¹ at 0.2 A g ⁻¹ 272 mAh g ⁻¹ at 2 A g ⁻¹	AlCl ₃ /AcA	[54]

Some articles have reviewed the research progress of metal–S batteries, but the application of catalysts in nonlithium–S batteries is still less discussed.^[1,8a,59] In addition, these articles tend to focus on the catalytic effect of the S cathode, but little

on the catalytic effects of the anode and electrolyte. However, high-performance metal–S batteries need to consider all components of batteries, such as cathode, anode and electrolyte. Therefore, the catalytic effects involved in metal–S batteries



Figure 1. Schematic illustration of the development of metal–S batteries.

need to be discussed in depth, especially their practical application in future commercial M–S batteries. In this review, recent advance in the study of catalytic effects in M–S batteries is described. The charging/discharging mechanisms of the S cathodes and metal anodes are discussed and design strategies for the S cathodes, metal anodes, and electrolytes are described from the perspective of catalytic effects using Li–S and RT Na–S batteries as examples. Other M–S batteries involving K–S, Ca–S, Mg–S, and Al–S are also discussed. The practical application of electrocatalysts in the field of Li–S systems is also described, and finally, the challenges and prospects are discussed.

2. Li–S Batteries

The typical charging/discharging process of Li–S batteries is shown in **Figure 2a**. The conversion from S_8 to the final product Li_2S follows solid (S_8) \rightarrow liquid (Li_2S_n) \rightarrow solid (Li_2S_2/Li_2S) processes. S_8 is reduced relatively fast to the highly soluble S_8^{2-} , S_6^{2-} , and S_4^{2-} at an average voltage of 2.3 V (vs Li^+/Li). In this process, each S atom receives 0.5 electrons corresponding to a theoretical capacity of 418 mAh g^{-1} .^[60] The long-chain Li polysulfides (LiPSs) are reduced to insoluble Li_2S_2/Li_2S slowly. Conversion between the solid Li_2S_2 and solid Li_2S is a slow solid-phase reaction which limits the conversion rate of Li–S batteries.^[61] In this process, each S atom receives 1.5 electrons thus providing a high theoretical capacity of 1254 mAh g^{-1} . During charging of Li–S batteries, Li_2S is gradually reconverted to S_8 in the inverse conversion processes to complete the reversible electrochemical cycle.

The development of S as energy-storage materials was proposed a long time ago (**Figure 2b**).^[6,59a,62] The first use of S as electrode material was proposed by Herbet and Ulam in 1962,

who used S and sodium sulfides (Na_2S) to synthesize sodium polysulfides (NaPSs) chemically.^[63] The soluble LiPSs were analyzed by Coleman and Bates in 1968 and they found that the transparent electrolyte turned into a red-black solution in the incomplete discharge state in the Li/dimethyl sulfoxide (DMSO)– $KClO_4/S$ system.^[59a] Since then, tremendous efforts have been made to overcome this phenomenon in Li–S batteries. On the heels of recent development of advanced characterization techniques, a deeper mechanistic understanding of Li–S chemistry is guiding cell design to improve the electrochemical performance. For instance, See et al. have discovered that Li_2S is deposited during discharging and S reprecipitates after charging process as revealed by in situ nuclear magnetic resonance (NMR).^[64] Moreover, polysulfide radicals have been observed directly by in situ electron paramagnetic resonance (EPR) and S in organic solvents has been determined quantitatively by high-performance liquid chromatography using an ultraviolet (UV) detector.^[65] To deeply reveal the chemical immobilization and catalytic transformation of LiPSs on mediator, Gao et al. have obtained the S K-edge information of S/NCNT@ SnS_2 and S/NCNT@Co- SnS_2 at different reaction states via ex situ X-ray adsorption near-edge structure spectroscopy (XANES).^[66] S/NCNT@ SnS_2 barely changes from 2.0 to 1.7 V, while S/NCNT@Co- SnS_2 shows a new peak of Li–S bond, indicating that the effective conversion of soluble LiPSs to the final discharge product Li_2S . This confirms that the Co doping can significantly inhibit the accumulation of soluble LiPSs and promote the nucleation of Li_2S . In addition, the characteristic peaks of S reappears at the terminal state of charging process, indicating the completely conversion of Li_2S to pristine S. The development of these advanced characterization techniques deepens the understanding of the fundamental reaction mechanism of Li–S batteries and provides a new approach for the study of other M–S batteries.

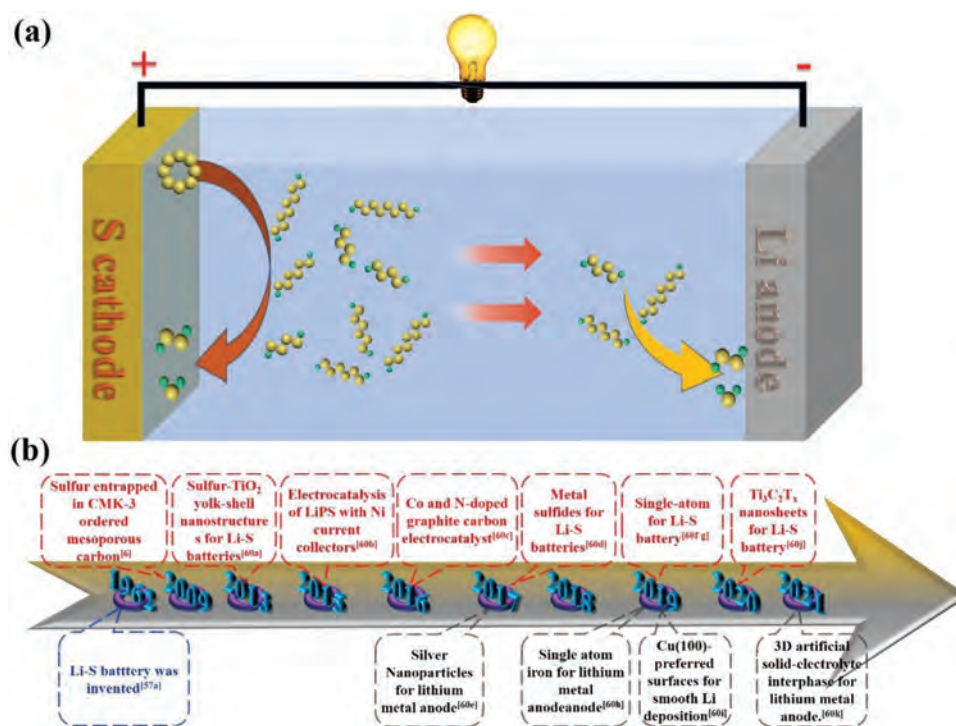


Figure 2. a) Reaction mechanism of LiPSs in the Li–S batteries. b) Development history of Li–S batteries.^[6,59,62]

2.1. Sulfur Cathodes

Previous research of S cathodes has mostly focused on improving the electrochemical properties of Li–S batteries by decreasing dissolution of LiPSs in organic electrolytes and various physical and chemical adsorption methods have been developed to deal with the shuttle effect. Ji et al. have proposed a feasible approach to stabilize the S cathode by forming a highly ordered interwoven composite structure (Figure 3a).^[6] The conductive mesoporous carbon framework effectively limits the growth of S nanofillers in the continuous channels and produces good contact with insulating S. The composite provides a route for Li⁺ to react with S through the conductive carbon framework. Inhibition of LiPSs diffusion in the carbon framework and the adsorption property of the carbon framework to LiPSs also contribute to the capture of LiPSs formed during the redox processes. However, slow capacity fading indicates that the porous carbon cannot entirely prevent the loss of LiPSs. In this case, polyethylene glycol (PEG) has been used to modify the carbon surface to provide a chemical gradient and prevent outward diffusion of large LiPS anions from the electrode. Based on the advanced electrode structure, the S cathode shows a high reversible capacity of 1320 mAh g⁻¹. This study provides a route to improve the electrochemical performance of Li–S batteries by introducing conductive framework. Later, scientists proposed a series of porous carbon materials as hosts for S.^[67] Li et al. have synthesized ordered microporous carbon as a confining matrix for S.^[68] Small S_{2,4} molecules are confined in the micropores to prevent contact between LiPSs and solvent molecules thus avoiding the irreversible reaction between carbonate molecules and dissolution of LiPSs in the ether-based

electrolytes. The S_{2,4} molecules in the micropores of the carbon ensure a solid–solid redox reaction instead of the conventional solid–liquid–solid redox reaction, thereby limiting diffusion of LiPSs during cycling. However, the effects of physical adsorption to stabilize LiPSs via a porous carbon matrix are relatively limited and consequently, the slow kinetics is not totally solved.

High-activity electrocatalysts can maximize the utilization of active components. Introducing the catalysts into the S cathode is a new strategy to accelerate reduction of LiPSs to Li₂S₂/Li₂S and/or converse oxidation to S and inhibit the dissolution of LiPSs.^[59a] To our knowledge, Babu et al. have first proposed the electrocatalytic concept for Li–S batteries.^[62b] Catalysts including Pt, Au, and Ni are coated on traditional current collectors (such as Al foil and stainless steel foil) to serve the dual roles of the current collectors and electrodes in Li–S batteries. The Li–S batteries consisting of Au, Pt, and Ni coated current collectors exhibit reduced polarization and larger discharge capacity than Li–S batteries comprising the conventional Al current collectors. Macroporous 3D Ni is used as the host and current collector for the S cathode to maximize the surface accessibility and a high and stable reversible capacity of up to 900 mAh g⁻¹ is realized (Figure 3b). This study carves a new path for improving the performance of Li–S batteries. Subsequently, Peng et al. have further studied the fundamental electrocatalytic mechanism of the N and S dual-doped holey graphene framework (N,S-HGF) catalyst used in Li–S batteries.^[69] According to the diffusion-limited current density (*J_D*), the battery with N,S-HGF catalyst has a high electron transfer number of 7.8 in the S reduction reaction (SRR), reflecting that the S reaction is highly complete and LiPSs is rapidly transformed into insoluble products. According to the Arrhenius equation,

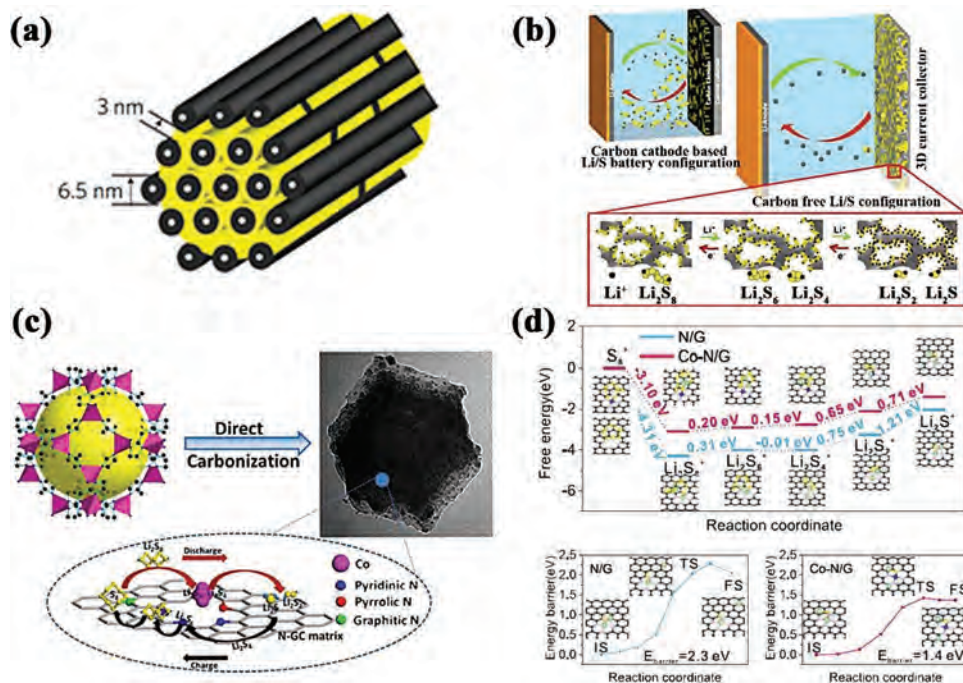


Figure 3. a) Schematic diagram of the S (yellow) confined in CMK-3 ordered mesoporous carbon. S is trapped in CMK-3 ordered mesoporous carbon. Reproduced with permission.^[6] Copyright 2009, Springer Nature. b) Schematic of the conventional carbon cathode based Li/S battery and metal/PS/metal battery configuration with 3D current collectors. Reproduced with permission.^[62b] Copyright 2015, Springer Nature. c) Schematic illustration of the preparation of the dual-catalysts anchored Co-N-GC composite and the interaction with LiPSs during charging/discharge in the Li-S battery. Reproduced with permission.^[62c] Copyright 2016, The Royal Society of Chemistry. d) DFT calculation of the fast kinetics of Li-S battery using the Co single-atom catalyst. Reproduced with permission.^[62d] Copyright 2019, American Chemical Society.

the battery with N,S-HGF catalyst has a low activation energy (E_a) of 0.06 eV, reflecting the superior kinetics of SRR. Besides, the battery with N,S-HGF catalyst has a small Tafel slope (η) and a high exchange current density (J_0), further reflecting the high reaction kinetics of Li-S batteries. This study reveals the fundamental electrocatalytic mechanism of the electrocatalyst for Li-S batteries and provides a promising strategy to overcome the challenges faced by Li-S batteries. Up to now, many electrocatalysts for S cathode have been studied, and great progress has been made.

2.1.1. Metal-Based Nanomaterials

Metal-based nanomaterials, a typical class of heterogeneous catalysts, have been studied in the field of energy conversion and introduced to Li-S batteries in recent years. Metal-based nanocatalysts have the ability to capture LiPSs due to the interaction between the metal atoms and LiPSs.^[62g] The interaction accelerates charge transfer on the S electrode to catalyze the conversion of LiPSs. In addition, with decreasing size, more surface metal atoms and quantum size effects are observed to benefit the catalytic activity. For example, Zhou et al. have synthesized Co-based nanomaterials with different size using Co single atoms (Co-SAs/NC), Co nanoclusters (Co-ACs/NC), and Co nanoparticles (Co-NPs/NC) as host materials in Li-S batteries.^[70] The Co-SAs/NC cell shows the lowest

overpotential ($\Delta E = 0.279$ V) compared to Co-ACs/NC ($\Delta E = 0.294$ V) and Co-NPs/NC ($\Delta E = 0.298$ V), revealing that the smaller size of the Co-based nanomaterials leads to improved electrocatalytic effects in the Li-S batteries. The Co-SAs/NC cell shows a reversible capacity of 935 mAh g⁻¹ after 100 cycles confirming that a small particle size is more suitable for high-performance Li-S batteries.

It is noted that the hybrid systems of N-doped carbon-supported transition metals are efficient nonprecious metal catalysts.^[71] The transition metals participate as active catalysts in LiPSs conversion based on the interaction between the transition metals and LiPSs.^[72] The strong favorable interactions contribute to the adsorption and dissociation of intermediates on the surface of the catalysts enabling fast charge exchange between them to accelerate redox conversion of LiPSs. The N-doped carbon matrix improves the utilization efficiency of the catalysts by facilitating dispersion and providing continuous electron conduction to the electrode. For example, Li et al. have synthesized a 3D porous N-doped graphitic carbon-Co nanoparticle composite (Co-NG) as a host for the S cathode (Figure 3c).^[62c] In this composite, Co nanoparticles are dispersed uniformly in the N-doped graphitic carbon matrix with a large surface area. The Co nanoparticles not only catalyze electrochemical transformation from LiPSs to Li₂S₂ and/or Li₂S, but also accelerate conversion from long-chain LiPSs to S. This electrode structure improves the rate performance and cyclic stability even for a large S concentration of 70 wt%. The

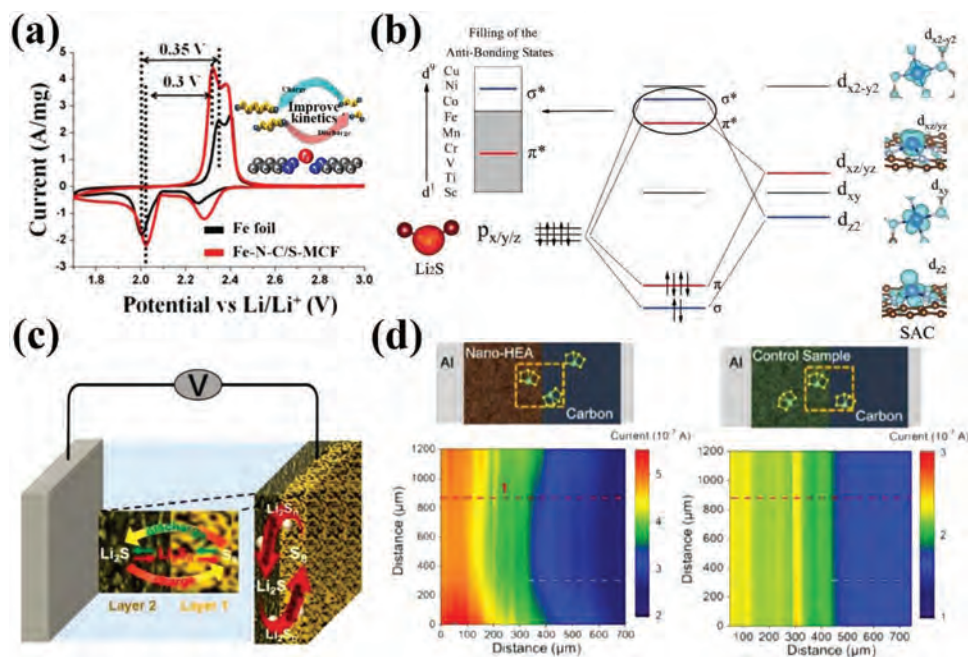


Figure 4. a) Single-atom Fe electrocatalytic conversion of intermediates in the Li–S batteries. Reproduced with permission.^[14] Copyright 2018, American Chemical Society. b) d–p orbital hybridization scenario between SAC and Li₂S. Reproduced with permission.^[73] Copyright 2021, Wiley-VCH. c) Dual layer S cathode for the stepwise electrocatalytic process. Reproduced with permission.^[74] Copyright 2019, American Chemical Society. d) The reaction activity of LiPSs around the electrode with nano-HEA and without nano-HEA. Reproduced with permission.^[75] Copyright 2021, Elsevier Ltd.

multifunctional cathode can be operated at 1 C for more than 500 cycles with CE approaching 100%.

If the size of metal nanoparticles is continuously reduced, they will eventually reach the atomic level and a series of single-atoms catalyst (SACs) materials have been studied for Li–S batteries. Du et al. have reported single-atom Co embedded in N-doped graphene (Co–N/G) as the host for S (Figure 3d).^[62] The study reveals that the Co–N–C coordination center accelerates the formation and decomposition of Li₂S in discharging and charging. The overpotential for the conversion between Li₂S and LiPSs is the lowest, indicating that Co–N/G renders the electrocatalytic effect. Furthermore, theoretical calculation indicates that the Gibbs free energies for reduction of Li₂S₂ and decomposition of Li₂S on Co–N/G are much lower than those on N-doped graphene (NG). As a result, the S@Co–N/G cathode (90 wt% S) shows a high gravimetric capacity of 1210 mAh g^{−1}, areal capacity of 5.1 mAh cm^{−2} with a fading rate of 0.029% per cycle for 100 cycles at 0.2 C at an S loading of 6.0 mg cm^{−2}. The Co–N/G host also serves as a bifunctional catalyst for both reduction and oxidation thus accelerating the discharging and charging processes. Similar to the Co–N/G, single-atom Fe catalyst has been used to improve the kinetics of Li–S batteries.^[14] Lim et al. have introduced the Fe–N–C molecular catalyst on the surface of mesoporous carbon microspheres with a large pore volume to serve as the hosts for S in Li–S batteries (Figure 4a). The host materials have a large pore volume that can accommodate up to ≈87 wt% S. In addition, the host materials have controllable uniform spherical morphology, which improves the tap density of S–MCF, and thus increases the capacity of S cathode. Cyclic voltammetry (CV) curves show the positive shift of reduction peaks and negative shift of the oxidation

peaks after introducing the Fe–N–C molecular on the surface of mesoporous carbon microspheres. The Tafel plot is an important parameter reflecting the catalytic activity of a catalyst for the S conversion. The results show that the slopes of both the reduction reaction and oxidation reaction are small, indicating that the uniform distribution of Fe–N–C (only 0.33 wt%) improves the redox kinetics of the conversion reaction of S and facilitates the efficient absorption of soluble LiPSs during electrochemical cycling. The cyclic stability of the S composite cathode is maintained at 84% of the initial capacity after 500 cycles at 3 C for an S loading of 5.2 mg cm^{−2}. Recently, Han et al. have revealed that transition metals with a small atomic number such as Ti with only slightly filled antibonding states shows the most effective d–p hybridization (Figure 4b).^[73] The SACs interact with Li₂S and soluble LiPSs to break S–S bonds in the S chain structure and accelerate LiPSs reduction. They also break Li–S bonds in the Li₂S cluster and decrease the energy barrier in Li₂S oxidation. Single-atom metal catalysts (Mn, Cu, Cr, and Ti) are embedded in 3D electrodes by controllable N coordination and density functional theory (DFT) calculation shows that the single-atom Ti-embedded electrode has the lowest electrochemical barrier to LiPSs reduction/Li₂S oxidation as well as highest catalytic activity, indicating that d–p orbital hybridization between SAC and S is a viable approach to develop highly active SACs for advanced Li–S batteries.

Conversion of S during charging/discharging is a multistep process and researchers have mainly considered the conversion step of LiPSs instead of the complete conversion process of Ye et al. have prepared a S cathode by using a dual-layer design in which two metal catalysts of Fe–N-doped carbon (Fe–NC) and Co–N-doped carbon (Co–NC) are configured in the S cathode

and proposed a method for stepwise electrocatalysis in the electrochemical conversion process of Li–S batteries (Figure 4c).^[74] The electrochemical experiments and DFT calculation reveal that Fe-NC catalyzes conversion of elemental S to soluble LiPSs, whereas Co-NC accelerates conversion of LiPSs to the final product of Li₂S. Owing to the unique dual-layer design, soluble LiPSs are formed in the inner layer (Fe-NC) and then diffuse outward to form insoluble Li₂S in the electrolyte-facing outer layer (Co-NC) by electrochemically deposition during discharging. During charging, the solid Li₂S deposited in the outer layer is oxidized electrochemically into soluble LiPSs and diffuses inward to the inner layer to be converted into elemental S. The S cathode with a dual-layer structure controls diffusion of LiPSs into the dual-catalyst layer but not the electrolyte consequently eliminating the shuttle effect of LiPSs during cycling. The S cathode retains ≈90% of the theoretical specific capacity of S and exhibits a high areal capacity of ≈8.3 mAh cm⁻² with a low electrolyte/S (E/S) ratio of 5 μL mg⁻¹. The double-layer catalyst structure catalyzes the electrochemical reaction process of Li–S batteries and paves the way for inhibiting the shuttle effect of LiPSs and improving the kinetics of batteries.

High-entropy alloys (HEAs) have many unique virtues and potential in catalyzing complex redox reactions. Xu et al. have synthesized nano-HEA composed of five elements (Fe, Co, Ni, Mn, and Zn) as catalyst for Li–S batteries.^[75] To study the reaction kinetics of HEA during the discharge process, the rotating disk electrode (RDE) is measured. The results show that HEA has a higher J_D . According to the Levich–Koutecký equation, the electron transfer numbers of nano-HEA at 2.0, 1.8, and 1.6 V are 3.4, 5.7, and 5.8, respectively, while the electron transfer numbers of the control sample at the same voltages are 2.67, 3.1, and 3.7, respectively. The larger electron transfer number of nano-HEA indicates that the conversion kinetics of the LiPSs intermediate is faster. The η of the nano-HEA is much smaller than that of the control sample, indicating that the redox reaction is easier to proceed around the nano-HEA. The higher J_0 also indicates that the nano-HEA can accelerate the redox kinetics. In addition, owing to the strong affinity between nano-HEA and LiPSs, the reactivity of LiPSs around the electrode with nano-HEA is much higher than that around the electrode without nano-HEA according to the result of scanning electrochemical microscopy (Figure 4d). The buffering effect of the nano-HEA catalyzes the activation polarization, leading to a higher J_0 and larger current response. DFT calculation further reveals the smooth and continuous surface charge redistribution that is favorable to the multi-electron reactions of LiPSs. Because of the combined effects, the Li–S batteries assembled with the nano-HEA exhibit outstanding capacity retention rates of 83.3% (2 C after 500 cycles in coin cell) and 82% (0.1 C for 150 cycles in pouch cell), respectively.

2.1.2. Metal Compounds

The transformation of LiPSs into Li₂S₂ or Li₂S is a liquid–solid reaction and the nucleation and growth of Li₂S₂/Li₂S is an essential process in the discharge process of Li–S batteries. Nonpolar carbon is often used as a support for both metal nanoparticle catalysts and single-atom catalysts. However, it is

difficult to deposit solid Li₂S₂/Li₂S on the nonpolar surface of carbon host. Metal oxide, a kind of polar materials, interacts strongly with LiPSs through the polar–polar, Lewis acid–base, or thiosulfate–polythionate conversion interactions to enhance the electrochemical performance of Li–S batteries.^[76] Compared to carbon materials, metal oxide compounds not only have higher binding energy with LiPSs, but also are beneficial to the deposition of the final discharge products of Li₂S₂/Li₂S. TiO₂, a common and low-cost metal oxide with hydrophilic Ti–O groups and surface hydroxyl groups, has been proven to bind favorably with polysulfide anions (calculated binding energies of Li₂S₄ and Li₂S with TiO₂ are 1.24 and 1.96 eV, respectively).^[76f,77] Seh et al. have reported the use of polar TiO₂ as the host to accommodate S molecules and prepare S/TiO₂ yolk–shell composites for Li–S batteries (Figure 5a).^[62a] Due to the polar surface on the TiO₂ shell that accelerates nucleation and growth of Li₂S₂/Li₂S, the electrode exhibits a high initial specific capacity of 1030 mAh g⁻¹ at 0.5 C with CE approaching 100% for 1000 cycles. The capacity decay is only 0.033% per cycle after 1000 cycles to corroborate the structural stability.

Although metal oxide catalysts can facilitate nucleation and growth of Li₂S₂/Li₂S, most of the stoichiometric metal oxides are insulators thus hampering the transfer of electrons/ions in the electrochemical reactions. This problem can be solved by combining metal oxide compounds with a carbon skeleton to host S. The carbon skeleton provides ion/electron transfer channels to ensure rapid nucleation of Li₂S on the metal oxides. Peng et al. have proposed to block the shuttle effect of LiPSs and accelerate the reaction kinetics of Li–S batteries by establishing a cooperative interface between the S cathode and separator (Figure 5b).^[78] By this design of nanosized “sulfiphilic” layered double hydroxide and mesoporous “lithiophilic” NG, the cooperative interface provides bifunctional chemical bonding with *Li and *S, thus preventing the loss of LiPSs and catalyzing the formation of Li₂S. Furthermore, the NG framework is electrically conductive and mechanically stable, which provides channels for the transfer of ions/electronic and alleviates the volume change of S cathode. This work not only solves the problem of poor electron/ion of metal oxide, but also opens the door for the design of advanced catalyst materials with cooperative interfaces to regulate the active intermediates. The concept of cooperative interfaces has been extended to other systems. Zhang et al. have used a nickel–cobalt double hydroxide (NiCo-DH) shell to encapsulate S and used graphene and carbon nanotube (CNT) as the conductive network (Figure 5c).^[79] The outer homogeneously distributed graphene and CNTs form the conductive framework, which provides channels for the migration of ions/electrons between the electrolyte and active materials. Moreover, NiCo-DH preserves S through physical and chemical constraints. The key mechanism is that the thiosulfate group on the surface of NiCo-DH catenates and traps LiPSs to form the polythionate complex as well as Li₂S₂/Li₂S.

The smooth “adsorption–diffusion–conversion” process is an effective strategy to balance adsorption of LiPSs and enhance diffusion and the electrical conductivity of the mediators to improve the electrochemical performance of Li–S batteries. The adsorption and diffusion properties of LiPSs have been studied but the nucleation process of Li₂S from LiPSs is relatively unknown. Recently, Kong et al. have designed an

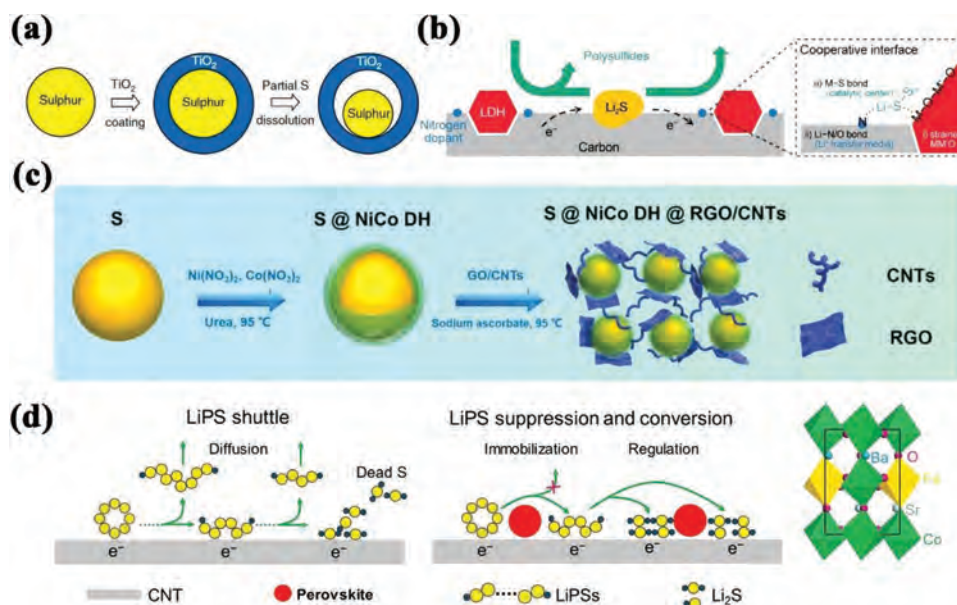


Figure 5. a) Schematic of the preparation that involves coating of S nanoparticles with TiO₂ to form the core-shell nanostructures. Reproduced with permission.^[62a] Copyright 2013, Springer Nature. b) Schematic illustration of the cooperative interface of LDH@NG. Reproduced with permission.^[78] Copyright 2016, Wiley-VCH. c) Schematic illustration to synthesize the S@NiCo-DH@RC composite. Reproduced with permission.^[79] Copyright 2018, Wiley-VCH. d) Roles of the bifunctional perovskite promoter for trapping LiPSs and Li₂S regulation in the Li-S batteries. Reproduced with permission.^[80] Copyright 2017, Wiley-VCH.

electrode structure with CNTs loaded Ba_{0.5}Sr_{0.5}Co_{0.8}Fe_{0.2}O_{3-δ} perovskite nanoparticles (PrNPs) to adsorb LiPSs and accelerate deposition of Li₂S (Figure 5d).^[80] The chemical bonding (Li-O and Sr-S bonds) based on lithiophilic (O) and sulfiphilic (Sr) sites and increased metal reactivity arising from oxygen vacancies are more likely to anchor LiPSs. What's more, the natural affinity between PrNP and LiPSs provides the nucleation sites to accelerate Li₂S deposition and guides uniform growth. This strategy enhances the reaction kinetics of LiPSs and regulates deposition of Li₂S and as a result, Li-S batteries comprising the bifunctional hosts exhibit a small capacity decay rate of 0.05% for 40 cycles together with a capacity of 753 mAh g⁻¹ at 2 C.

Metal sulfide is a kind of materials with strong sulfiphilic properties and relatively low lithiation potential. It has excellent electrocatalysis on the redox reactions and is widely used in Li-S batteries.^[81] In addition, metal sulfide generally have relatively higher conductivity than metal oxide, and some metal sulfide even have metallic or semimetallic phases. For instance, Pan et al. have prepared layer-spacing-enlarged MoS₂ nanotubes (LE-MoS₂) consisting of hierarchical superstructural nanosheet (-MoS₂-carbon layer-MoS₂-) and applied them to Li-S batteries.^[82] The enlarged layer space and hierarchical superstructure improve the conductivity of LE-MoS₂, and enhance the electrocatalytic effect and adsorption capability of MoS₂ to LiPSs. After annealing, the carbon intercalation maintains the large layer space and enhances the conductivity between adjacent MoS₂ monolayer. The catalytic effect and adsorptive ability of LE-MoS₂ are revealed by in situ XANES technology, indicating that the LE-MoS₂ has a strong interaction with LiPS/Li₂S. DFT calculation shows that the adsorption ability of LE-MoS₂ to Li₂S₆ and Li₂S₈ are 14.5% and 17.4% higher than that of unexpanded MoS₂. The S-loaded LE-MoS₂ shows

a high initial capacity of 1550 mAh g⁻¹ and low capacity decay rate of 0.06%. In addition, Wu et al. have proposed the conception of built-in catalysis in confined nanocontainers for Li-S batteries.^[83] The researchers employ Al-based metal-organic framework (MOF) as precursor to prepare an ordered ladder-like carbon framework coupled with built-in MoS₂ catalyst. After removing the Al₂O₃ template, the loosely stacked carbon layer self-assembled into 3D ladder-like frameworks with high aspect ratio and mesoporous voids between adjacent layers. The ultrathin MoS₂ nanosheets are uniformly loaded and paved in the inner mesoporosity. Such a structure provides integrated function of adsorption-catalysis-conversion. The constructed S cathode has a high initial capacity of 1240 mAh g⁻¹ at 0.2C, an outstanding cyclic stability of 1000 cycles at 2 C and a high tolerance up to 20 C. This electrode releases a considerable reversible capacity under high S loading and lean electrolyte.

Except from metal oxide and sulfide, polar metallic catalysts with improved electrical conductivity can catalyze the redox reactions of LiPSs, and improve the electrochemical characteristics of Li-S batteries, especially cycling at large current densities.^[84] As a result, researchers have tried to develop host materials with conductive properties and electrocatalytic effects that can simultaneously trap the LiPSs and modulate the LiPS redox kinetics. Metal nitrides such as TiN, and InN have better electrical conductivity and potential in inhibiting the loss of LiPSs and accelerating the redox processes in Li-S batteries.^[85] Moreover, metal nitride possesses better physicochemical stability than their oxide and sulfide counterparts because the highly basic N₃-sites attract metal cations and stabilize the lattice.^[86] It also have the metallic lattice structure with interstitial alloying of N resulting in excellent conductivity.^[85b] According to the Lewis acid-base principle, the intrinsic chemical polarity of

metal nitrides interact with the weak-polar LiPSs to inhibit dissolution of LiPSs. Indium nitride (InN) has a narrow bandgap and metal-like properties that can be used to anchor materials for LiPSs and accelerate reversible conversion of LiPSs, thus improving the electrochemical performance of Li–S batteries. Zhang et al. have introduced InN nanowires to accelerate the conversion of S for Li–S batteries (Figure 6a).^[87] Both the In cations and electron-rich N atoms in InN can act as anchors for LiPSs through the strong chemical affinity to inhibit the shuttle effect. In addition, the high electrical conductivity of InN enables rapid electron transport across the surface of InN during discharging and charging and accelerates conversion of LiPSs. Therefore, the prepared Li–S batteries deliver excellent rate and stable cycling performance with only 0.015% capacity decay per cycle after 1000 cycles.

As another kind of catalysts for Li–S batteries, metal phosphides also have the polar characteristic, good electrical conductivity and excellent stability to promote the electrochemical reaction between Li and S. On the one hand, the electronegative P atoms in phosphide draw electrons from metal atoms and act as a base to attract positively charged species.^[88] On the other hand, transition metal phosphides with the appropriate atomic ratio of metal to P have metallic characteristics or even superconductivity.^[89] Huang et al. have studied the multifunctional effects of iron phosphide (FeP) nanocrystals incorporated in the 3D porous reduced graphene oxide (rGO)–CNT scaffold and the electrochemical properties of Li–S batteries (Figure 6b).^[90] The DFT calculation reveals that the FeP nanocrystals have highly effective chemisorption of LiPSs to prevent the loss of LiPSs.

The FeP nanocrystals also act as catalysts for the faster LiPSs conversion during electrochemical cycling and reduce LiPSs dissolution. The FeP nanocrystals anchored on the rGO–CNT framework also provide an adsorptive interface to accelerate nucleation and growth of Li_2S to improve the redox kinetics. The porous rGO–CNT scaffold can transport Li^+/e^- quickly and efficiently, thus achieving high utilization and rapid redox of S. Therefore, the constructed FeP/rGO/CNT-S cathode has a high capacity of 1291 mAh g^{-1} at a current density of 0.1 C with outstanding stability of 0.04% decay per cycle. Similarly, Yang et al. have studied the role of molybdenum phosphide (MoP) nanoparticles in the conversion of the S cathode (Figure 6c). It reduces the overpotentials in the charge and discharge reactions even under lean electrolyte conditions.^[91] The S cathode containing MoP nanoparticles shows fast kinetics and high S utilization, resulting in improved charging/discharging voltage profiles, capacity, rates, as well as cyclic stability of the batteries. Owing to the electrocatalytic effect of MoP, a highly reversible areal capacity of 5.0 mAh cm^{-2} is observed from the Li–S battery despite an E/S ratio of $4 \mu\text{L mg}^{-1}$.

Transition metal carbides are a kind of interstitial alloys prepared by introducing carbon atoms into the lattices and preferably locates at the largest sites available for parent metals.^[92] Since discovered by Levy and Boudart to have the platinum-like properties, transition metal carbides have been considered as candidates for cheap catalysts because of their excellent electrical conductivity and electrocatalytic activity.^[93] Recently, transition metal carbide has been introduced into Li–S batteries.^[94] Li et al. has designed an N-doped carbon hierarchical

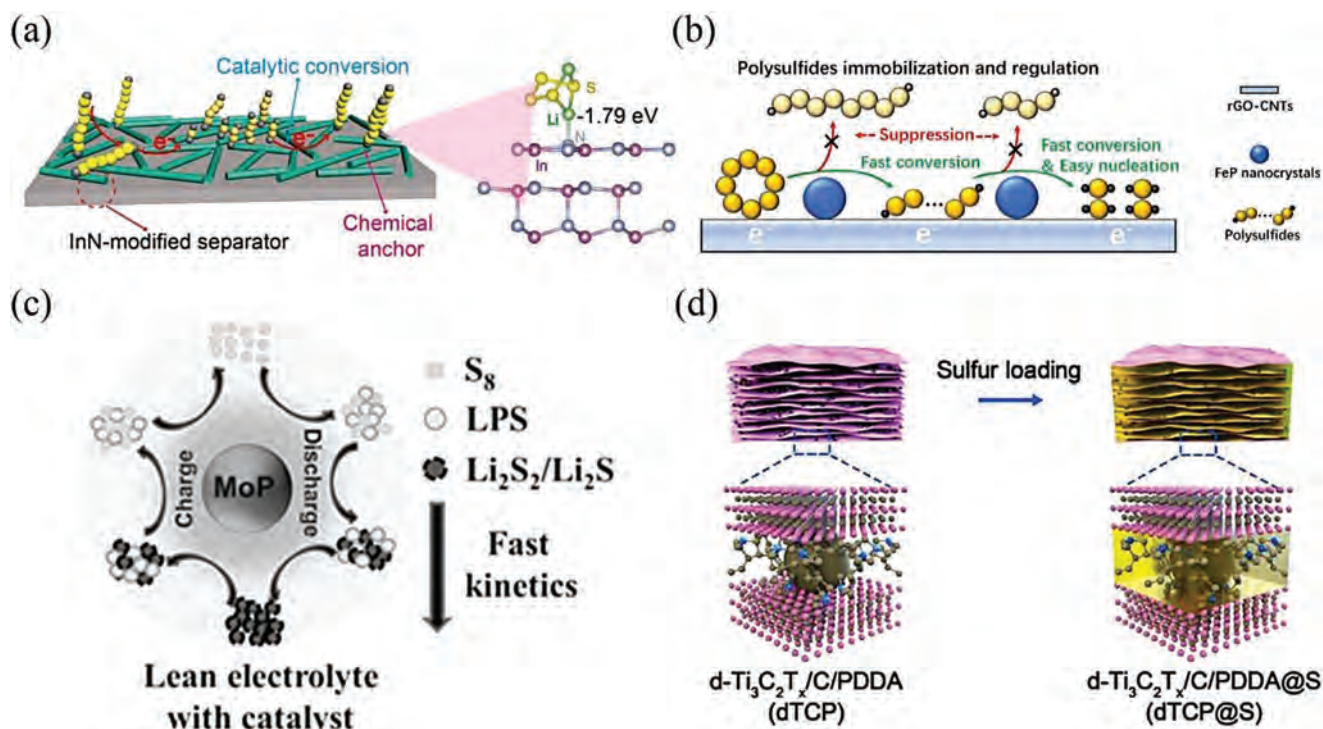


Figure 6. a) Schematic illustration of the LiPSs conversion reaction on the surface of InN nanowires. Reproduced with permission.^[87] Copyright 2018, American Chemical Society. b) Roles of FeP in LiPSs suppression and regulation. Reproduced with permission.^[90] Copyright 2018, Elsevier Ltd. c) Schematic of possible reaction pathways for a S cathode catalyzed by MoP under lean electrolyte conditions. Reproduced with permission.^[91] Copyright 2018, Wiley-VCH. d) Structure of dTCP and dTCP@S. Reproduced with permission.^[62] Copyright 2021, Elsevier Ltd.

double-shelled hollow spheres decorated with molybdenum carbide ($\text{Mo}_2\text{C}/\text{C}$ HDS-HSs), which has a mesoporous thick inner shell and a microporous thin outer shell, and further used it as a host for S.^[95] In this unique structure, the carbon framework can ensure a high S loading, buffer the shuttle effect and provide a transfer channel for Li^+ , while the $\text{Mo}_2\text{C}/\text{C}$ backbone can promote the conversion kinetics of LiPSs and further improve the utilization of S. As a result, the $\text{M}_2\text{C}/\text{C}/\text{S}$ HDS-HSs electrode with a high S loading (5.8 mg cm^{-2}) can provide a large reversible capacity of 901.4 mAh g^{-1} , excellent rate capability of 641.9 mAh g^{-1} at 5 C and ultralong cyclic stability of 874.5 mAh g^{-1} after 500 cycles at 1 C.

MXenes, a class of 2D materials including transition metal carbides, nitrides, and carbon-nitrides, have prospects in the energy-storage, electromagnetic, electronic, and structural fields.^[96] Pure MXenes (without terminal functional groups) have a high electronic conductivity up to $2.4 \times 10^5 \text{ S cm}^{-1}$, which can overcome the electronic insulation defects of S and $\text{Li}_2\text{S}_2/\text{Li}_2\text{S}$.^[97] Theoretical studies indicate that there are abundant $-\text{O}$, $-\text{F}$, and/or $-\text{OH}$ groups at the end of the structure in MXene to capture LiPSs and prevent dissolution and shuttling of LiPSs in the electrolytes.^[98] The lamellar structure of MXene can physically block shuttling of soluble LiPSs but MXene nanosheets prepared by traditional methods restack easily so that the number of active sites and electrical conductivity decrease. Therefore, restacked MXene is not preferred for Li-S batteries. To improve the properties of MXene in Li-S batteries, Zhang et al. have designed 3D MXene-based S cathodes (Figure 6d).^[62] When carbon-poly(diallyl dimethyl ammonium chloride) (C/PDDA) nanoparticles are dispersed homogeneously in MXene nanosheets, the positively charged ammonium groups in the C/PDDA NPs interact with the negatively charged surface of $\text{Ti}_3\text{C}_2\text{T}_x$ nanosheets to form a 3D framework which prevents restacking and aggregation of $\text{Ti}_3\text{C}_2\text{T}_x$ nanosheets for improved electrical conductivity. The 3D MXene-based materials not only improve utilization of S by providing abundant contact sites for the electrolyte to fully permeate, but also prevent the shuttle effect of LiPSs due to physical separation and

chemisorption between the LiPSs and abundant functional groups of MXene. In addition, the lower overpotential demonstrates that MXene accelerates conversion of LiPSs. The S cathode has a highly reversible specific capacity of $1016.8 \text{ mAh g}^{-1}$ at a current density of 0.2 C and excellent cyclic stability exemplified by a capacity loss of only 0.075% per cycle for 600 cycles at 1 C.

2.1.3. Heterostructures

Polar metal oxides have the ability to capture LiPSs but the low electrical conductivity of most metal oxides hinders direct conversion of LiPSs on the surface.^[99] This makes the captured LiPSs must be diffused to a conductive substrate nearby to achieve electrochemical transformation. On the contrary, metal compounds like TiN and FeP with good electrical conductivity and provide a large number of active sites to accelerate LiPSs conversion. However, the adsorption capability of these metal compounds for LiPSs is generally inferior to that of metal oxides. In this case, designing a heterogeneous interface between the anchoring mediator and conducting mediator is expected to realize efficient adsorption and transformation for LiPSs. Zhou et al. have designed a twinborn TiO_2 -TiN heterogeneous interface combining the adsorbent TiO_2 and conductive TiN to realize the smooth “adsorption-diffusion-conversion” process through the interface (Figure 7a).^[100] Here, TiO_2 absorbs LiPSs, whereas TiN accelerates conversion of LiPSs into insoluble Li_2S . The potentiostatic discharging curves reveal that the capacity of Li_2S precipitate on the TiO_2 -TiN heterostructure (137 mAh g^{-1}) is higher than that on TiO_2 or TiN, proving that the TiO_2 -TiN heterostructure has a positive effect on adsorption and conversion of LiPSs. A high reversible specific capacity of 927 mAh g^{-1} is maintained after 300 cycles at a current density of 0.3 C. Yang et al. have synthesized MoO_2 - Mo_2N binary nanobelts to regulate the electrochemical reactions of Li-S batteries (Figure 7b).^[101] The binary nanobelts coordinated the polar MoO_2 and electrically conductive Mo_2N accelerate the reaction from S_8 to LiPSs and then Li_2S .

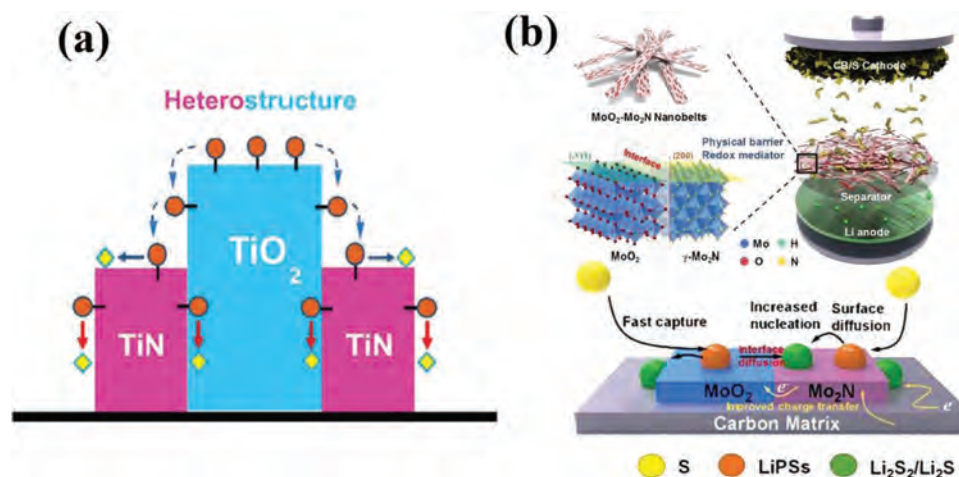


Figure 7. a) Schematic of the LiPSs conversion processes on the TiO_2 -TiN heterostructured surface. Reproduced with permission.^[100] Copyright 2017, The Royal Society of Chemistry. b) Schematic illustration and atomic model of the MoO_2 - Mo_2N heterostructure and LiPSs conversion on the surface of the MoO_2 - Mo_2N binary structure. Reproduced with permission.^[101] Copyright 2020, Elsevier Ltd.

Therefore, the MoO₂–Mo₂N binary nanobelts thus combine the advantages of rapid capture of LiPSs and optimization of nucleation of insoluble Li₂S. Such heterostructure contains rapid transportation pathways for the intermediates by three steps. The long-chain LiPSs are captured by polar MoO₂ via the strong S–Mo and Li–O interactions and then captured LiPSs diffuse to the conductive Mo₂N through the interface of MoO₂ and Mo₂N. Finally, the diffused LiPSs acquire electrons on the conductive Mo₂N surface to enhance nucleation of Li₂S.

2.1.4. Defect Engineering

Defect engineering plays an important role in optimizing the electronic structure and improving the electrochemical performance of catalysts in various applications because of its ability to tailor the atomic distribution and adjust the surface property of catalysts. It also attracts a great attention on the design of catalyst for S in Li–S batteries.^[102] Due to the exposure of active lattices and edge sites, as well as the relatively precise control of atomic distribution and electronic structure, the defective mediators can regulate LiPSs behavior to achieve rapid redox. At present, many kinds of defective mediators have been reported, including defects, dopants, and vacancies, which are discussed as follows.

The rapid emergency of carbonaceous catalysts with artificially induced intrinsic defects as promising substitutes for noble metal catalysts has attracted extensive attention. The defects such as pentagon and heptagon rings of carbon can promote the local electronic redistribution and the bandgap contraction, leading to superior bonding affinity and electrocatalytic activity. Cai et al. have introduced a large number of intrinsic defects into carbon black through wet-chemistry strategy and applied them to Li–S batteries.^[103] Raman, XPS and EPR results demonstrate the successful introduction of defects in carbon back. It is noteworthy that the carbon back treated with 1 mL H₂O₂ (CB-2) has more intrinsic defects than those treated with 0.5 and 2 mL of H₂O₂, which makes CB-2 has higher electrocatalytic activity, which is consistent with the experimental and theoretical calculations. As a result, the S/CB-2 cathode exhibits a superior rate capacity of 1179.1 mAh g⁻¹ at 0.2 C and outstanding cyclic stability (891.7 mAh g⁻¹ after 100 cycles at 1 C).

Heteroatomic doping is another important strategy in defect engineering. The electronic conductivity, electronic structure, and surface properties of materials can be changed by doping. Liu et al. have prepared N-doped Co₉S₈ nanoparticles,^[104] and these N-doped nanoparticles are proved to have enhanced LiPSs capture capacity, thus significantly improving the performance of Li–S batteries.^[105] On the other hand, DFT calculations and experiment show that a strong chemical bond exists between N-Co₉S₈ and LiPSs, because Li–N bond is more conductive to LiPSs capture than Li–S bond. As a result, the Li–S batteries with N-doped Co₉S₈ nanoparticles as the host has a capacity of up to 1233 mAh g⁻¹ at 0.2 A g⁻¹, high redox reaction rate (604 mAh g⁻¹ at 20 A g⁻¹) and excellent capacity retention (0.037% per cycle after 1000 cycles). Cation doping can also optimize the electronic structure of nanocatalyst and improve its electrocatalytic effect on the LiPSs conversion. For example,

Shen et al. have used metallic Ni₂P as a catalyst and substituted Ni with Co to improve its catalytic activity on the LiPSs conversion reactions.^[106] When doped with cations to a certain extent, the original crystallographic framework of Ni₂P is disordered, which increases the d-band of the metal sites and reduces the activation barrier. Theoretical analysis shows that the terminal S atoms of LiPSs are adsorbed to the triply bridged metal sites through strong metal–S bonds, and the S–S bonds of LiPSs are weakened due to the redistributed electronic structure. In addition, the researchers have also prepared Ni₂Co₄P₃ on a highly porous nickel scaffold (PNS) following with embedded ion-selective filtration layer into the shallow surface to construct microreactor-like S cathode to maximize the catalytic effect. The prepared S cathode has a high initial capacity of 1223 mAh g⁻¹ with an ultralow decay rate of 0.39 mAh g⁻¹ per cycle up to 1000 cycles and a high capacity of 413 mAh g⁻¹ after 150 cycles with an ultrahigh S loading of 25 mg cm⁻².

Nonmetallic heteroatoms (e.g., N, S, B, and halogens) doped carbon as catalysts have also attracted a lot of attention in Li–S batteries.^[102,107] In carbon-based metal-free catalysts, the dopant atoms interact with carbon atoms through covalent chemical bonds, which can avoid the segregation problem in metal-alloy catalysts and have good operational stability.^[108] In addition, the dopant atom can induce the charge transfer and change the electronic structure on the surface of carbon materials, thus improving the performance of Li–S batteries. Recently, Du et al. have used multifunctional hierarchical N-doped carbon nanocages as host materials for Li–S batteries.^[12] The results of electrocatalytic experiments and density function theory simulations show that the high electrocatalytic effect of N-sites can accelerate the conversion of LiPSs. Meanwhile, the porous structure of hierarchical N-doped carbon nanocages can realize the physical confinement and chemisorption of LiPSs, thus inhibiting the shuttle effect. As a result, the prepared Li–S batteries with areal S loading of 0.8 mg cm⁻² exhibit a high capacity of 539 mAh g⁻¹ at an ultrahigh current density of 20 A g⁻¹, and an excellent cyclic stability with a high capacity of 438 mAh g⁻¹ after 1000 cycles at 10 A g⁻¹. Even when the areal S loading is increased to 3 mg cm⁻², the prepared Li–S batteries can still provide a high capacity of 605 mAh g⁻¹ at a high current density of 3 A g⁻¹.

Creating vacancy is an important defect engineering strategy to change the geometrical and chemical configurations of compounds. Due to the abundance of localized electrons, vacancy can act as trapper and active sites to limit and accelerate the conversion of various intermediates, thus improving the performance of Li–S batteries.^[109] Oxygen vacancies are common anionic vacancies in transition metal oxides due to their low formation energy. Luo et al. have designed an ultrafine, amorphous and oxygen deficient niobium pentoxide nanocluster embedded in microporous carbon nanospheres (A-Nb₂O_{5-x}@MCS) and used it as host material for Li–S batteries.^[110] The amorphous and defective structure of Nb₂O_{5-x} enhances the chemisorption to LiPSs, while the oxygen vacancy further enhances the catalytic effect for the rapid transformation of LiPSs. In addition, the nanocluster embedded in microporous carbon sphere promotes the uniformly distribution of S and exposes a large number of active interfaces, providing transport channels for ions/electrons. This structure provides a synergistic

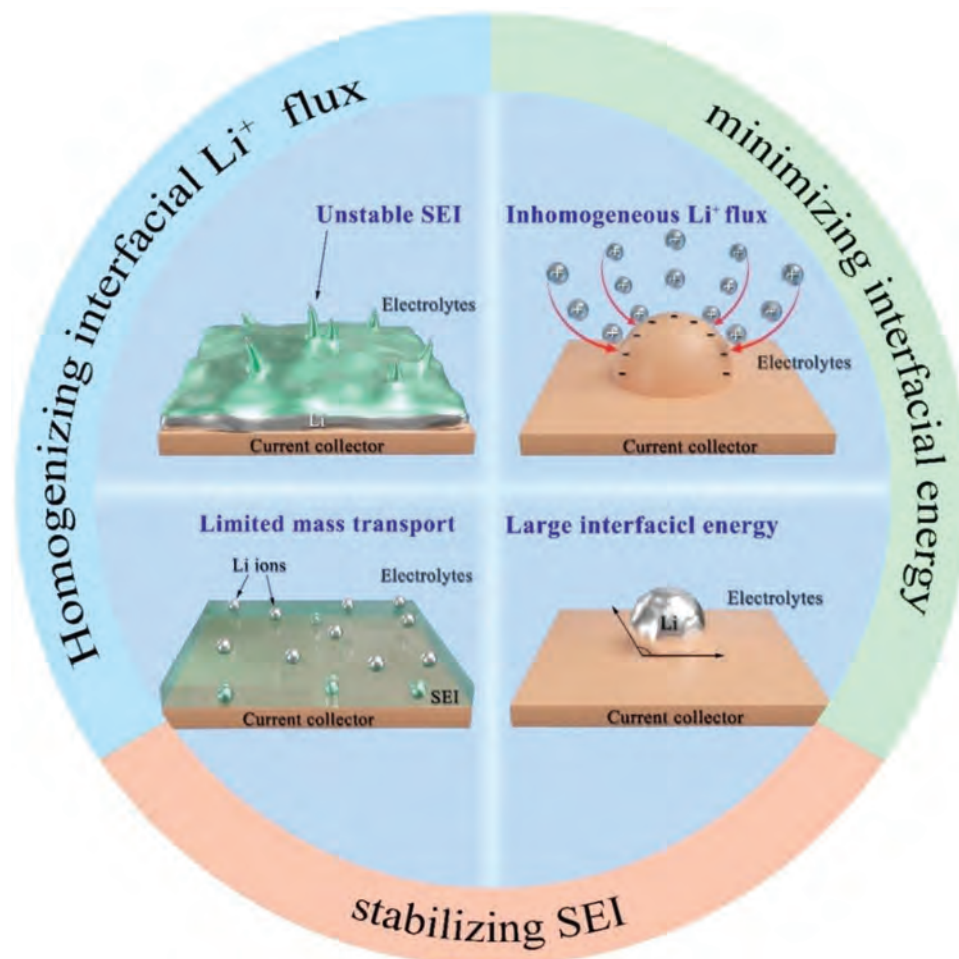


Figure 8. Schematic diagram showing the key interfacial challenges for Li anodes in the liquid electrolyte systems.

regulation of crystallinity and oxygen deficiency for rapid and durable S conversion. Benefiting from the unique structure, the $A\text{-Nb}_2\text{O}_{5-x}\text{@MCS}$ shows an outstanding cyclic stability with a low capacity fading of 0.024% per cycle over 1200 cycles, excellent rate capability as well as high areal capacity of 6.62 mAh cm^{-2} under high S loading of 5.8 mg cm^{-2} and lean E/S ratio (4.5 mL g^{-1}). Cation vacancy also shows great promise in improving the electrochemical activity. For instance, Zhao et al. have reported an etching-induced vacancy strategy to form cation vacancy in Ni_3FeN .^[111] The Fe atoms at the corner of cubic premediator Ni_3FeN are etched by polysulfide to form metastable $\text{Ni}_3\text{Fe}_{1-\delta}\text{N}$. The smaller η for the Ni_3FeN /graphene cell suggests that liquid polysulfide reacts with solid S/ Li_2S faster due to the regulation of $\text{Ni}_3\text{Fe}_{1-\delta}\text{N}$. Besides, the corresponding onset potentials for $\text{Ni}_3\text{Fe}_{1-\delta}\text{N}$ -modified LiPS redox are 37 mV positive for reduction and 16 mV negative for Li_2S oxidation, further suggesting the high catalytic activity of $\text{Ni}_3\text{Fe}_{1-\delta}\text{N}$.

In this part, the application of electrocatalyst for S cathode in Li-S batteries is discussed in depth and the introduction of these electrocatalysts makes Li-S batteries with improved electrochemical performance. Based on the above discussion, we can see that different type of electrocatalysts have different properties. For metal nanomaterial electrocatalysts, their

excellent conductivity and the effective utilization of electrocatalytic active sites make them outstanding in S cathode. On the other hand, the naturally insulated metal compounds strongly absorb LiPSs and provide polar surface for the deposition of $\text{Li}_2\text{S}_2/\text{Li}_2\text{S}$. Therefore, the ideal catalyst medium for Li-S batteries should have excellent electrical conductivity, large active surface, as many active sites as possible, and appropriate affinity for LiPSs, thus improving the redox kinetics of LiPSs. In addition, advanced electrode structure design also plays an important role in improving the catalytic effect of catalyst. For example, the 3D porous structure electrode design can expose more catalytic active sites and facilitate the infiltration of electrolyte, thus improving the performance of the batteries. Finally, the morphology of S cathode is also important for the utilization of S. Although the host material should provide space for buffering the volume change of S during the electrochemical cycling, if the pore volume or SSA is too large, the conductivity of the host material will be reduced,^[112] and then the tap density and volumetric capacity of S cathode will be reduced, which is detrimental to the practical application of the S cathode. Therefore, the rational design of interspace in host material is of great significance to the application of Li-S batteries.

2.2. Lithium-Metal Anodes

Since the advent of LIBs, the energy density of LIBs has been improved but is still short of the target of 500 Wh kg^{-1} for application in electric vehicles. Li-metal anodes (LMAs) have high specific capacity (3860 mAh g^{-1}) and low redox potential (-3.04 V versus the standard hydrogen electrode). For example, the theoretical energy density of Li-S batteries is 2600 Wh kg^{-1} , which is about 5 times higher than that of traditional LIBs. However, the LMAs have some drawbacks such as the large volume change during electrochemical cycling of Li-S batteries and uncontrolled growth of Li dendrites. By hosting the Li-metal in an advanced porous structure, the space in the hosts can overcome the volume variation of LMAs. Uncontrolled growth of Li dendrites is the key that limits the practical application of LMAs. Formation of Li dendrite involves the transportation and reduction of Li^+ during charging. Local ion/electron enrichment and side reactions arising from the unstable and inhomogeneous interface produce Li dendrites and low CE in Li electroplating and stripping. Therefore, it is necessary to understand the interfacial chemistry and charge transfer of LMAs. As shown in **Figure 8**, the interfacial issues of LMAs can be divided into four parts: unstable SEI, inhomogeneous interfacial Li^+ flux, limited mass transport, and large interfacial energy and should be properly addressed.^[113]

2.2.1. Conductive Hosts

Theoretically, a uniform Li^+ flux to the electrode interface leads to uniform Li deposition. However, defects and other inhomogeneities become the “hot spots” for preferential deposition of

Li giving rise to dendrite formation. An effective strategy to modify LMAs is to adopt a conductive host to accommodate the Li metal. High conductivity and large surface area reduce the current density (J) and make the Li^+ distribution relatively uniform. Moreover, the conductive host provides space to accommodate the volume change during charging and discharging to enhance the stability of the SEI film and uniformity of Li^+ . Cu foil is a common current collector in LIBs but not suitable in LMAs due to the limited electroactive area. However, this problem can be solved by designing a functional 3D Cu framework. Yang et al. have prepared a 3D Cu foil with a porous structure to provide a large number of charge centers and active sites for uniform Li deposition (**Figure 9a**).^[114] The LMAs can operate for 600 h without failure, indicating that the 3D Cu framework improves the cyclic stability and safety. At the same time, it shows a high areal capacity and maintains good Li^+ electroplating/stripping efficiency of 98.5%. Different techniques have been developed to synthesize 3D Cu frameworks. Yun et al. have prepared a 3D porous Cu framework by chemical dealloying from the commercial Cu-Zn alloy (**Figure 9b**).^[115] After complete dissolution of Zn from Cu-Zn alloy, the interconnected 3D Cu framework exhibits outstanding electrical conductivity and abundant porosity. The pore distribution in the 3D Cu current collector regulates deposition of Li, buffers the volume change of Li during electroplating/stripping, and inhibits the formation of Li dendrites. As a result, the LMAs with the 3D Cu framework current collector are stable for 250 cycles at 0.5 mA cm^{-2} with CE up to 97%. They can be operated stably for more than 140 cycles at 1.0 mA cm^{-2} with reduced polarization.

Deposition of Li on a heterogeneous substrate needs to overcome the interfacial barrier related to surface energy and

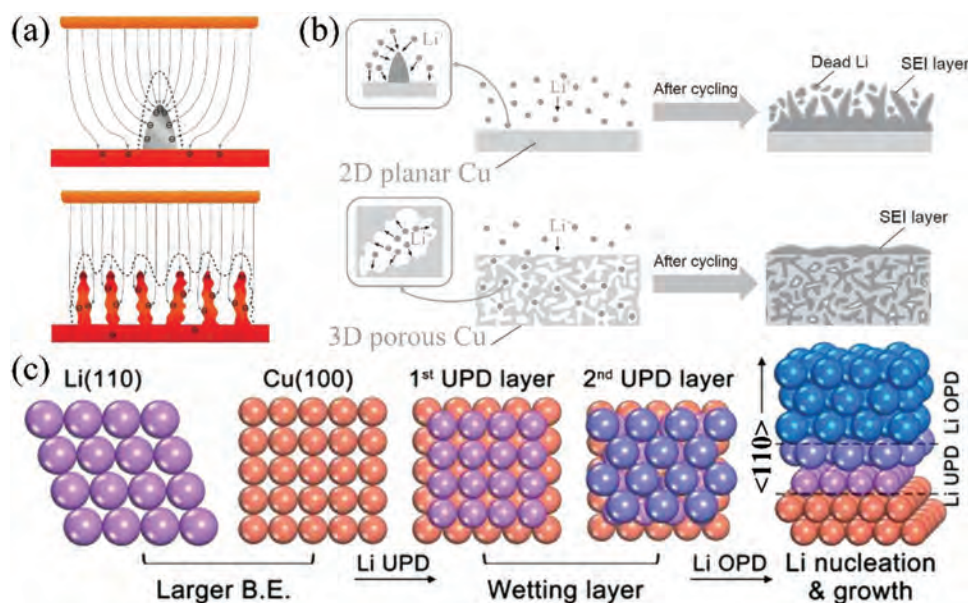


Figure 9. a) Electrochemical deposition mechanism of Li metal on the planar current collector and 3D current collector. Reproduced under the terms of the CC-BY Creative Commons Attribution 4.0 International license (<https://creativecommons.org/licenses/by/4.0>).^[114] Copyright 2015, The Authors, published by Springer Nature. b) Schematic of the structural changes in different Li-metal anodes. Reproduced with permission.^[115] Copyright 2016, Wiley-VCH. c) Schematics of the structures of Li underpotential deposition layers and crystallographic orientation of bulk Li deposit. Reproduced with permission.^[62] Copyright 2019, Wiley-VCH.

Table 2. Electrochemical properties and parameters of Li anodes with metal- and carbon-based current collectors.

Species	Morphology	Final form	Electrolyte	Performance	Ref.
3D graphene framework	Hollow spheres	3D-GF	1 M LiTFSI in DOL-DME with 1 wt% LiNO ₃	CEs of 97.8% at 0.5 mA cm ⁻² and CE of 97.2% at 1 mA cm ⁻² for 1 mA h cm ⁻²	[116]
Cu(100)-preferred Cu foam	3D skeleton	Faceted Cu meshes	LiTFSI in DME/DOL	CEs of 99% at 2 mA cm ⁻² over 400 cycles CE of 97% at 4 mA cm ⁻² over 400 cycles	[62i]
Ag	Nanoparticle	AgNP/CNFs	1 M LiTFSI in DOL/DME	CE of 98% at 0.5 mA cm ⁻² for 500 h	[62e]
Ag	Nanoparticle	Ag@CMFs	1 M LiTFSI in DOL-DME with 2 wt% LiNO ₃	CE of 98% at 1 mA cm ⁻² with 1 mAh cm ⁻²	[117]
Nano-Cu-embedded carbon	Porous	Cu@carbon	1 M LiTFSI in DOL-DME with 2 wt% LiNO ₃	CE of 99.3% at 0.25 mA cm ⁻² , 98.7% at 0.5 mA cm ⁻² , and 98.1% at 2.0 mA cm ⁻² with the capacity of 1.0 mA h cm ⁻²	[118]
Li _x M (M = Si, Sn, or Al)	Nanoparticle	Li _x Si/graphene foils	1.0 M LiPF ₆ in EC/DEC	CE of 99.92% at 1 mA cm ⁻² with an capacity of 2.4 mAh cm ⁻²	[119]
Tiny Co nanoparticle	Nanosheet arrays	CC@CN-Co	1 M LiTFSI in DOL-DME with 2 wt% LiNO ₃	CEs of 98.3% at 2 mA cm ⁻² for 2 mAh cm ⁻²	[120]
ZnO	Carbon felt	CFZO-Li	1.0 M LiPF ₆ in EC and DEC	99.1% over 400 cycles at 1 mA cm ⁻² with 1 mA h cm ⁻²	[121]
ZnO	Nanofibers	ZnO/CNFs@Li	1 M LiTFSI in DOL-DME with 0.2 M LiNO ₃	CE of 98% at 1 mA cm ⁻² with 1 mAh cm ⁻²	[122]
MoS ₂	Nanofiber	PCNF/MoS ₂ -Li	1.0 M LiPF ₆ in EC and DMC	CE of 93% of at 1 mA cm ⁻² with 1 mAh cm ⁻²	[123]
g-C ₃ N ₄	3D architecture	3D g-C ₃ N ₄ /G/g-C ₃ N ₄	1 M LiTFSI in DOL-DME with 1 wt% LiNO ₃	CE of 99.1% at 1.0 mA cm ⁻² with 1.0 mAh cm ⁻²	[62k]
Carbon framework	Coaxial interweaved	CNT@POF	1.0 M LiTFSI in DOL/DME with 5% LiNO ₃	CE over 98.5% at the 1.0 mA cm ⁻² and the capacity of 1.0 mAh cm ⁻²	[124]
Poly(styrene-co-divinylbenzene)	Network	M-Li-metal anode	1.0 M LiFSI in DME and TTE	CE of 99.8% at 1.0 mA cm ⁻² and 1.0 mAh cm ⁻²	[125]

lattice mismatch between the substrate and nuclei, and a small nucleation barrier is more conducive to uniform deposition of Li on the substrate. According to crystallography, the (110) plane of the Li crystal is the densest arranged and has the smallest nucleation barrier. The lattice mismatch between the Cu (100) plane and Li (110) plane is also minimal, which is conducive to nucleation and growth of Li.^[62i] Gu et al. have used the electrochemical method to prepare the Cu (100)-preferred surface on both planar and 3D Cu current collectors (Figure 9c). The Cu (100)-preferred surface is lithiophilic and Li can be guided to grow along the Li (110) direction by the Li (110) oriented Li underpotential deposition layer. Compared to the original Cu meshes, the contact angle between the molten Li and Cu foam with the (100)-preferred surface reflects the reduced interfacial energy. The results reveal not only preparation of smooth Li planar thin films, but also homogeneous electroplating/stripping of Li on the 3D Cu current collector with high utilization.

Although great efforts have been made to develop 3D metal frameworks for LMAs, uniform deposition of Li is possible only at low current densities and cycling capacity on account of the limited surface area. In addition, metal frameworks are quite heavy. Carbon is a potential alternative for the 3D metallic framework and can be fabricated into a variety of morphologies such as nanotubes, nanofibers, and nanosheets. Compared to metal frameworks, carbon hosts are more suitable for LMAs at large current densities, as shown in Table 2. Pan et al. have proposed a 3D graphene framework with large interconnect

channels for transfer of Li⁺ and accommodation of metallic Li (Figure 10a).^[116] The 3D porous framework not only strengthens the structure to preserve the hollow structure in spite of the pressure generated during battery assembly, but also decreases the overpotential without requiring dopants or precious metals. The hollow spheres facilitate ion diffusion, inhibit the growth of Li dendrites, and improve the rate capability of LMAs. Experiments show that due to the low density and large pore space in the 3D graphene framework, no obvious dendrite formation is observed during electrochemical cycling and a high capacity of over 2600 mAh g⁻¹ is achieved.

2.2.2. Nucleation Regulation

Similar to Cu current collectors, the affinity between carbon and Li⁺ is poor and uniform deposition of Li on carbon can be achieved only by reducing the interfacial energy between carbon and Li. Heteroatomic substitution is an effective strategy to convert carbon into a lithiophilic substrate. N and O doping can improve the lithiophilic properties of carbonaceous materials for LMAs.^[126] The heteroatoms have high binding energy with Li⁺, consequently reducing the interfacial energy and providing a large number of active sites for Li nucleation. Formation of a lithiophilic layer on the surface of the current collector is also an effective method to enhance the affinity between the current collectors and Li.^[117,120] For example, Yang et al. have embedded

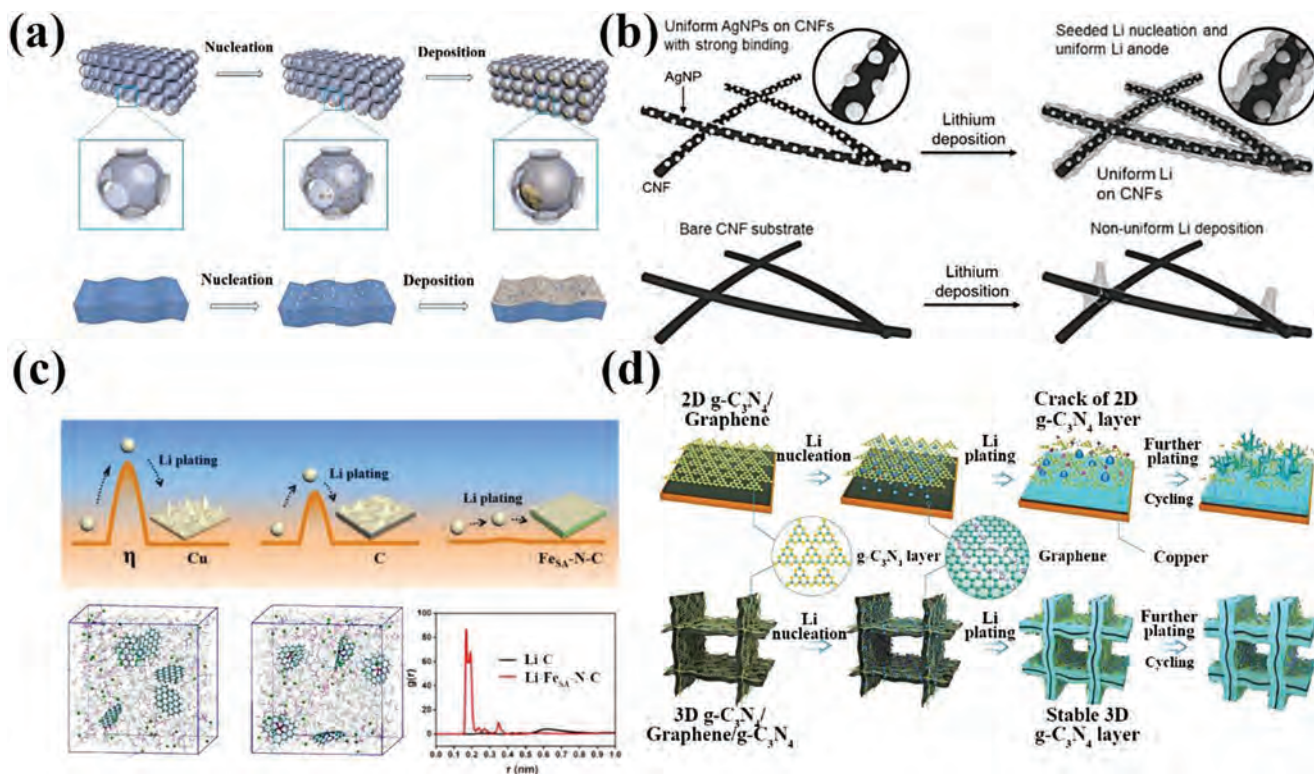


Figure 10. a) Schematic diagrams showing Li nucleation and growth on the 3D-GF and graphene paper. Reproduced with permission.^[116] Copyright 2019, American Chemical Society. b) Schematic illustration of Li deposition on 3D host materials with Uniform Ag NPs and bare CNF. Reproduced with permission.^[62e] Copyright 2017, Wiley-VCH. c) Fe Single-atom minimizing the Li nucleation barrier in stable Li-metal batteries. Reproduced with permission.^[62h] Copyright 2019, American Chemical Society. d) Illustration of Li deposition on 2D g-C₃N₄/Graphene electrode and 3D g-C₃N₄/G/g-C₃N₄ electrode. Reproduced with permission.^[62k] Copyright 2021, Wiley-VCH.

ultrafine Ag NPs (≈ 40 nm) evenly into carbon nanofibers by optimizing the Joule heating method to obtain lower interfacial energy.^[62e] The Ag NPs decrease the nucleation barrier of Li and regulate homogeneous deposition of Li on the carbon fibers to avoid dendrite formation (Figure 10b). As a result, a stable and reversible LMA with an ultralow overpotential (≈ 0.025 V) and long cyclic stability is produced.

Non-noble metal single-atom catalysts is a kind of material with monoatoms dispersed on a solid substrate, which can make maximize use of metal atoms to deposit Li in LMAs. These materials contribute to the uniform deposition of Li metal during the electroplating and stripping processes, and prevent the formation of dendrites, thus improving the electrochemical performance of LMAs. Yan et al. have studied single-atom Fe incorporated into N-doped carbon (Fe_{SA}-N-C) to produce lithiophilic sites for Li metal and the nucleation overpotential decreases from 18.6 to 0.8 mV (Figure 10c).^[62h] The strong affinity between Li⁺ and Fe_{SA}-N-C is verified on the atomic level by molecular dynamics simulation. Uniform dispersion of Fe_{SA}-N-C leads to homogeneous electroplating/stripping of Li and uncontrolled growth of Li dendrites is mitigated. The full cell consisting of the Fe_{SA}-N-C/Li composite anode exhibits excellent cyclic stability with capacity retention of 89.3% after 200 cycles.

Besides metal seeds, other compounds can reduce the interfacial energy for nucleation of metallic Li.^[62k,122–123,127] Nonmetallic elements such as N, O, S, and Se have higher binding

energy with Li, so that the interfacial energy can be reduced and the number of active sites for Li nucleation can be increased. Zhai et al. have proposed a 3D framework comprising g-C₃N₄/graphene/g-C₃N₄ sandwich-like nanosheets (Figure 10d).^[62k] The g-C₃N₄ layer not only supplies a large number of sites to accelerate nucleation of Li due to N species, but also enhances uniform deposition of Li in the van der Waals gap between graphene and g-C₃N₄. The amorphous g-C₃N₄ gives rise to high homogeneity without fragile grain boundaries further ensuring the structural stability during deposition of Li metal. The 3D g-C₃N₄/G/g-C₃N₄ electrode after Li deposition is promising for LMAs as exemplified by a high capacity of 5.0 mAh cm⁻², long cycling lifetime (more than 500 cycles), and high CE (average 99.1%).

The Li₂S-rich protection layer homogenizes the distribution of Li⁺ and leads to the diffusion of uniform ion flux to the surface of LMA, which makes the uniform nucleation of Li metal and inhibits the growth of Li dendrites. To achieve this goal, Yu et al. have prepared the edge-enriched ultrathin MoS₂ embedded carbon nanofiber (PCNF/MoS₂) framework as a protective layer to stabilize LMAs.^[123] After prelithiation, the spontaneous chemical reaction between MoS₂ and Li leads to in situ formation of Mo and Li₂S on the surface of the Li foil. The overpotential of Li nucleation decreases and uniform deposition of Li is enhanced along the cavity of the 3D framework so that growth of Li dendrites is restrained. Moreover, Li₂S is an effective additive to accelerate the formation of uniform and

robust SEI films with excellent chemical stability and high ionic conductivity. The PCNF/MoS₂-Li LMAs show a long cycling lifetime of over 750 h at 1 mA cm⁻² with a capacity of 1 mAh cm⁻².

In general, the current LMAs can only work stably at low current densities and limit cycles due to the risk of dendrite growth and the interface instability. To overcome this dilemma, conductive host and nucleation regulation are two strategies to accelerate interface kinetics while maintaining the interface stability. The conductive host minimizes the “space charge” effect, homogenizes Li⁺ flux, and effectively buffers the formation of Li dendrites. In terms of nucleation regulation, the lithiophilic interface can be used to reduce interfacial energy, and achieve uniform deposition of Li during electrochemical cycling. In this case, the ideal host for LMAs should possess lithiophilic interface with a suitable specific surface area in order to avoid the formation of dendrites via reducing the “space charge” effect and the nucleation barrier of Li metal.

2.3. Electrolytes

Electrolyte is an important component that affects the transport of Li⁺ during the electrochemical cycling process and plays a crucial role in the performance of battery. In Li-S systems, the preferred electrolyte should have excellent Li conductivity, low LiPSs solubility, and outstanding stability for the S cathode and Li anode.^[128] Although solid electrolytes can overcome issues such as shuttle and safety, their typical drawbacks include low conductivity, poor interfacial compatibility and complicated synthesis.^[129] Liquid electrolytes do not have these problems occurred in solid electrolyte. Unfortunately, liquid electrolytes (including solvent and Li-salt) react with the S cathode and LMA, which degrades battery performance.^[130] On the other hand, the reactions between electrolyte and electrodes sometimes promote the formation of stable SEI and cathode electrolyte interface (CEI) films, thus contributing to the stability of battery performance. Therefore, the current study is to improve the performance of Li-S batteries by optimizing the liquid electrolytes composed of solvents, salts, and additives. In this section, different modification strategies of electrolyte are summarized as follows.

2.3.1. Solvents and Li-Salts

The ether-based solvents are widely used for Li-S batteries due to their high solubility and excellent chemical stability to LiPSs.^[130-131] However, these ether-based solvents have different natural characteristics. 1,2-dimethoxyethane (DME) has high LiPSs solubility and high kinetics for the LiPSs, but prefers to react with LMAs. In contrast, 1, 3-dioxolane (DOL) has a lower LiPSs solubility, but contributes to the formation of a more stable SEI on the LMA surface.^[132] These different natural properties make it hard for a single solvent to meet all the requirements of Li-S batteries. To combine the advantages of different solvents, researchers have studied the binary and ternary ether-based solvents for high-performance Li-S batteries.^[133] The most common solvent currently used in Li-S batteries is the mixture of DME and DOL with equal volume ratio, which is suitable for various S cathodes.^[130]

Compared with the current popular ether-based solvents, fluorinated ether is a promising alternative due to its low viscosity, low flammability and moderate LiPSs solubility. More importantly, the fluorinated ether can promote the formation of inorganic components in SEI and CEI films, which significantly prevent the shuttle effect. Azimi et al. have used an organo-fluorine compound of 1,1,2,2-tetrafluoroethyl-2,2,3,3-tetrafluoropropyl ether (TTE) as the solvent for Li-S batteries.^[134] The result shows that the diffusion of LiPSs is buffered by the fluorinated ether, and the Li-S batteries show stable discharge capacity of 1100 mAh g⁻¹ for 50 cycles with a CE of 98%. Later, Chen et al. have constructed a rechargeable prelithiated graphite/S battery using ether bis(2,2,2-trifluoroethyl) ether (BTFE)/DOL solvent.^[135] The fluorinated ether solvent effectively reduces the solubility of LiPSs, thus retarding the shuttle of LiPSs and improving the capacity retention of S cathodes. In addition, the low viscosity and good wettability of BTFE/DOL solvent accelerates the electrochemical reaction kinetics of Li-S batteries. Notably, the electrolyte facilitates the formation of a stable SEI layer on the graphite surface, ensuring Li insertion/extraction of the graphite anodes to achieve improved safety and better cycle life. Therefore, the constructed Li-S battery using 1.0 M LiTFSI DOL/BTFE (1:1, v/v) as the electrolyte has a high S-specific capacity of ≈1000 mAh g⁻¹, and an excellent capacity retention of >65% after 450 cycles at 0.1 C. Even when the S loading is increased to ≈7 mg cm⁻², the constructed Li-S battery can still provide a high discharge capacity of about 1200 mAh g⁻¹ at 0.05 C.

Ether-based electrolytes have been widely used in Li-S batteries and have improved the electrochemical performance of Li-S batteries effectively. However, the inflammability property of ether-based solvents is a major shortage, especially at high temperature.^[130] Carbonate-based solvents are successful electrolyte systems for LIBs. They have been introduced into Li-S batteries due to their low LiPSs solubility, effective LMA passivation, high ionic conductivity and excellent electrochemical stability.^[136] However, most carbonate solvents are not suitable for S cathodes because of the side-reactions between the carbonates molecules and the soluble LiPSs, which leads to severe performance degradation of batteries with a limited cycles.^[137] Nowadays, this dilemma has been broken, providing new opportunities for Li-S batteries. For example, the electrolytes containing mixture of DEC and EC solvents deliver better cycle performance in the Li-S system due to the different reaction mechanism. Shi et al. have constructed a full battery consisting of an S@pPAN cathode, a prelithiated SiO_x/C anode and a DEC/EC electrolyte with outstanding cycle performance (reversible capacity of 616 mAh g⁻¹ after 100 cycles at 0.1 A g⁻¹).^[138] In order to further improve the cycling performance of the carbonate-based electrolyte, the coupling of FEC with different S cathodes has been studied. Compared with the EC solvent, FEC can catalyze the formation of dense and stable SEI film, which prevents the corrosion and the dendrite growth of LMA.^[139] In addition, the lower desolvation energy of Li⁺ in FEC-based electrolyte accelerates the reaction between the Li⁺ and S in carbon matrix, thus preventing the dissolution of LiPSs from cathode.^[140]

Li-salt is another important part of the electrolyte for Li-S batteries, which has an important effect on the Li⁺ conductivity

of electrolyte.^[136,141] A series of Li-salts (e.g., LiClO₄, LiPF₆, LiCF₃SO₃, and lithium bis(trifluoromethane sulfonyl) imide (LiTFSI)) commonly used in LIBs have been widely studied in Li-S batteries. Specifically, studies on Li-salts for Li-S batteries mainly focus on LiTFSI, because it has excellent electrochemical stability, high ionic conductivity and low reactivity with LiPSs.^[130] However, single Li-salt has its own limitations, so electrolytes containing binary salts can be used to improve performance of electrolyte systems. For example, introducing the LiFSI into the LiTFSI-based electrolytes can increase the ionic conductivity of electrolyte and decrease the viscosity of electrolyte. Kim et al. reported that the reduction of LiFSI at high temperature facilitates the formation of an in situ protective coating on the cathode/anode surfaces.^[142] The protective layer can limit the reaction between LMA and LiPSs, thus effectively buffering the shuttle effect. However, the Li-salts of LiTFSI, LiFSI, and LiCF₃SO₃ have similar structures and can corrode Al current collector. In this case, lithium oxalyldifluoroborate (LiODFB) can be used as an additive in the LiFSI-based electrolytes to promote the formation of a passive film on the surface of Al current collector, thereby inhibiting the corrosion of Al current collector by the electrolytes.^[143] However, the corrosion of Al collector by electrolytes still exists and needs further study.

2.3.2. Additives

Expert for solvents and Li-salts, additives are generally preferred to provide additional stable inorganic SEI components to prevent the side-reaction between the LiPSs and fresh metallic Li in Li-S batteries.^[144] LiNO₃ is the commonly used additive because it can facilitate and participate in the formation of the passivation layer, thus limiting the contact between the Li metal and LiPSs.^[132a] Aurbach et al. have studied the composition of the LMA surface and found that the LiNO₃ additive can promote the formation of inorganic Li_xNO_y and Li_xSO_y species, which in turn passivate the LMA, thus blocking the side-reaction.^[145] Furthermore, the DFT calculations show that the LiNO₃ additive can catalyze the conversion of soluble LiPSs into elemental S at the end of oxidation process.^[146] However, the strong oxidation of NO₃⁻ and the irreversible consumption of LiNO₃ during SEI formation result in the increase of SEI resistance, which limits the development of LiNO₃. Kim et al. have added metal iodides such as LiI, MgI₂, AlI₃, TiI₄, and SnI₄ to ether-based electrolytes and studied the effects of these additives.^[147] These metal iodides are co-deposited on the surface of LMA to promote formation of stable SEI film and the viscosity of the electrolyte is increased by polymerization. As a result, the Li-S batteries assembled with electrolyte additives such as LiI, MgI₂, AlI₃, TiI₄, and SnI₄ show high capacities of 690, 680, 573, 556, and 501 mAh g⁻¹, respectively, after 50 cycles, which provides a feasible method for the design of novelty electrolytes for advanced Li-S batteries.

The passivation layer formed by transition metal cation additives also protects the LMA and improves the performance of Li-S batteries. Zeng et al. have studied the effects of transition metal cations (e.g., Zn²⁺, Cu²⁺, Co²⁺, Ni²⁺, and Mn²⁺) on the passivation of LMA in the Li-S system, and the rate capacity and

CE improve with the addition of transition metal cations.^[148] At 0.1 C, the initial capacities of Li-S batteries with Zn²⁺ and Cu²⁺ additives are 1595 and 1560 mAh g⁻¹, respectively. After 500 cycles, the capacities retention of Li-S batteries with Zn²⁺ and Cu²⁺ additives are 69.1% and 63.4%, respectively. The electrochemical performance of Li-S batteries with Zn²⁺ and Cu²⁺ additives are better than that without additives (initial capacity of 1510 mAh g⁻¹ and capacity retention of 57.5%). In addition, due to the addition of transition metal cations, a smoother and harder SEI films is more easily formed on the surface of LMA, which blocks the parasitic reactions between LMA and LiPSs as well as the organic electrolyte, thus reducing the consumption of the active materials and improving the CE of batteries. Notably, the uniform and good mechanical strength SEI film can reduce the formation of Li dendrites and improve the cyclic stability of batteries. In details, the effects of transition cations on the performance of Li-S batteries are as follows: Zn²⁺ > Cu²⁺ > Co²⁺ > Ni²⁺ > Mn²⁺.

Phosphorus pentasulfide (P₂S₅) is another promising additive for Li-S batteries, which has attracted much attention due to its ability to form passivation layer and increase the solubility of Li₂S. Lin et al. have added P₂S₅ as an additive to the electrolyte and found that a highly protective passivation layer is formed on the surface of LMA.^[149] The passivation layer significantly improves the electrochemical properties of the S cathode during the electrochemical cycling. Besides, P₂S₅ combines with Li₂S to form Li₂S_x/P₂S₅ complex, which is soluble in organic TEGDME. It greatly accelerates the conversion of S species during the battery cycling. As a result, the Li-S batteries have high CE and excellent cycling performance (70% capacity retention at 900 mAh g⁻¹ over 40 cycles at 0.1 C). Although additives can improve the performance of Li-S batteries, the reaction between additives and LiPSs may result in the loss of active materials.

Obviously, the solution of LiPSs is the dominate factor affecting the performance of batteries, such as the CE, cyclic stability and rate capability. The composition of solvent, Li-salt and additive is the main direction of electrolyte design for Li-S batteries. The main principle of electrolyte design is to obtain stable SEI and CEI films by adjusting the composition of the solvent, Li-salt and additive, so as to significantly improve the electrode structure stability of Li-S batteries. In addition, the reaction kinetics of Li-S batteries can be accelerated by optimizing the composition of electrolyte, which will further improve the electrochemical performance.

2.4. Functional Separators

As an indispensable component of Li-S batteries, separator can separate cathode from anode, provide channels for the migration of Li⁺ and prevent the transfer of electrons, thus efficiently preventing the internal short circuit of batteries.^[150] In fact, some LiPSs can also cross the separators and attach to the LMAs during the electrochemical cycling, resulting in the failure of batteries. A lot of efforts have been made on functional separators with adsorption effect and separation effect to improve the performance of Li-S batteries.^[151] However, the conversion from LiPSs to the final product Li₂S is still sluggish,

which severely limits the electrochemical performance of Li–S batteries. In order to improve the conversion kinetics of LiPSs, catalysts have been introduced into the functional separators to avoid the accumulation of LiPSs on the surface of separators and accelerate the transportation of Li⁺ in recent years. It is worth noting that the functional separator with catalyst can simultaneously provide absorption ability for LiPSs. Therefore, the functional separator with catalyst firstly adsorbs LiPSs on its surface and further accelerates the conversion of LiPSs through catalytic effect, thus improving the electrochemical performance of Li–S batteries.

A variety of catalysts (e.g., metallic catalysts, and metal oxides) can catalyze the conversion of LiPSs, and have been used in the modification of separators. Cheng et al. have constructed a functional separator by coating Co-embedded N-doped porous carbon nanosheets and graphene (Co–N_x@NPC/G) on the surface of commercial polypropylene separator.^[152] The encapsulation of Co by N-doped porous nanosheet can avoid the undesirable side reactions caused by its high catalytic activity. The coating layer can not only inhibit the shuttle effect of LiPSs by chemisorption, but also accelerate the conversion of intercepted LiPSs. As a result, the assembled coin-type cell has high capacities of 1180, 1040, 905, and 801 mAh g⁻¹ at 0.5, 1.0, 3.0, and 5.0 C, respectively. The catalyst-containing separator can also significantly improve the utilization of S. When the CNT/S composite with 90% S content is used as the cathode, the assembled battery shows a high initial capacity of 1103 mAh g⁻¹ with high areal capacity of 2.87 mAh cm⁻² at the current density of 0.2 C. In addition, the cell containing Co–N_x@NPC/G modified separator and freestanding carbon nanofibers/S cathode shows a high capacity of 1190 mAh g⁻¹ and a volumetric capacity of 1136 mAh g⁻¹ with high S content of 78% and S loading of 10.5 mg cm⁻². Similarly, Song et al. have proposed a strategy to fabricate high-performance Li–S batteries via employing a 3D network-like nanocomposite of Co/NCNS/CNT to prepare functional separator.^[153] Due to the good sulphophilicity, outstanding conductivity as well as high catalytic activity of metallic Co, the functional separator can effectively improve the electrochemical performance of Li–S batteries. As a result, the assembled battery shows a high initial capacity of 972.4 mAh g⁻¹ at 2 C with an S loading of 2.0 mg cm⁻² and excellent cyclic stability. When the S loading reaches 5 mg cm⁻², a capacity of 522.1 mAh g⁻¹ is maintained after 500 cycles under the current density of 1 C.

It is well known that some metal oxides also show a catalytic effect toward polysulfides. Very recently, Yu et al. have prepared oxygen vacancy-rich MnO nanoflakes/N-doped carbon nanotubes (MnO-OVs/NCNTs) modified separator to improve the electrochemical performance of Li–S batteries.^[154] The polar MnO acts as anchor to restrict the diffusion of LiPSs via chemical adsorption. In addition, the oxygen vacancies introduced into MnO can regulate the electronic structure and provide extra active site for improving the adsorption ability for LiPSs, accelerating conversion of LiPSs and increasing the electronic conductivity. Furthermore, the MnO-OVs/NCNTs layer coating on the surface of separator interrupts the diffusion of LiPSs while acts as an upper collector to trap S species simultaneously. Due to these advantages, the MnO-OVs/NCNTs modified separator effectively improves the utilization of S. The assembled cell delivered an ultrahigh capacity of 1516 mAh g⁻¹ at

0.1 C, improved cyclic stability (500 cycles at 1 C) and rate performance 550 mAh g⁻¹ at 3 C.

Up to now, a lot of modification studies have been carried out on the separator to boost the electrochemical performance of Li–S batteries. However, most of these studies are focused on solving the problems of cathode, and less attention is paid to the problems of metal anode. It has been confirmed that the problems of metal anode can be solved by modifying the anode. Therefore, if the modified separator can overcome the problems of both cathode and anode, it will further improve the electrochemical performance of the metal–S batteries. Such research strategies of modified separator deserve further attention.

3. Na–S Batteries

Recently, great progress has been made in the development of high-performance Li–S batteries for practical applications. However, owing to the relatively high cost and uneven geographical distribution of Li, Li-free M–S batteries that meet the needs for large-scale energy storage have aroused interests.^[155] Na is the most promising alternative to Li and being the fourth most abundant element on earth, and it does not have geographical limitations (Figure 11a).^[156] RT Na–S batteries have a similar working mechanism as Li–S batteries due to the similar chemistry.^[157] During the discharging process of RT Na–S batteries, the Na anode is oxidized to form Na⁺ and electrons. Na⁺ ions move through the electrolyte to the S cathode and electrons exit through the external circuit to the S cathode. At the same time, S receives Na⁺ and electrons at the cathode and is reduced to NaPSs. The S cathode in RT Na–S batteries undergo multistep reduction from S₈ to Na₂S during discharging (Figure 11b), similar to that in Li–S batteries. Elemental S is first reduced to soluble long-chain intermediates (Na₂S_n, 4 ≤ n ≤ 8) at a high voltage window (1.65–2.2 V) and then further reduced to solid Na₂S₂/Na₂S at a lower voltage (1.2–1.6 V).^[158] During the charging process, Na₂S is gradually oxidized to S₈ through a reverse path eventually forming a reversible cycle. The RT Na–S batteries can have a high theoretical capacity of 1672 mAh g⁻¹ and is competitive in low-cost and large-scale energy storage.

RT Na–S batteries face similar challenges as Li–S batteries and these challenges are exacerbated by the unique characteristics of RT Na–S batteries. As an anode, Na is more active than Li and so the SEI films of Na metal formed in conventional liquid electrolytes are unstable, giving rise to formation of Na dendrites, corrosion of the Na anode surface, and failure of cell. As for the cathode, the solubility of NaPSs is higher than that of LiPSs, thereby making the shuttle effect of NaPSs in RT Na–S batteries more pronounced than Li–S batteries. In addition, the volume change of the S cathode in RT Na–S batteries is larger than that in Li–S batteries during charging and discharging and the structural stability of the S cathode in RT Na–S batteries is more challenging. Finally, the charge transfer and electrochemical reaction kinetics of RT Na–S batteries are slower than those of Li–S batteries due to the larger size of Na⁺, which creates another problem during charging/discharging especially at large current densities.

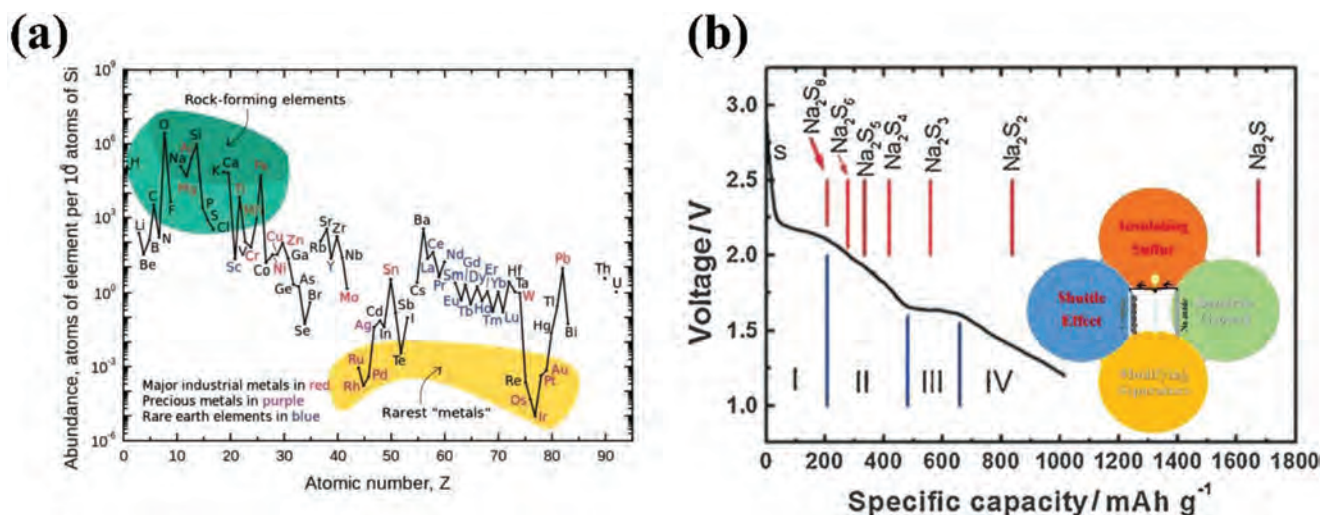


Figure 11. a) Relative elemental abundance in the earth crust. Reproduced with permission.^[156] Copyright 2013, Royal Society of Chemistry. b) Theoretical, practical discharge capacities and Challenges of RT Na-S batteries. Reproduced with permission.^[158] Copyright 2014, Wiley-VCH.

3.1. Sulfur Cathodes for RT Na-S Batteries

Owing to the similarity between RT Na-S and Li-S batteries, the research and development of high-performance RT Na-S batteries can take advantages of the technologies developed for Li-S batteries. Park et al. have proposed an RT Na-S battery with a gel polymer with high Na⁺ conductivity as the electrolyte and there have been efforts to buffer the diffusion of NaPSs.^[159] Porous carbon has been used as the host materials for RT Na-S batteries to physically capture NaPSs and improve the conductivity of the S cathode. For example, Wang et al. have used interconnected mesoporous carbon hollow nanospheres (iMCHS) with a large tap density as the S host for RT Na-S batteries.^[160] The iMCHS block diffusion of NaPSs in the inner hollow nanospace via physical adsorption and also buffer the volume change of the interior S. The interconnected mesoporous carbon structure provides continuous electron transfer channels for S and consequently, the S electrode has a reversible capacity of 292 mAh g⁻¹ after 200 cycles at 0.1 mA g⁻¹. However, because of the weak interactions between nonpolar carbon and NaPSs, physical capturing of NaPSs has limited effects on the electrochemical properties of RT Na-S batteries and it is necessary to identify new host materials and structure to improve the electrochemical performance of RT Na-S batteries.

Similar to Li-S batteries, electrocatalysts have also been introduced into the study of RT Na-S batteries. To reveal the fundamental electrocatalytic effect, Ye et al. have prepared a Mo₅N₆ cathode material and measured the *E_a* via electrochemical impedance spectroscopy (EIS).^[161] By fitting values of charge transfer resistance in the Arrhenius equation, the *E_a* of the S/Mo₅N₆ electrode is 0.53, 0.57, and 0.60 eV at 2.5, 2.0, and 1.5 V, respectively, which are lower than those of the S/MoN electrode (0.64, 0.69, and 0.79 eV), the S/Mo₂N electrode (0.67, 0.71, and 0.77 eV) and S/C electrode (0.63, 0.57, and 0.82 eV). For the final conversion to Na₂S₂/Na₂S in the voltage range of 1.0 to 0.5 V, the S/Mo₅N₆ exhibits significantly lower values of 0.73 and 0.74 eV in comparison with those of S/MoN (0.78 and 0.80 eV), S/Mo₂N (0.80 and 0.84 eV) and S/C

electrode (0.79 and 0.89 eV). Furthermore, the electrodeposition kinetics of Na₂S on various molybdenum nitrides are calculated by DFT calculation. A three-step reaction pathway is constructed for converting Na₂S₂ to Na₂S on different molybdenum nitrides, including 1) adsorption of Na₂S₂; 2) Na₂S₂ dissociates to form adsorbed Na* and NaS₂*; 3) two NaS* formation following simultaneous NaS₂* dissociation and Na-S bond formation. From the thermodynamic point of view, Mo₅N₆ shows an optimal free energy value of -0.23 eV for the Na₂S₂ dissociation step, and MoN shows the optimal free energy value of -0.05 eV for the NaS₂* dissociation step, demonstrating that the Mo₅N₆ and MoN have similar Na₂S electrodeposition activity. From a kinetic viewpoint, the Mo₅N₆ surface displays a substantially lower energy barrier (0.48 eV) than those of other molybdenum nitrides (0.58 eV for MoN and 1.06 eV for Mo₂N) when the kinetics of NaS* formation step is considered, indicating that the most favorable electrodeposition efficiency occurs on the surface of Mo₅N₆. These findings indicate that the Mo₅N₆ significantly improves the overall kinetics and Na₂S electrodeposition. This work reveals that the application of electrocatalyst can significantly overcome the challenges of RT Na-S batteries.

3.1.1. Metal-Based Nanomaterials

Similar to Li-S batteries, electrocatalytic effects can be introduced to the S cathode in RT Na-S batteries to improve the cyclic stability and kinetics. Zhang et al. have decorated hollow carbon nanospheres with atomic cobalt species for electrocatalytic reduction of NaPSs to Na₂S (**Figure 12a**).^[162] The atomic Co, including sing-atom Co and Co clusters, form Co-S chemical bonds with S to restrict mobilization of S and NaPSs and by means of in situ Raman scattering, in situ XRD, and theoretical calculation, atomic Co is observed to expedite reduction of NaPSs to Na₂S and impede the shuttle effect of NaPSs. In addition, the micropores of the hollow carbon nanospheres act as the traction of atomic Co and provide channels for the diffusion of Na⁺. The S cathode shows a high initial reversible capacity of

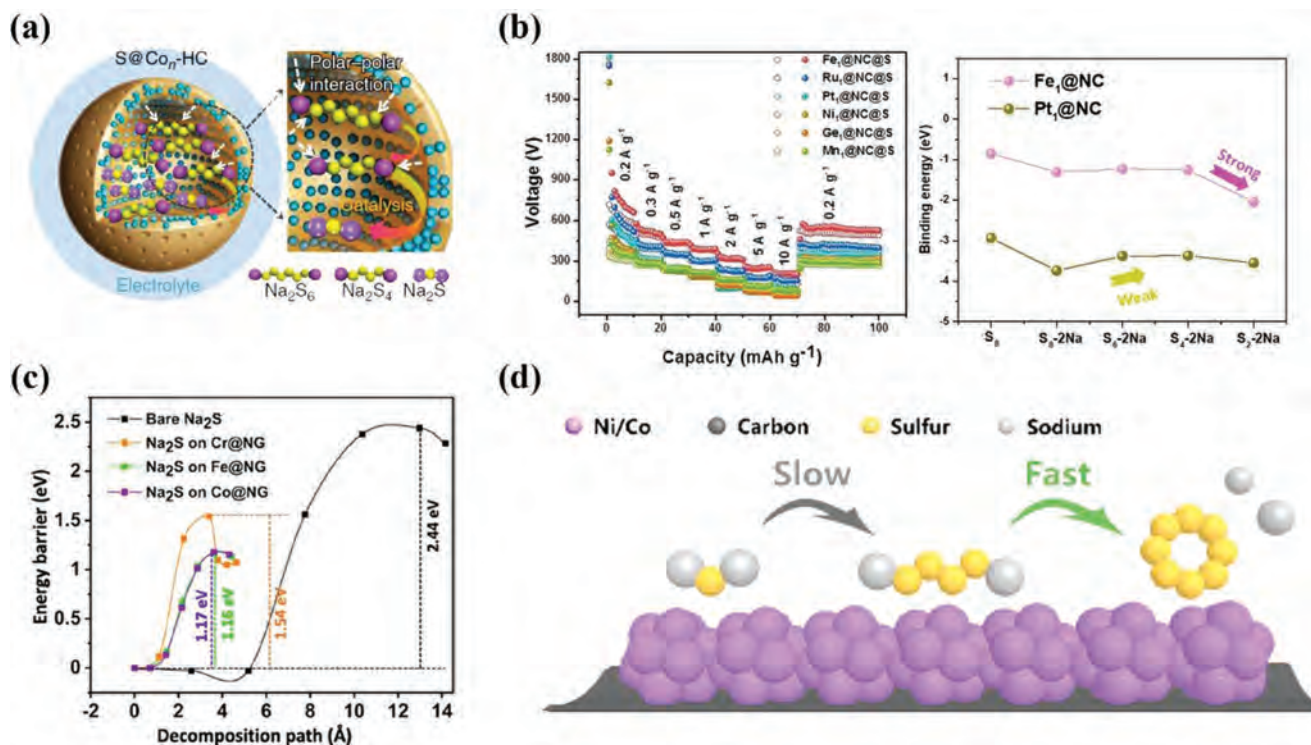


Figure 12. a) Electrocatalysts with hollow carbon decorated with atomic Co metals for RT Na–S batteries. Reproduced under the terms of the CC-BY Creative Commons Attribution 4.0 International license (<https://creativecommons.org/licenses/by/4.0/>).^[162] Copyright 2018, The Authors, published by Springer Nature. b) Study of single-atom catalysts for RT Na–S batteries. Reproduced with permission.^[164] Copyright 2020, Wiley-VCH. c) Decomposition barrier of bare Na₂S and Na₂S on TM@NG substrates. Reproduced with permission.^[165] Copyright 2021, American Chemical Society. d) Schematic diagram of the conversion processes on Ni/Co bimetal. Reproduced with permission.^[166] Copyright 2021, American Chemical Society.

1081 mAh g⁻¹ with an initial CE of 52.1% in conjunction with excellent cycling characteristics (508 mAh g⁻¹ after 600 cycles). Zhang et al. have also loaded a series of transition nanoclusters (e.g., Ni, Fe, and Cu) on hollow carbon nanospheres as host materials for S in RT Na–S batteries.^[162] Molecular dynamics simulation based on ab initio calculation confirms the electrocatalytic effect in conversion of NaPSs. In addition, Liu et al. have designed a novel host material based on tungsten nanoparticles embedded in N-doped graphene (W@N-G) for RT Na–S batteries.^[163] Specifically, the incorporation of tungsten nanoparticles drastically improves the chemisorption of NaPSs and catalyzes the transformation of NaPSs in RT Na–S batteries. With a host weight ratio of 9.1 wt% in the cathode (corresponding to S loading of 90.9%), the W@N-G/S cathode with a S areal loading of 1 mg cm⁻² shows a high discharge capacity of 1160 mAh g⁻¹ at 0.2 C in the second cycle. When the S loading reaches 3.6 g cm⁻², the W@N-G/S cathode still has a high discharge capacity of 1050 mAh g⁻¹ in the second cycle, and maintains a high capacity of 883 mAh g⁻¹ after 100 cycles, indicating that the W@N-G/S cathode is suitable for practical application.

As mentioned above, single-atom catalysts maximize the active sites of atoms and improve the electrocatalytic properties of LiPSs. Lai et al. have synthesized a series of single-atom metals (e.g., Fe, Mn, Pt, and Ru) on carbon as host materials for RT Na–S batteries.^[164] These single-atom catalysts play a significant role in improving the electrochemical performance of RT Na–S batteries (Figure 12b). Jayan et al. have studied

the electrocatalytic effects of single-atom metals on RT Na–S batteries by DFT calculation.^[165] Hybridization of the transition-metal-3d orbitals in the transition metal single-atom has sufficient binding energy for hybridization of the S-2p orbitals in NaPSs, while the original graphene and N-doped graphene have no obvious anchoring effects on NaPSs (Figure 12c). The density of state calculation indicates that SACs adsorbed S₈ has significant metallic behavior. The binding energy between NaPSs and ether-type electrolyte is smaller than that between the single-atom catalysts, indicating that the single-atom catalysts have obvious adsorption effects on NaPSs to inhibit the shuttle effect of NaPSs. In addition, SACs reduce the decomposition barrier of Na₂S demonstrating the electrocatalytic effects of single-atom catalysts in reversible conversion of NaPSs.

In addition to atomic catalysts, bimetal catalysts are adopted by RT Na–S batteries and have the potential in multi-step control of catalytic conversion of NaPSs. Ma et al. have modified carbon nanospheres with bimetal Co/Ni nanoparticles as the host materials for RT Na–S batteries (Figure 12d).^[166] The results of galvanostatic intermittent titration (GITT) show that the overpotential of the cathode with a Ni/Co molar ratio of 1:2 (S@Ni/Co-C-12) is smaller than the cathode with a Ni/Co molar ratio of 1:1 and 2:1 during the whole discharge/charge process. At the same time, the S@Ni/Co-C-12 has a highest Na⁺ diffusion coefficient during the charge/discharge process, indicating that the Na⁺ rapid transfer of Na⁺ in the carbon channels is due to the existence of Ni/Co bimetal nanoparticles. These

results reveal that the minimized polarization and resistance of S@Ni/Co-C-12, thus enabling the ion transfer for rapid S transformation. During charging, the conversion rate of Na₂S to NaPSs is slowed but that of NaPSs to S₈ is accelerated by adjusting the metal ratio of Co/Ni nanoparticles. This strategy reduces the shuttle effect of NaPSs and improves the kinetics of RT Na-S batteries. The electrode shows good cycling performance (813.5 mAh g⁻¹ at 0.5 C after 200 cycles) and a capacity of 391.6 mAh g⁻¹ at 9 C. FeNi₃ decorated hollow carbon spheres (FeNi₃/HC) have been prepared as the host materials for S in RT Na-S batteries and first-principle calculation discloses that Fe regulates the electronic structure of Ni.^[40] The different electronegativity between Fe and Ni facilitates transfer of electrons from Fe to Ni and reduces the reaction energy barrier of Na₂S₄ to Na₂S, thus improving the kinetics of Na₂S₄ to Na₂S. The electrode based on FeNi₃ decorated hollow carbon spheres has excellent cyclic stability and rate performance and the deposition rate of Na₂S on the FeNi₃/HC electrode is larger. The results show that FeNi₃ accelerates conversion of NaPSs.

3.1.2. Metal Compounds

In addition to metal-based catalysts, metal oxides are commonly used to improve the redox kinetics of NaPSs conversion. Large number of active sites on the surface of metal oxides accelerates conversion of NaPSs and improves utilization of S. Besides, the polar nature of metal oxides provides the ability to

capture NaPSs to improve the cyclic stability of RT Na-S batteries. However, metal oxides are mostly insulators and metal oxides should be combined with a conductive carbon framework to ensure good electron transfer in RT Na-S batteries. Metal oxides have been studied for their excellent catalytic activity in RT Na-S batteries due to their specific intrinsic electronic structure and energy band structure. The M-S and Na-O bonds produce strong chemisorption between metal oxides and NaPSs to mitigate shuttling of intermediates. Du et al. have prepared rGO/VO₂ nanoflowers as the multifunctional hosts for S in RT Na-S batteries.^[37] As shown in Figure 13a, the VO₂ nanoflowers serving as the catalytic centers for the transformation of NaPSs are uniformly distributed on rGO which acts as the conductive network in the cathode. Owing to the good electrical conductivity and catalytic characteristics for NaPSs, the RT Na-S batteries composed of the rGO/VO₂/S cathode exhibits a small overpotential and cycling performance of 400 mAh g⁻¹ after 200 cycles with a CE of over 99%. Recently, Kumar et al. have reported that indium tin oxide nanoparticles, a conductive metal oxide decorated on activated carbon cloth (ITO@ACC), act as an electrocatalytic host to immobilize the higher-order NaPSs and accelerate the conversion of NaPSs.^[167] The EPR spectroscopy shows that the single-electron-trapped oxygen vacancies present in the ITO crystal undergo a free-radical coupling process with trisulfur radical monoanions (S₃⁻), and can accelerate the transformation of higher-order NaPSs. As a result, the prepared RT Na-S coin cells with ITO@ACC shows a high capacity of 1167 mAh g⁻¹ at 0.2 C. When the S

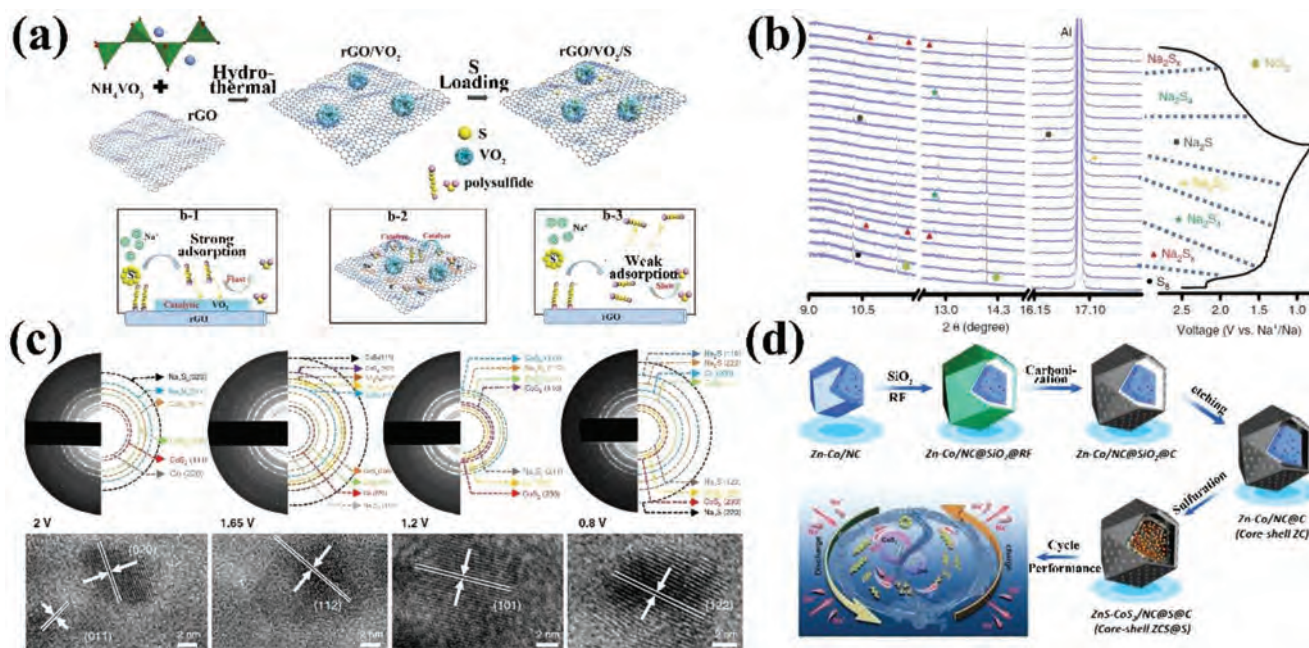


Figure 13. a) Schematic of the preparation and advantages of the rGO/VO₂/S composite. Reproduced with permission.^[37] Copyright 2020, American Chemical Society. b) In situ synchrotron XRD patterns of the RT-Na/S battery containing a NiS₂@NPCTs/S electrode with the corresponding galvanostatic charge/discharge curves at 200 mA g⁻¹. Reproduced under the terms of the CC-BY Creative Commons Attribution 4.0 International license (<https://creativecommons.org/licenses/by/4.0>).^[33] Copyright 2019, The Authors, published by Springer Nature. c) Ex situ high-resolution transmission electron microscopy/selected area electron diffraction of S@BPCS electrode at different discharge voltages. Reproduced under the terms of the CC-BY Creative Commons Attribution 4.0 International license (<https://creativecommons.org/licenses/by/4.0>).^[168] Copyright 2020, The Authors, published by Springer Nature. d) Schematic illustration of the synthesis of core-shell nanoarchitecture and multisulfiphilic cathode. Reproduced with permission.^[169] Copyright 2020 American Chemical Society.

loading reaches 6.8 mg cm^{-2} , the cathode exhibits a high initial reversible capacity of 684 mAh g^{-1} and maintains a high reversible capacity of 445 mAh g^{-1} after 1000 cycles.

Metal sulfides are widely used in Li–S batteries due to the excellent catalytic activity in the electrochemical reactions and are expected to improve the electrochemical properties of RT Na–S batteries.^[56b] Yan et al. have designed a multifunctional S host to achieve high adsorption and efficient transformation of NaPSs by encapsulating NiS_2 onto N-doped CNTs ($\text{NiS}_2@ \text{NPCTs}$) (Figure 13b).^[33] Under vacuum conditions, the nickel salt and thioacetamide are injected into the interior pores of the CNTs by the capillary effect. The NiS_2 nanocrystals are uniformly distributed inside the carbon matrix and have an average size of 8.3 nm. In the in situ synchrotron XRD spectrum, the Na_2S_2 signal disappears during charging, indicating that NiS_2 accelerates the transformation of NaPSs. DFT calculation shows that the binding energy between NiS_2 and Na_2S (2.4 eV) is larger than that between NiS_2 and NaPSs (0.79 eV) and fast conversion of NaPSs is related to NiS_2 . The binding energy of NiS_2 to NaPSs is stronger than that of N-doped carbon (0.57 eV), demonstrating NiS_2 has excellent adsorption capacity for NaPSs. As a host for S in RT Na–S batteries, the $\text{NiS}_2@ \text{NPCTs}$ electrode shows impressive cycling property with a capacity of 401 mAh g^{-1} after 750 cycles at 1 A g^{-1} . Aslam et al. have prepared CoS_2 hollow polar bipyramid prisms as host materials for S and used it as cathode materials in RT Na–S batteries. The interactions between CoS_2 and NaPSs are investigated by various in/ex situ characterization techniques and DFT calculation (Figure 13c).^[168] Strong chemical adsorption between CoS_2 and NaPSs not only prevents the shuttle effect of NaPSs but also accelerates the kinetics of the electrochemical reaction, thereby ensuring direct conversion of long-chain NaPSs into short-chain NaPSs. In addition, the bipyramid prism structure provides wide hollow cavity for S loading and NaPSs capture. The electrode shows outstanding cyclic stability (675 mAh g^{-1} after 800 cycles at 0.5 C) and rate performance (349 mAh g^{-1} at 3 C). In addition, CoSe_2 and CoTe_2 have been prepared by a similar method and experiments, revealing a universal strategy for the adoption of other transition metal dichalcogenides in RT Na–S batteries.

The different electronic structures and binding ability of metal sulfides determine whether they can be used as multifunctional active sites for the conversion of NaPSs. Liu et al. have prepared a bimetallic MOF with a porous core–shell structure and multisulfophilic sites for RT Na–S batteries.^[169] The porous carbon structure provides space to accommodate S and buffers the volume expansion of S during electrochemical cycling. The multisulfophilic sites including ZnS and CoS_2 provide active sites for the conversion of NaPSs (Figure 13d). Zn–S and Co–S chemical bonds are formed during discharging and charging, indicating that ZnS and CoS_2 lead to chemisorption of NaPSs to prevent diffusion of NaPSs in RT Na–S batteries. DFT calculation reveals that the discharging process is thermally more favorable under catalysis of CoS_2 . However, Na_2S tends to be oxidized at the ZnS sites and converted into long-chain NaPSs during charging and therefore, the assembled battery delivers high cycling performance (570 mAh g^{-1} at 0.2 A g^{-1} over 1000 cycles), excellent rate capability (250 mAh g^{-1} at 1.0 A g^{-1} over 2000 cycles), as well as a high energy density of 384 Wh

kg^{-1} . This study reveals the key role of the core–shell structure and multisulfophilic sites in improving the electrochemical properties of RT Na–S batteries and points out the importance of structural design.

Compared with metal oxides and sulfides, transition metal carbides have higher conductivity and excellent electrocatalytic activity for Li–S batteries. In recent years, transition metal carbides have also been widely used in RT Na–S batteries. Zhou et al. have proposed a hierarchically hollow porous carbon polyhedrons embedded with Mo_2C nanoparticles (HPC/ Mo_2C) as a host for S in RT Na–S batteries.^[170] On the one hand, the obtained hollow carbon polyhedrons with abundant micropores and mesopores (HPC) can provide channels for ions/electrons transfer, buffer the volume change of electrode during the electrochemical cycling, and avoid the failure of electrode. On the other hand, the highly conductive Mo_2C can capture NaPSs through chemisorption, thus accelerating the transformation of NaPSs. The results of potentiostatic test at 1.2 V show that the HPC/ Mo_2C has a faster response to Na_2S deposition and a higher peak current, indicating that the existence of Mo_2C can accelerate the conversion of NaPSs to Na_2S . Theoretical calculation shows that the binding energy of different S species on Mo_2C is higher than that on NG, indicating that the chemisorption of Mo_2C on S species is stronger than that of NG. In addition, the Gibbs free energy changes of S species in the discharge process for Mo_2C are smaller than those of NG, revealing that the Mo_2C can catalyze the transformation of NaPSs. As a result, the S@HPC/ Mo_2C electrode exhibits a superior rate performance of 483 mAh g^{-1} at 10 A g^{-1} and long cycle life (503 mAh^{-1} after 800 cycles at 5 A g^{-1}).

The Lewis acid–base reaction is an effective method for adsorption of NaPSs and inhibiting the shuttle effect of NaPSs. Some polar species like MXenes can accelerate the redox transformation of S species in RT Na–S batteries and this kind of materials have both the chemical adsorption capability and catalytic activity for NaPSs, thus making it possible to realize adsorption-catalysis of NaPSs for a single material. Bao et al. have introduced heteroatomic S into the MAX phase precursor and prepared functionalized MXene nanosheets (Figure 14a).^[36] The wrinkled S-doped MXene ($\text{S-Ti}_3\text{C}_2\text{T}_x$) nanosheets serve as the host materials for S in RT Na–S batteries. After vacuum freeze-drying, the $\text{S-Ti}_3\text{C}_2\text{T}_x$ has a 3D nanoarchitecture with a large specific surface area of $258.1 \text{ m}^2 \text{ g}^{-1}$ bonding well as a conductive framework. The Ti–S bond formed in the $\text{S-Ti}_3\text{C}_2\text{T}_x$ and S substitution in the Al layer indicate that the polar surface of $\text{S-Ti}_3\text{C}_2\text{T}_x$ has strong chemisorption with NaPSs. Therefore, $\text{S-Ti}_3\text{C}_2\text{T}_x$ captures soluble NaPSs on the surface by the Lewis acid–base interaction and reduces diffusion of NaPSs. The electrochemical mechanism of the $\text{S-Ti}_3\text{C}_2\text{T}_x/\text{S}$ cathode has been studied by EIS which shows that the redox reactivity of NaPSs is improved after introduction of S surface groups. As a result, the $\text{S-Ti}_3\text{C}_2\text{T}_x/\text{S}$ cathode shows a high reversible capacity of 577.1 mAh g^{-1} after 500 cycles at a current density of 2 C.

3.1.3. Heterostructures

In an ideal situation, NaPSs first adsorb onto the surface of the host and convert into the final product of $\text{Na}_2\text{S}_2/\text{Na}_2\text{S}$.

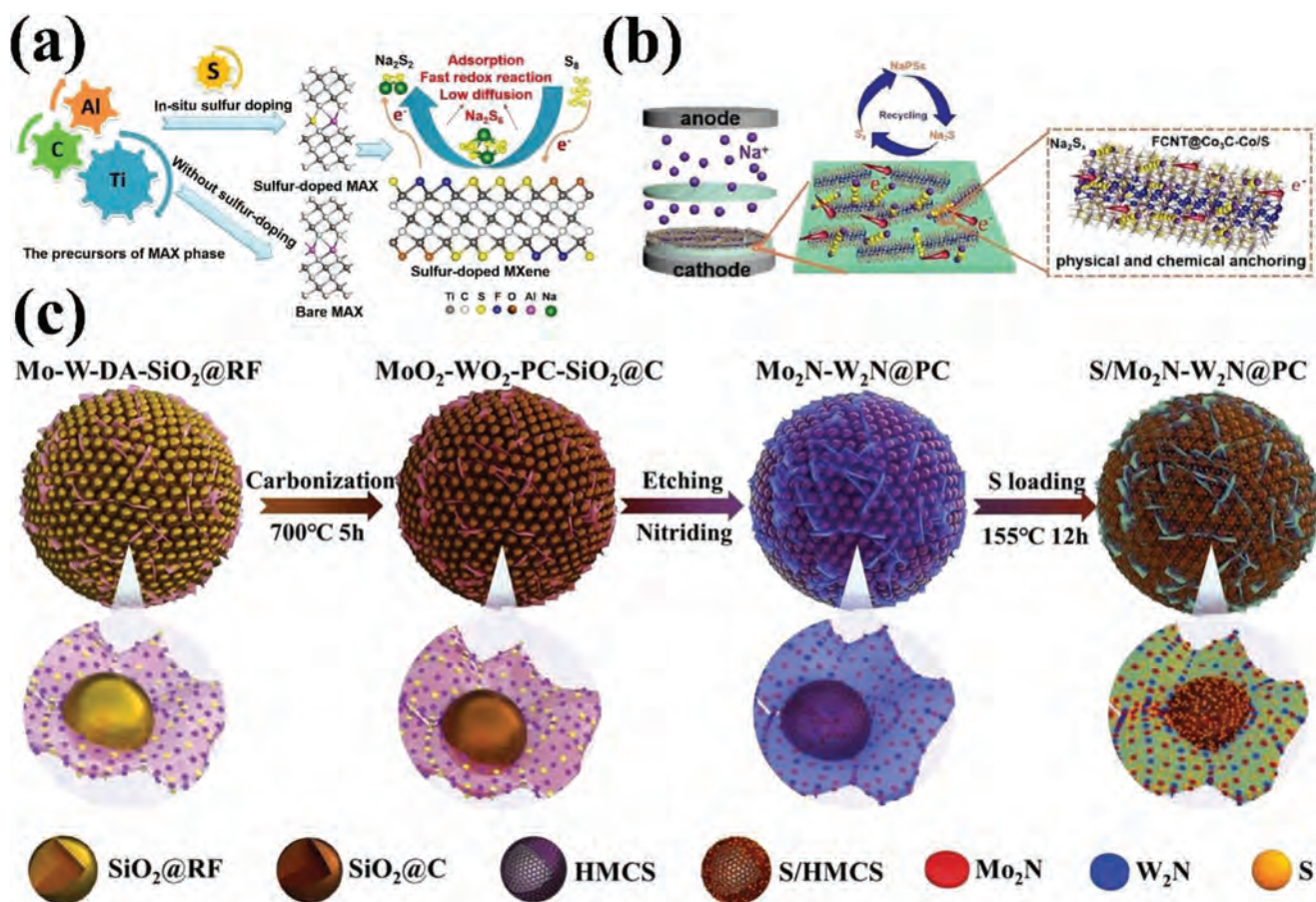


Figure 14. a) Preparation of S-doped MXene and discharge process on the S-doped MXene/S cathode. Reproduced with permission.^[36] Copyright 2019, American Chemical Society. b) Schematic showing chemical, physical anchoring and catalytic conversion of NaPSs based on FCNT@Co₃C-Co in the Na-S batteries. Reproduced with permission.^[172] Copyright 2020, American Chemical Society. c) Schematic illustration of the preparation of the spherical S/Mo₂N-W₂N@PC superstructure. Reproduced with permission.^[38] Copyright 2021, Wiley-VCH.

Although the absorbable host materials can capture NaPSs to prevent them from dissolving into the electrolyte and participating in the shuttle effect, it is noted that if the chemical bond between the NaPSs and polar materials is too strong, dead S species are formed.^[56b] On the contrary, the catalytic host materials can accelerate the redox reaction of NaPSs, but they have poor adsorption ability for NaPSs and NaPSs are far away from the electrochemical conversion centers of the catalysts leading to slow kinetics.^[171] A strategy to combine adsorption and catalytic functions to improve adsorption and transformation of NaPSs has been proposed. The heterostructure is the junction region where two different nanocrystals are coupled on the atomic level giving rise to functional combination of each component and even new properties. By combining the adsorbent and catalyst components in the heterostructure, strong absorption and rapid transformation of NaPSs can be achieved at the same time.

Qin et al. have fabricated 3D fluorinated-doped CNT arrays in the porous Co₃C-Co framework (FCNT@Co₃C-Co) for RT Na-S batteries (Figure 14b).^[172] As a consequence of the chemical interactions between the F and Co in FCNT@Co₃C-Co and Na⁺ in Na₂S, FCNT@Co₃C-Co shows strong chemisorption for NaPSs and the polar Co₃C-Co and F-modified CNTs

expedite transformation of long-chain NaPSs and short-chain NaPSs to the final products, respectively. Zhang et al. have prepared a Mo₂N-W₂N heterostructure embedded in spherical carbon (Mo₂N-W₂N@PC) as the host for S in RT Na-S batteries (Figure 14c).^[38] The spherical carbon structure not only blocks diffusion of NaPSs physically, but also facilitates chemisorption of NaPSs due to the Mo₂N-W₂N heterostructure. The Mo₂N-W₂N heterostructure accelerates the solid-liquid-solid transition from S to long-chain NaPSs and the final product (Na₂S). The S/Mo₂N-W₂N@PC cathode exhibits excellent cyclic stability in RT Na-S batteries including reversible capacities of 799 mAh g⁻¹ after 100 cycles at 0.2 A g⁻¹ and 517 mAh g⁻¹ after 400 cycles at 1 A g⁻¹. These studies indicate that the proper heterostructure can overcome NaPSs shuttling and expedite the electrochemical reaction, potentially helping the development of RT Na-S batteries.

3.1.4. Defect Engineering

Similar to Li-S batteries, defect engineering is also an effective method to improve the electrochemical performance of RT Na-S batteries. However, there are still few reports in this

area. Li et al. have reported a simple and efficient way to control the preparation of N/O-doped multichambered carbon box (MCCBs) through selective etching and stepwise carbonization of ZIF-8 nanocubes.^[173] This MCCBs is composed of porous carbon shells on the outside and connected carbon grids with hollow structure on the inside, which achieves a better spatial encapsulation and integrated conductivity through the inner interconnected carbon. In addition, the hollow structure exposes N/O atoms to the surface and acts as a catalytic center to accelerate the transformation of NaPSs. As a result, the S@MCCBs cathode shows excellent electrochemical stability (0.045% capacity decay per cycle over 800 cycles at 5 A g⁻¹) and outstanding rate performance (328 mAh g⁻¹). Eng et al. have studied the opposite effects of polar N-groups and conductivity, as well as the specific interactions of each N-group with S/NaPSs.^[174] DFT calculation shows that in microporous carbon synthesized at 800 °C (MPC-800), the polar N-groups such as pyridinic-N and pyrrolic-N preferentially exist and strongly bind to the discharged species, especially pyridinic-N and pyrrolic-N well bind to Na₂S, Na₂S₂, and Na₂S₃. This makes the oxidation/desodiation reaction require a larger overpotential. On the contrary, the nonpolar graphitic-N groups are dominated in microporous carbon synthesized at 1000 °C, which is more strongly bound to short-chain S, thus increasing the reduction/sodiation overpotentials of S in the charge state. Compared with other samples, the MPC-800/S cathode shows a better cyclic stability (retaining capacity of 980 mAh g⁻¹ after 800 cycles) even though MPC-800 has a lower conductivity.

Due to the similar natural properties of Na and Li, the electrocatalyst used for S cathode in Li-S batteries can also be introduced into RT Na-S batteries. Therefore, the ideal catalyst medium for RT Na-S batteries should have good electrical conductivity, large active surface, as many active sites as possible and appropriate affinity for NaPSs, thus improving the redox kinetics of NaPSs. In addition, advanced electrode structure design can help improve the catalytic performance of the electrocatalyst and the performance of RT Na-S batteries. Finally,

the morphology of S cathode needs to be optimized to obtain a larger tap density, which is conducive to obtain a higher S cathode volumetric capacity, so as to meet the practical application of RT Na-S batteries.

3.2. Sodium-Metal Anodes

Dendrite growth is a common phenomenon in electroplating metals in common electrolytes.^[175] Na dendrites are also produced in the electrochemical reaction on the Na anode in RT Na-S batteries. When Na dendrites penetrate the separator and contact the cathode, the batteries are short-circuited and release heat rapidly causing possible fire hazards. As mentioned for LMAs, the large volume expansion of Li, continuous growth of SEI caused by Li electroplating, rapid exhaustion of the electrolyte, large impedance of the batteries and failure, are the same problems stymieing the application of Na-metal anodes (SMAs). Compared to LMAs, SMAs react with the carbonate electrolyte in a different way and the strategies to improve the performance of LMAs cannot be directly translated to SMAs.^[176] Na dendrites have a variety of morphologies and usually appear as “needle-like” or “mossy” (Figure 15). In the case of Li, the “needle-like” or “mossy” morphology is related to the growth conditions based on defect catalysis at low currents excluding the ion diffusion limitation. However, the origin of Na dendrites is not clear and maybe similar to that of the Li metal. The fundamental differences between the Na and Li are described in the following:

- 1) The thermodynamic and kinetic processes of nucleation of Na metal are different from those of Li metal. Na can bond with inorganic, metallic, or carbon hosts but Li cannot.
- 2) The growth kinetics of Na metal is different from that of Li metal. A higher homologous temperature is observed from Na-metal batteries at RT ($T/T_m = 0.8$ vs 0.65, Na vs Li).
- 3) Li dendrites are stronger than Na dendrites, as shown in Table 3. Therefore, Na dendrites can more easily dissolve

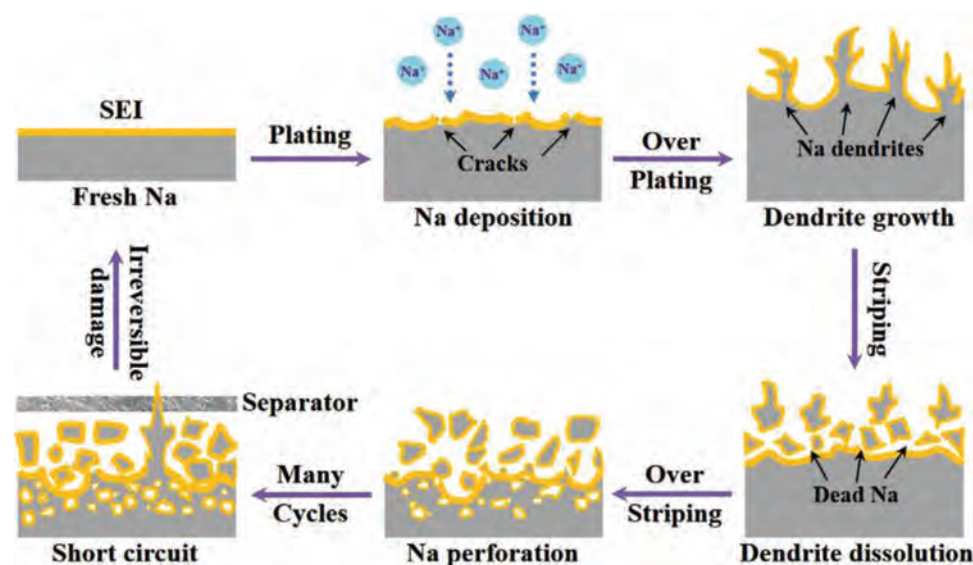


Figure 15. Schematic illustration of the formation of Na dendrites. Reproduced with permission.^[179] Copyright 2021, Wiley-VCH.

Table 3. Comparison of the physical properties of Li and Na.

	Atomic properties				Physical properties			
	Atomic radius [pm]	Covalent radius [pm]	Van der Waals radius [pm]	Ionization energy [kJ mol ⁻¹]	Melting point [K]	Boiling point [K]	Critical point [K]	Heat of vaporization [kJ mol ⁻¹]
Li	152	128±7	182	520.2	454	1603	3220	136
Na	186	166±9	227	495.8	371	1156	2573	97

	Mechanical properties				
	Shear modulus [GPa]	Bulk modulus [GPa]	Mosh hardness	Brinell hardness [MPa]	Bonding to carbon, metal underpotential deposition on carbon surface
Li	4.2	11	0.6	5	Strong, yes
Na	3.3	6.3	0.5	0.69	Weaker, no, or maybe?

in common battery electrolytes and be broken under external pressure.

- 4) The SEI composition, structure, and stability of SMAs differ from those of LMAs. This leads to a different trend in Na-based systems compared to Li-based systems. For instance, additive FEC contributes to the formation of the stable SEI film on both LMAs and SMAs, whereas SMAs induces significant voltage polarization but LMAs do not.^[176–177] Compared with LMAs, there is a higher inorganic content (Na–F to Na–O) in the SEI of LMAs in the carbonate solution (EC/DMC) with analogous salts (LiPF₆ and NaPF₆).^[178] These inorganic compositions are preferred because they are elastically stiff enough to block Na dendrites. Another difference between Na and Li is that Na dendrites grow at the base rather than the tip.^[179]

It is generally believed that formation of dendrites arises from diffusion limitations of the electrolytes during metal electrodeposition.^[180] Dendrites are directly related to Sands' time which exhibits the behavior of dendrites at high current densities during electroplating/stripping. However, this view is not suitable for the Na-based system because the rate of formation of Na dendrites is wider including moderate and even low currents.^[181] Growth of dendrites in SMAs can be explained by a sequential growth mechanism. During initial deposition, the SMA contacts the electrolyte unevenly to form an uneven SEI film due to non-uniform Na deposition. Later, the ion flux concentrates on the protuberance to generate dendrites.^[182] The geometrically non-uniform surface on the Na metal is not that important because the physical and chemical heterogeneity of the SEI layer is intrinsically heterogeneous, although it is originally completely isotropic. In this case, the concentrated ion flux is also not that important for the growth of Na dendrites because the heterogeneous SEI layer leads to uneven development of the Na metal. For instance, preferential growth of Na dendrites may be introduced by the surrounding SEI structures such as cracks, pores, nucleation sites, or simply thinned cross-sections to shorten the transfer distance. The heterogeneity of SEI accelerates nonisotropic growth of Na dendrites and growth of mossy Na dendrites is mainly attributed to the electrocatalytic effects of the SEI.^[183]

During the electrochemical stripping process, Na near the root of Na dendrites is more likely to dissolve because this location is more receptive to electrons.^[183] This phenomenon leads to the dendrites electrically exfoliated from the current collector

due to the concentrated ion flux or mechanical stress caused by the strain of the SEI layer. This part of Na is called “dead Na” and causes a sharp drop in CE and increase in the impedance, eventually giving rise to battery failure. Although the “dead Na” has no electrochemical activity, its chemical activity still exists and can react with electrolytes to form SEI on the surface. Formation of “dead Na” is accompanied by a new Na-metal surface and contact with the electrolyte further accelerates the formation of the SEI film.^[182–184]

The dendrites on the surface of SMA create a porous morphology, thus increasing polarization and overpotentials during charging and discharging.^[185] Yui et al. have proposed a formation mechanism for Na dendrites. Na nucleates on the root of the surface of the Na-metal electrode and then grows continuously to form Na dendrites.^[183] Although it is a valid viewpoint, other mechanisms of Na dendrite growth are worth noting. However, up to now, our knowledge of Na-metal systems is still limited and the fundamental information about Na dendrites is still lacking. For example, because of the different physical and chemical properties of Na and Li, it is still not clear whether the nucleation and growth model of Li dendrites is suitable for SMAs. Therefore, it is necessary to conduct more research and design advanced electrodes to improve the electrochemical characteristics of SMAs in RT Na–S batteries.

3.2.1. Conductive Hosts

Dendrite growth can be alleviated by decreasing the current density and a conductive host with a large surface area can reduce the effective current density because the surface area available for metal plating is several orders of magnitude larger than that on a planar current collector.^[115,186] The porous host not only attenuates concentration polarization that causes dendrite growth, but also provides dense nucleation sites for metal nucleation and finer grains. This strategy improves the CE in electroplating/stripping and inhibits the formation of dendrites and these hosts often overlay or even act directly as current collectors. For example, Liu et al. have designed a 3D porous Al current collector as the host for Na to provide a large surface area for nucleation during Na electrodeposition and facilitate uniform electroplating/stripping of Na (Figure 16a).^[187] The 3D porous Al current collector does not alloy with Na and the interconnected porous structure yields a large surface area for Na

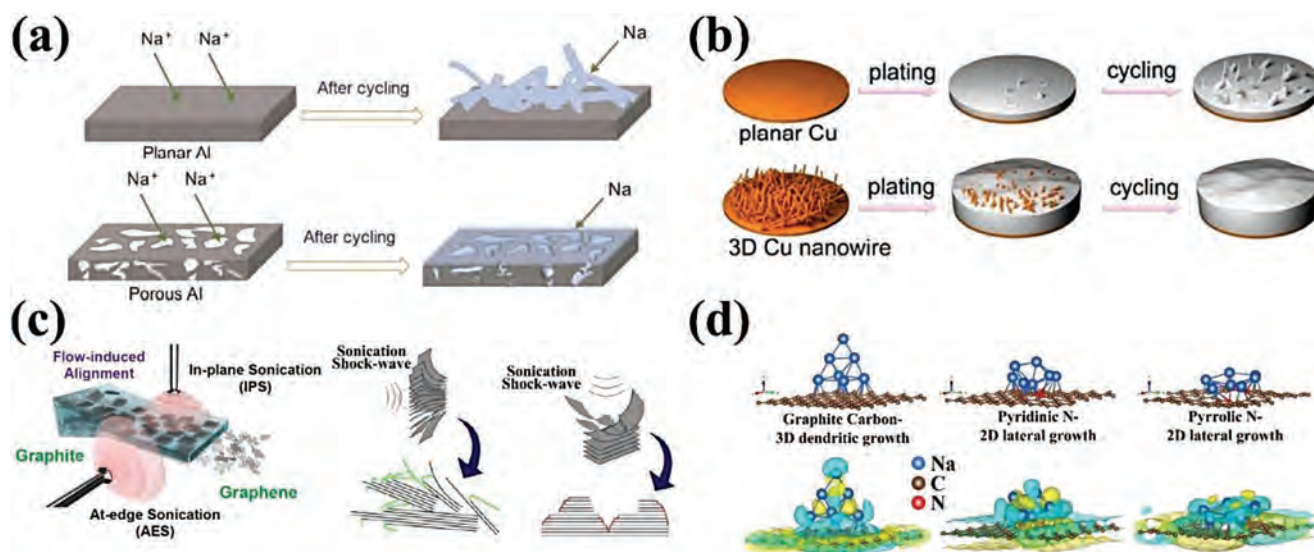


Figure 16. a) Deposition of Na on planar and porous Al current collector. Reproduced with permission.^[187] Copyright 2017, American Chemical Society. b) Schematic illustration of Na-plating models on different current collectors of planar Cu foil and 3D Cu nanowires. Reproduced with permission.^[188a] Copyright 2017, Royal Society of Chemistry. c) Exfoliation process of AES-G and IPS-G. Reproduced with permission.^[189] Copyright 2018, American Chemical Society. d) Final relaxed states (top) and charge density difference plots (bottom) after seven sequentially adsorbed Na atoms on crystalline carbon, carbon with pyridinic-N and carbon with pyrrolic-N species. Reproduced with permission.^[190b] Copyright 2021, Elsevier Ltd.

nucleation while reducing the Na⁺ flux, thus resulting in homogeneous deposition of Na. With increasing Na plating amounts from 0.25 mAh cm⁻² to 0.5 mAh cm⁻², Na first grows on the Al skeleton and gradually fills the pores in the 3D Al host. Even when the plating amount of Na is increased to 2 mAh cm⁻², no clear dendrites are observed. After stripping of Na, the square-wave texture of the 3D Al porous host returns to the original shape, indicating that plated Na is stripped reversibly. However, the surface of the planar Al current collector appears patchy and then mossy like Na with increasing Na plating amounts. The mossy structure becomes more significant after several cycles eventually loosening the connection with the host to form “dead Na”. The SMAs based on the 3D Al porous host can operate for 1000 cycles with a low and stable voltage hysteresis and high average CE of >99.9%. In addition to 3D porous Al, nonreactive metals such as Ni@Cu and porous Cu can be used as the host materials for SMAs.^[188] Lu et al. have reported a simple method to transfer the commercial Cu foil to 3D Cu nanowires by a hydrothermal route and systematically studied the Na electroplating/stripping behavior (Figure 16b). The 3D Cu nanowires with a smaller diameter (<40 nm) distribute the electric field more effectively to realize stable and uniform Na deposition. The 3D Cu nanowires have a high areal capacity of 3 mAh cm⁻² as well as stable electroplating/stripping for over 100 cycles.

Compared with the metallic current collector, carbonaceous materials have smaller densities and weights with abundant pores, and can effectively buffer the volume change of the Na metal during electroplating/stripping, thus preventing the SMAs from breaking. Liu et al. have employed a directional flow-acid sonochemistry (FAS) exfoliation technique to alter the structure and chemical state of graphene and studied the effect of defects on electrodeposition of Na metal (Figure 16c).^[189] In the FAS process, the ultrasonic waves propagate parallel or

vertical to the edge of the graphite flake. The at-edge sonicated graphene (denoted as AES-G) is produced when the ultrasonic shockwave vector is parallel to the (0002) basal plane, while the in-plane sonicated graphene (labeled as IPS-G) is synthesized by the shockwave normal to the (0002) basal plane. Compared with IPS-G, AES-G has a larger band ratio between the G and D bands of sp² carbon ($I_G/I_D = 14.3$) in the Raman spectra and a smaller surface oxygen concentration (1.3%) indicative of less defects in AES-G. The voltage of Na-metal batteries using AES-G as the host is more stable while voltage fluctuations are observed from Na-metal batteries with the IPS-G host and bare Cu current collector, indicating that the structural and chemical defects in carbon promote the formation of the SEI layer during electroplating/stripping and cause harm to Na plating and stripping.

3.2.2. Nucleation Regulation

High-purity porous carbonaceous materials have poor wettability to molten Na because of weak binding between Na and solid carbon. The chemical properties of carbon surface have an important influence on the wettability of molten Na and affect initial nucleation, nucleation density, and subsequent growth kinetics of Na during electrodeposition on the carbon surface.^[179,190] To improve the wettability of Na, it is necessary to introduce heteroatomic functional groups into the carbonaceous hosts. These hosts, known as the “sodiophilic matrix,” have modified surface chemistry and low wettability angles. Mubarak et al. have prepared hollow mesoporous carbon nanofibers (HpCNFs) by a coaxial electrospinning technique and the rich defects and N functional groups form a strong attraction with Na (Figure 16d).^[190b] The sodiophilic surface allows molten Na to permeate quickly and uniformly. Even at

a large current density of 3 mA cm^{-2} and plating capacity of 6 mAh cm^{-2} , only a low voltage hysteresis of 60 mV occurs during plating and the average CE remains at 99.7% after 1400 cycles. The low overpotential of the HpCNF electrode reflects that the energy barrier of Na electroplating/stripping on the surface of the HpCNF host is low. DFT calculation demonstrates that N functionalized carbon, including pyridinic-N and pyrrolic-N, attracts electrons from diffusing Na atoms to the carbon host and accelerates nucleation of Na on the carbon surface. In the continuous Na plating process, adjacent Na nuclei merge leading to uniform Na deposition on the N-functionalized surface of the carbonaceous hosts.

In addition to graft heteroatomic functional groups into the carbonaceous hosts, introducing sodiophilic metals into the carbonaceous host is an effective strategy to improve the electrochemical properties of SMAs. On the one hand, sodiophilic metal particles act as nucleation seeds to promote the density, uniform nucleation, and rapid deposition of Na.^[179,191] On the other hand, the carbonaceous matrix provides the SMAs with excellent mechanical stability, electrical conductivity, and large specific surface area. Lu et al. have constructed a sodiophilic and conductive host with the hierarchical vertical graphene (VG) cultivator and Co/N-doped carbon decorator (Co-VG/CC).^[191d] The Na metal penetrates the host (Na@Co-VG/CC) by melt-diffusion to impede unwanted SEI and tedious prestoring inherent to conventional electrodeposition methods. Electrochemical studies show that introduction of Co into the carbon

framework reduces the overpotential and accelerates electro-deposition of Na (Figure 17a). Even when the current density is increased to 5.0 mA cm^{-2} , the symmetrical batteries with the Na@Co-VG/CC electrode still operates steadily for 280 h at a high capacity of 5.0 mAh cm^{-2} . The low charge transfer resistance of the Na@Co-VG/CC electrode regulates the reaction kinetics of Na deposition/stripping. The finite element method is adopted to simulate the Na^+ concentration and local current density at the interface between the electrode and electrolyte and to explore the mechanism of uniform Na deposition. The result reveals that the uniform Na^+ concentration distribution on the surface of Na@Co-VG/CC and uniform local electron flux inhibit dendrite growth. DFT calculation demonstrates that the Co cluster anchored on the N-doped graphene acts as nucleation sites offering advanced absorption of Na to restrain dendrite formation.

Typically, Na is deposited on the top surface of the SMAs and it is followed by a “top-growth” method. The gradient interfacial layer is a reliable method to prevent uncontrolled growth of Na dendrites. Sun et al. have made a protective layer consisting of a carbon nanotube (CNT) film with a sodiophobic–sodiophilic gradient in the direction of the thickness (Figure 17b).^[191c] This structure is prepared by embedding sodiophilic Ag nanoparticles into the wall of sodiophobic CNTs to form an Ag-deficient layer on one side of the CNT film and an Ag-rich layer on the opposite side (grad-Ag@CNT). The protective layer is placed between the separator and metal current collector, whereas

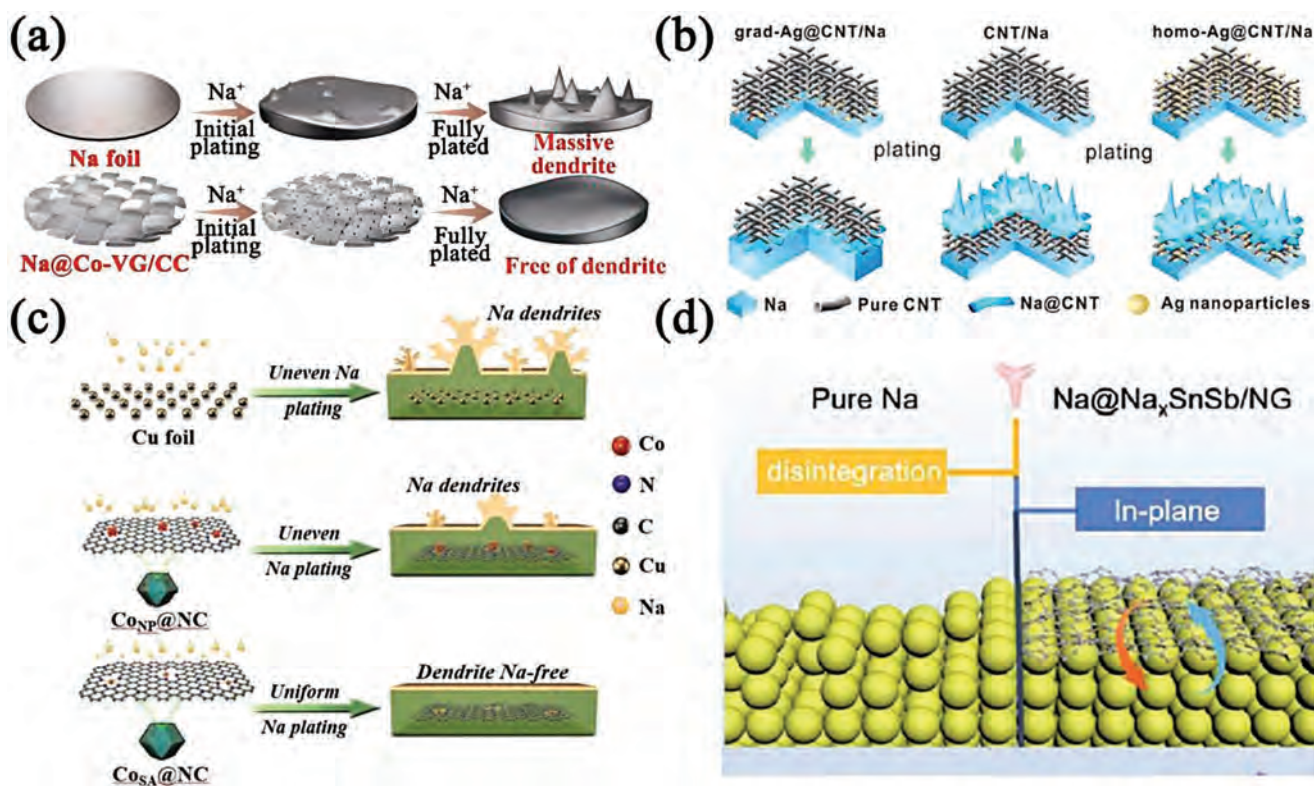


Figure 17. a) Schematic diagram of Na plating on the bare Na foil and Na@Co-VG/CC and mechanism. Reproduced with permission.^[191d] Copyright 2021, Wiley-VCH. b) Deposition behavior of Na in different interlayer/Na anodes. Reproduced with permission.^[191c] Copyright 2021, American Chemical Society. c) Deposition of Na in different interlayer/Na anodes. Reproduced with permission.^[193] Copyright 2021, Wiley-VCH. d) Schematic illustration of the protection mechanism of NG. Reproduced with permission.^[195] Copyright 2021, Royal Society of Chemistry.

the Ag-rich layer is placed far away from the separator. The Ag nanoparticles are more inclined to adsorbing Na to enable uniform deposition of Na and produce a low overpotential during nucleation. Na plated on the Ag-rich layer previously contributes to Na nucleation and growth far away from the separator, while bare Na dendrites are formed on the Ag-deficient layer. As a result, the half-cell consisting of grad-Ag@CNT films can operate for more than 100 cycles (or 800 h) with a CE value higher than 99.5%. This work reveals the potential of advanced metal catalysts in reducing the nucleation overpotential of Na and producing stable SMAs.

The single-atom system can maximize the utilization rate of atoms and has been used as catalysts for energy storage, for example, Li-metal batteries and cathodes in RT Na–S batteries. However, the application to SMAs has seldom been reported.^[192] Li et al. have prepared a single Co atom uniformly decorated porous N-doped carbon matrix (Co_{SA}@NC) by carbonizing the Co-doped zinc-based metal–organic framework (Co-doped Zn-MOF) as a host for SMAs.^[193] The isolated Co single atoms are uniformly dispersed on the carbon polyhedron to provide a large number of stable sodiophilic sites for adsorption and nucleation of Na⁺. The sharp voltage dip followed by a flat voltage plateau observed from the Na plating curve of general materials is known as the nucleation overpotential.^[194] The nucleation overpotential of Na deposited on Co_{SA}@NC is quite small indicating that the Co single atoms accelerate uniform nucleation and deposition of Na. Even when the current density is increased to 5.0 mA cm⁻², Co_{SA}@NC still shows a small Na nucleation overpotential and long cycling lifetime of more than 1500 h at the high capacity limitation of 20.0 mAh cm⁻². The sodiophilic Co single atoms act as seeds to induce rapid nucleation and uniform deposition of Na during electroplating/stripping. The surface of the Co_{SA}@NC electrode after Na plating has a smooth morphology without dendrites and dead Na, further confirming uniform deposition of Na in electroplating/stripping (Figure 17c). Furthermore, the RT Na–S battery consisting of the Na-Co_{SA}@NC anode and S-Co_{SA}@NC cathode shows a high specific capacity of 765.2 mAh g⁻¹ and capacity retention of 88.5% after 210 cycles, revealing that the single-atom catalyst has great potential in high-performance RT Na–S batteries.

Although a great deal of research has been done on uniform nucleation and deposition of Na, the design of the proper hosts to protect freshly plated Na from parasitic side reactions is still lacking. Wang et al. have prepared a 3D sponge in which SnSb nanoparticles are uniformly encapsulated in the N-doped graphene framework (SnSb/NG) as a multifunctional host for stable SMAs.^[195] As shown in Figure 17d, SnSb/NG not only promotes smooth nucleation and growth of Na, but also protects newly plated Na from parasitic reactions. During Na deposition, Na₁₅Sn₄ and Na₃Sb formed initially produce almost zero overpotential for Na nucleation and regulate subsequent dendrite-free Na growth underneath the NG framework. The SnSb/NG-based SMAs do not form inactive and mossy Na structures in Na electroplating/stripping and the battery delivers stable cycling performance with the CE up to 95% for more than 500 cycles.

As discussed in Section 2.2, metal oxides that are easy to prepare can regulate the nucleation and dendrite-free deposition of Li. Similarly, metal oxides can act as alkali-metal ion homogenizers to distribute Na⁺ evenly and promote uniform nucleation.

Li et al. have reported that the change in the Gibbs free energy (ΔG) for the reaction between metal oxides (Co₃O₄, SnO₂, CuO) and Na is negative according to DFT calculation, constituting the key for Na-metal infusion.^[196] A hierarchical Co₃O₄ nanofiber-carbon sheet (CS) framework is prepared as a stable host for SMAs to take advantage of the excellent Li/Na adsorption properties (Figure 18a). The Co₃O₄ nanofibers are vertically oriented on the surface of the commercial conductive carbon sheet by a hydrothermal method and the Na/Co-CS is prepared by molten Na perfusion. The SMA has many advantages. The Na metal reacts with Co₃O₄ rapidly to form Na₂O/Co as ΔG of the reaction is negative and so the surface energy of the matrix is reduced. After the reaction, the Co₃O₄ nanofibers still adhere to the carbon fiber matrix to physically confine the plated Na and ensure sufficient contact with the electrolyte for charge transfer of Na/Na⁺ in the redox reactions leading to uniform Na nucleation. Generally, the deposition sites at smaller particles are more evenly dispersed to benefit Na plating.

Quantum dots are promising for Na⁺ plating because of the nanoscale characteristics, high affinity with Na⁺, and easy preparation. Xu et al. have designed a host in which SnO₂ quantum dots are uniformly distributed to cover a 3D carbon cloth scaffold (SnO₂-CC).^[197] This structure has high affinity with molten Na, enables the spontaneous reaction between SnO₂, and yields a low nucleation barrier for Na electroplating/stripping (Figure 18b). Different from the uncontrolled formation of Na dendrites on the plate electrode, SnO₂ quantum dots accelerate dense and uniform deposition of Na on the surface of the SnO₂-CC due to the reduced overpotential of Na nucleation stemming from the alloying reaction between SnO₂ and Na. The Na/SnO₂-CC electrode operates stably for more than 400 cycles with a low overpotential of ≈ 100 mV at a large current density of 20 mA cm⁻². This electrode with quantum dots provides a promising strategy for stable and safe SMAs.

2D materials have good effects in regulating Li/Na deposition and preventing dendrite formation. 2D materials are also adopted in 3D skeletons with adjustable pores that buffer the volume change during Na electroplating/stripping. MXene is a class of 2D materials with a layered structure, large specific surface area, high mechanical strength, as well as high electron/ion conductivity. These attributes render MXene hot materials in the field of energy storage. Fang et al. have prepared a 3D porous MXene-rGO matrix with a “build-function” as the stable host for SMAs (Figure 18c).^[198] DFT calculation reveals that the functional groups containing F and O have high adsorption energy, while the adsorption capacity of pure Ti₃C₂T_x and rGO is poor. The cross-section SEM images of the Ti₃C₂T_x-rGO host containing Na show that the interlayer space of Ti₃C₂T_x-rGO is almost filled with molten Na and no lamellar structure can be observed. Therefore, the Na dendrites generated during cyclic electroplating/stripping are separated and sealed in the separate interlayer cells. In addition, the MXene with high mechanical properties acts as an artificial SEI and inhibits the growth of dendrites. The surface on the Na–Ti₃C₂T_x-rGO electrode is smooth with few Na dendrites, but that on the bare Na electrode shows a large number of Na dendrites. Na atoms induced by Ti₃C₂T_x tend to be deposited in the interlayer pores and the interlayer pores wrap the dendrites to provide physical protection for the dendrites. This work reveals the feasibility of the

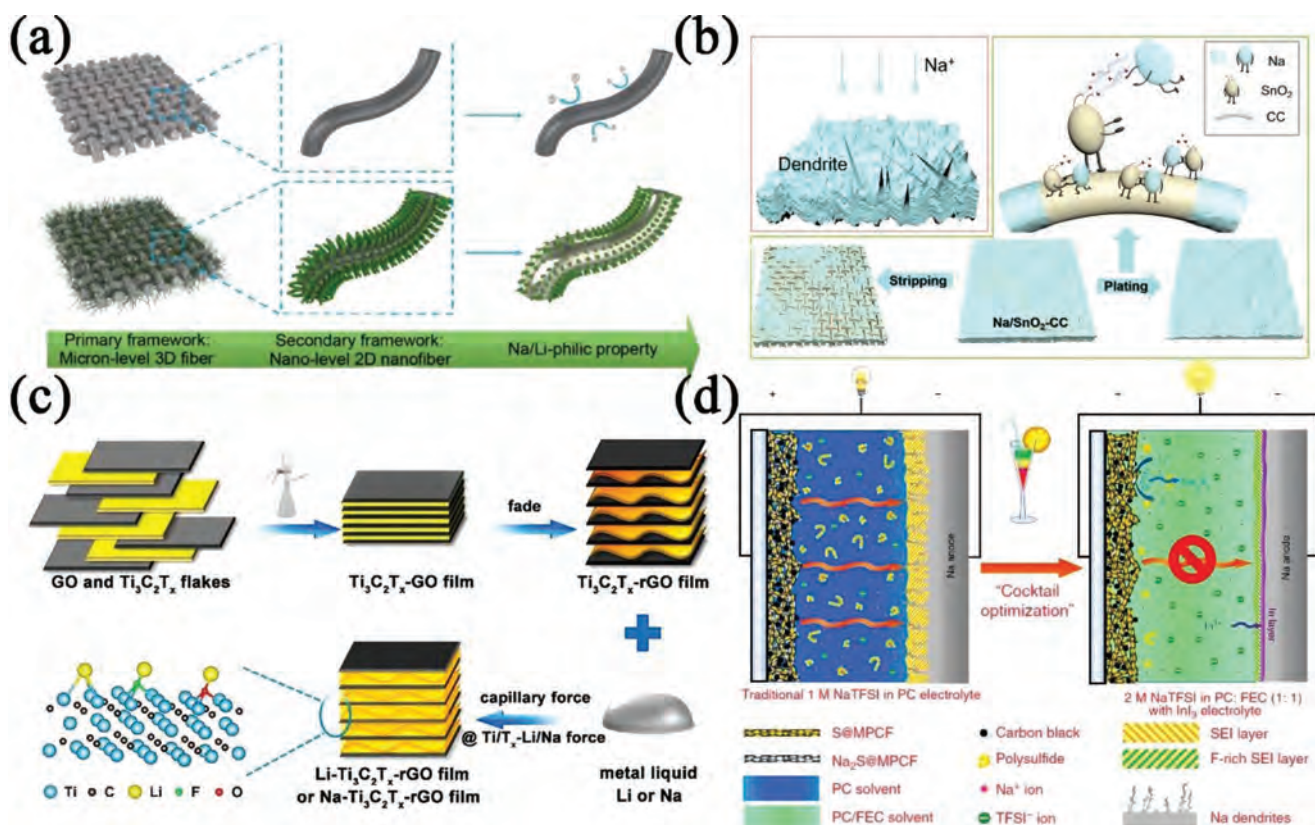


Figure 18. a) Schematic illustration of the multilevel structure of the Co_3O_4 -CS skeleton and related behavior when contacting molten alkali metal. Reproduced with permission.^[196] Copyright 2019, Wiley-VCH. b) Schematic illustration of Na deposition on the plate electrode and Na/SnO_2 -CC scaffold. Reproduced with permission.^[197] Copyright 2020, American Chemical Society. c) Preparation of the $\text{Li}/\text{Na}-\text{Ti}_3\text{C}_2\text{T}_x$ -rGO electrode. Reproduced with permission.^[198] Copyright 2019, American Chemical Society. d) Schematic illustration of RT Na-S batteries containing conventional 1 M NaTFSI in PC electrolyte and 2 M NaTFSI in PC/FEC with 10×10^{-3} M InI_3 additive electrolyte. Reproduced under the terms of the CC-BY Creative Commons Attribution 4.0 International license (<https://creativecommons.org/licenses/by/4.0>).^[214] Copyright 2018, The Authors, published by Springer Nature.

design of multifunction hosts (e.g., MXene and graphene) for advanced SMAs.

According to the discussion above, the main problems for SMAs are the instability of the SEI layer, the drastic change in electrode volume, the continuous consumption of active Na, and the continuous formation of “dead Na.” By introducing a conductive host, the volume change during the electrochemical cycling is buffered and the dendrite growth of Na is inhibited due to the scattering of deposited Na^+ flux and local charge density. By regulating the nucleation and deposition behaviors, the interfacial barrier can be lowered and Na^+ can be deposited uniform on the SMAs. Although stable SMAs can be achieved by these two strategies, the confused mechanism of Na dendrite growth restrict the further development of the SMAs. Therefore, further research in this area is needed.

3.3. Electrolytes

Electrolyte is the medium to ensure the ionic transport between the S cathode and Na anode, which plays an important role in the electrochemical performance of RT Na-S batteries.^[1,199] The wide voltage windows, excellent ionic conductivity and electrochemical stability of ether and carbonate ester electrolytes

contribute to the stable operation of RT Na-S batteries.^[200] In recent years, researchers have paid great attention to the development of electrolytes for RT Na-S batteries.

3.3.1. Solvents

Ether-based solvents, such as DOL, DME and TEGDME, are traditional solvents widely used in Li-S and RT Na-S batteries.^[201] Similar to Li-S batteries, ether-based solvents highly dissolve NaPSS, leading to the rapid transformation of NaPSS in the liquid phase. However, this phenomenon results in the shuttle of NaPSS between cathode and anode during the discharge/charge process, which cause the loss of active materials and corrosion of SMAs, leading to degradation of electrochemical performance. After extensive research, this situation has been eased in recent years. Lee et al. have exploited a hollow C/S cathode and employed a $\text{NaCF}_3\text{SO}_3/\text{TEGDME}$ electrolyte for RT Na-S batteries.^[202] The TEGDME-based solution interacts with the highly delocalized CF_3SO_3^- soft, leading to the rapid migration of Na^+ . This effectively reduces the concentration polarization and increases electrode kinetics during the battery cycling. Therefore, the RT Na-S batteries with $\text{NaCF}_3\text{SO}_3/\text{TEGDME}$ electrolyte show a high reversible capacity of 1000 mAh g^{-1} .

Carbonate-based electrolytes are commonly used electrolytes in NIBs containing carbonate-based solvents, such as cyclic carbonates (e.g., PC, EC, and FEC) and linear carbonates (e.g., DEC, and ethyl methyl carbonate (EMC)), which have also been widely introduced into RT Na–S batteries.^[200,203] The carbonate-based solvents determine the compositions of the SEI at the anode and CEI at the cathode.^[204] However, a single carbonate-based solvent is not suitable for RT Na–S batteries. Pure PC, as the only solvent, decomposes continuously during the battery cycling, resulting in the instability of SEI layer and CEI layer and the failure of RT Na–S batteries.^[205] Pure EC solvent has a high melting point (36.1 °C) and is not suitable for RT Na–S batteries.^[200] Binary and ternary solvents balancing the different chemical properties of each group have been studied in order to obtain high-performance solvents for RT Na–S batteries. For example, binary carbonate-based solvents composed of EC and PC are widely used in RT Na–S batteries due to their ability to promote the formation of SEI and CEI layers simultaneously. The EC can alleviate the continuous decomposition of PC and prevent the consumption of active materials.^[206] Li et al. have applied a binary PC/EC solvent to RT Li–S batteries assembled with S/mesoporous nitrogen-doped carbon nanospheres (S/PNC-Ns) cathode and modified separator.^[207] The prepared RT Na–S batteries can deliver a high reversible capacity of 639 mAh g⁻¹ at 0.1 C after 400 cycles. In addition, FEC is widely applied as a solvent or additive to inhibit the reduction decomposition of PC, and can facilitate the formation of strength and stable SEI films at the SMAs, limiting the growth of Na-metal dendrites.^[208] Guo et al. have used FEC as an additive in PC/EC solvent to test the constructed S cathode.^[209] The assembled RT Na–S batteries can deliver a high reversible capacity of 997 mAh g⁻¹ after 400 cycles at 0.1 C. It should be noted that RT Na–S batteries with carbonate-based solvents undergo a complex activation process, including the reaction between carbonate and NaPSs.^[2c,210] These reactions promote the formation of SEI on the surface of SMA and CEI on the surface of S cathode, leading to ultrahigh initial discharge capacity even exceeding theoretical capacity of S.

Based on the above discussion, although carbonate-based and ether-based solvents have their own natural disadvantages, they have been shown to achieve the cyclic stability of RT Na–S batteries when combined with suitable cathodes.

3.3.2. Additives

Due to the natural shortcomings of solvents, additives are considered to be an effective strategy to improve the performance of RT Na–S batteries. NaNO₃ is a commonly used additive in RT Na–S batteries, which can promote the formation of dense SEI layer in the Na anode, thus avoiding the corrosion of SMA. Ghosh et al. have prepared S-rich copolymer (CS90)-rGO cathode and assembled RT Na–S batteries with NaNO₃ additive.^[211] The prepared RT Na–S batteries can deliver a high reversible capacity of 650 mAh g⁻¹ at 0.2 A g⁻¹, and show a good electrochemical cyclic stability of 498 mA h g⁻¹ after 50 cycles. It is noteworthy that the NaNO₃ additive can promote the formation of stable SEI film on the surface of SMA and protect the Na anode from NaPSs corrosion. Therefore, only a small

amount of S can be detected on the surface of SMA after repeated electrochemical cycling, indicating the shuttle effect of NaPSs is suppressed.

In addition to NaNO₃, P₂S₅ is another kind of additive for RT Na–S batteries. Kohl et al. have tailored the electrolyte components by adding Na₂S/P₂S₅ into TEGDME.^[212] The addition of P₂S₅ can form a stable SEI film on the electrode surface, and the battery shows good electrochemical cycling performance. In addition, the CV profile shows that the discharge voltage is increased while the voltage is decreased during the charging process, indicating that the presence of P₂S₅ can accelerate the conversion kinetic of NaPSs. Combined with a presodiated hard carbon anode, the assembled battery can deliver a high discharge capacity of 980 mAh g⁻¹ over 1000 cycles. Similarly, Ren et al. have also used NaI-P₂S₅ as an electrolyte additive for RT Na–S batteries.^[213] The results show that the formation of Na₂S₂-P₂S₅ complex promotes the precipitation kinetics of Na₂S₂, and the chemical mediation of I⁻/I₃⁻ promotes the dissolution of Na₂S₂. Therefore, a high capacity retention of 92.9% can be obtained after 50 cycles at 0.2 C.

Recently, a “cocktail optimized” electrolyte containing a large concentration of Na–Salt (2 M), InI₃ as an additive, and a co-solvent made of PC and FEC (1:1 by volume), has been developed for advanced RT Na–S batteries (Figure 18d).^[214] DFT calculation reveals that the NaPSs tends to adhere to the surface of the carbon network rather than dissolve in the FEC-based electrolytes. The Na₂S also tends to agglomerate on the surface of the carbon network in the electrode rather than transfer to NaPSs. Galvanostatic cycling of the Na/Na symmetrical cells at a current density of 0.1 mA cm⁻² shows uniform Na deposition with a stable electrolyte/Na-metal interface is more easily formed due to passivation by the In layer formed by the InI₃ additive. I⁻ is oxidized to I₃⁻ at 2.9 V versus Na/Na⁺, which increases the kinetic conversion of Na₂S and reduces the irreversible capacity. As a result, the RT Na–S batteries composed of the “cocktail optimized” electrolyte shows a high capacity of 1170 mAh g⁻¹ at 0.1 C and excellent cyclic stability (648 mAh g⁻¹ and 581 mAh g⁻¹ at 0.5 C and 1 C after about 500 cycles, respectively). This work shows that the design of an advanced electrolyte system plays an important role in improving the electrochemical reaction kinetics and electrochemical stability of the cathode and anode in high-performance RT Na–S cells and the strategy can be extended to other types of M–S batteries.

As mentioned above, in order to obtain high-performance RT Na–S batteries, the electrolyte must contain limited NaPSs solution and can facilitate the formation of stable CEI and SEI films on the cathode and anode surfaces. Due to the natural properties of different solvents and Na–Salts, developing binary and ternary solvents/Na–Salts systems can make up for their shortcomings and realize the optimization of performance. Some additives can promote the conversion kinetic of S species, and the introduction of these compounds can finally improve the performance of RT Na–S batteries.

3.4. Functional Separators

The separator is an important component of RT Na–S batteries, allowing Na⁺ to be transferred between the cathode and anode

during electrochemical cycling.^[215] Glass fiber (GF) is a commonly used separator in RT Na–S batteries.^[8b] However, some soluble NaPSs can also pass through the separator, resulting in the severe loss of active material and the failure of battery.^[216] To address these obstacles, functional separators that can absorb NaPSs have been studied because they can inhibit the shuttle of soluble NaPSs to the anode regions, thus greatly improving the electrochemical performance of RT Na–S batteries.

In recent years, the functional separator with electrocatalytic effect has also been widely studied. Dong et al.^[217] have constructed a functional separator prepared by coating N-dope hollow carbon spheres decorated with few-layer 2H-MoSe₂ nanoflakes and graphene oxide (2H-MoSe₂/N-HCS/GO) on GF separator and used it for RT Na–S batteries. To demonstrate the performance improvement of RT Na–S batteries with the functional separator, coin cells using 2H-MoSe₂/N-HCS/GO modified GF as separator are assembled and tested. The assembled cell exhibits high capacities of 760, 711, 659, 600, and 530 mAh g⁻¹ at the current densities of 0.1, 0.2, 0.5, 1.0, and 2.0 C, respectively, which is higher than the cell without 2H-MoSe₂/N-HCS/GO. The diffusion coefficient of Na⁺ (D_{Na^+}) at different scanning rates are measured according to the CV curves. The results show that 2H-MoSe₂/N-HCS/GO modified GF has a higher D_{Na^+} value, indicating that 2H-MoSe₂ can improve the reaction kinetics of NaPSs transformation. Moreover, the adsorption test combining with visual discrimination, ultraviolet–visible (UV–vis) absorption spectroscopy and XPS show that the 2H-MoSe₂/N-HCS can effectively inhibit the shuttle effect of NaPSs. The DFT calculation results reveal that the few-layer 2H-MoSe₂ can not only strongly interact with NaPSs, but also dynamically enhance the redox reaction of the NaPSs, which are in good agreement with the experimental results. In addition, it is worth noting that the low Na⁺ diffusion barrier on the surface of few-layer 2H-MoSe₂ allows the rapid ion migration, which improves the reaction kinetics of NaPSs transformation.

Similarly, Wang et al. have designed a double-sided coating route to construct sandwich-structured MXene@C/PP/MXene@C membrane, which serves as a dual-functional separator to improve the electrochemical properties of cathode and anode.^[218] The electrolyte static contact angle (SCA) on the MXene@C/PP/MXene@C separator is low, indicating that MXene@C/PP/MXene@C separator has good wettability, which is conducive to the infiltration of electrolyte into the pore channels of separator. The closely stacked MXene@C nanosheets also form a physical barrier to prevent the transfer of NaPSs. The electrochemical tests show that the voltage hysteresis of symmetrical cell with MXene@C/PP/MXene@C separator is lower than that of symmetrical cell with glass fiber, indicating

that the conductivity of MXene@C coating layer makes it act as upper current collectors for both cathode and anode, which helps to regulate the Na deposition behavior and improve the stability of SMA. In addition, the MXene@C coating layer close to the cathode increases the conversion kinetic of NaPSs, improving the utilization of S and the stability of the S cathode. To study the applicability of the MXene, coin-type cells are assembled with C/S composite as cathode, Na metal as anode and NaClO₄/EC/DEC/FEC as electrolyte. Electrochemical results show that the capacities of the assembled battery with MXene@C/PP/MXene@C separator are 1159 mAh g⁻¹ and 759 mAh g⁻¹ at the current density of 0.2 C and 2 C, respectively.

4. Other M–S Energy-Storage Systems

In addition to the common Li–S and RT Na–S batteries, other M–S energy-storage systems such as K–S, Ca–S, Mg–S, and Al–S batteries have also attracted attention due to their natural abundance. These metal anodes have redox potentials that are sufficiently low or even close to that of Li and have high specific gravimetric/volumetric specific capacities. Hence, M–S batteries can meet the commercial requirements of high energy densities and low cost. However, the different nature of these M–S batteries makes development challenging (Table 4). For example, in multivalent M–S batteries, the major challenge is that common organic liquid electrolytes are not suitable for multivalence metal ions. To date, a series of electrolytes have been proposed to transport metal ions in reversible electroplating/stripping of the metal.^[1] The shuttle effect may be a common problem in these energy-storage systems but can be solved to some extent by existing S cathode design for Li–S and RT Na–S batteries. In this section, the electrocatalytic effects and challenges of M–S energy-storage systems are discussed.

4.1. K–S Batteries

K has a similar working potential ($E_{\text{K/K}^+} = -2.93$ V) as Li ($E_{\text{Li/Li}^+} = -3.04$ V) and Na ($E_{\text{Na/Na}^+} = -2.71$ V) and the operating potential of K–S batteries is close to those of Li–S and RT Na–S batteries. The difference between K–S batteries and Li–S or Na–S batteries is that the size of the K⁺ (1.38 Å) is larger than that of the Li⁺ (0.76 Å) or Na⁺ (1.02 Å), making it difficult to form K₂S after the battery is completely discharged due to the slow kinetics. The final product of the K–S batteries after full discharge is KS_{0.67–0.85}.^[219] K–S batteries are promising in

Table 4. Characteristics of metal anodes.

	Electron structure	Relative atomic weight	Valence	Density [mAh cm ⁻³]	Capacity [mAh g ⁻¹]	Capacity [mAh cm ⁻²]	Potential vs SHE [V]
Li	2s ¹	6.94	+1	0.534	3860	2062	-3.04
Na	3s ¹	22.99	+1	0.968	1165	1128	-2.71
K	4s ¹	39.1	+1	0.862	685	591	-2.93
Mg	3s ²	24.31	+2	1.738	2205	3832	-2.37
Al	3s ² 3p ¹	26.98	+3	2.699	2980	8046	-1.66

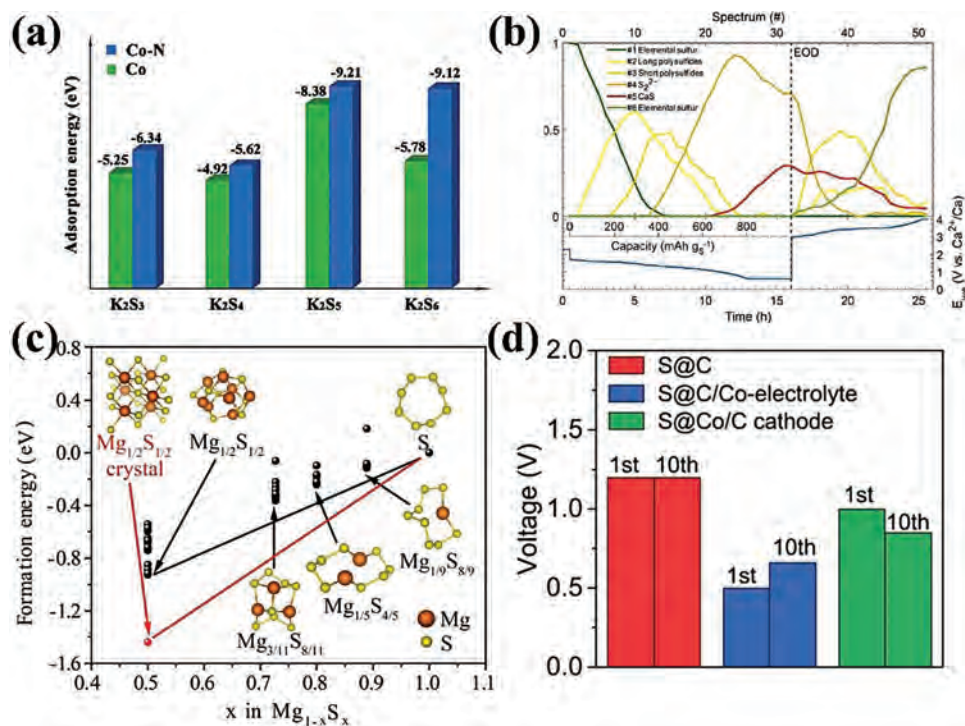


Figure 19. a) Adsorption energies for K₂S₃, K₂S₄, K₂S₅, and K₂S₆ on Co- and N-doped Co nanoparticles. Reproduced with permission.^[44] Copyright 2020, American Chemical Society. b) Operando S K-edge XANES spectra measured during a full discharge/charge cycle of a Ca–S battery. Reproduced with permission.^[10b] Copyright 2020, American Chemical Society. c) Calculated structure of MgPSs and corresponding formation energies. Reproduced with permission.^[229] Copyright 2019, American Chemical Society. d) Voltage hysteresis of the Al–S batteries. Reproduced with permission.^[10f] Copyright 2020, Wiley-VCH.

commercial application because K has similar chemical properties to Li/Na. Therefore, combining S with advanced carbon materials is also a common way to solve the shuttle effect of the intermediate potassium polysulfides (KPSs) and improve the conductivity of the electrodes.^[9d–f]

Catalysts have been incorporated into the design of S cathodes in K–S batteries. Ge et al. have prepared N-doped Co nanoclusters embedded in porous N-doped carbon (N–Co_s–C) from ZIF-67 by low-temperature pyrolysis as a host for the S cathode in K–S batteries (Figure 19a).^[44] N introduced into the crystalline Co nanoparticles during pyrolysis process forms an interstitial Co–N solid solution without changing the face-centered cubic (fcc) crystal structure. After sulfurization, S occupies most of the pores. The Tafel plot and exchange current densities of the S–N–Co_s–C cathode show that the N-doped Co clusters reduce the energy barrier of the electrochemical reactions and accelerate conversion from long-chain KPSs to short-chain KPSs. EIS reveals that the S–N–Co_s–C cathode has a low Warburg factor reflecting a large diffusion coefficient and DFT calculation shows that the N-doped Co clusters provide strong chemical interactions with KPSs to promote the conversion kinetics. The S–N–Co_s–C cathode inhibits the shuttle effect of KPSs and shows a high initial discharge/charge capacity of 879.4/657.1 mAh g⁻¹ besides a rate performance of 415.2 mAh g⁻¹ at a current density of 400 mAh g⁻¹.

The final discharge product of K–S batteries is different from that of the Li–S or RT Na–S batteries.^[44–45,219c] Ex situ XRD and XPS characterization of K–S batteries indicate that the final

products after discharge is K₂S₃ instead of K₂S. According to Lange's Handbook of Chemistry, $\Delta_r G_m^\circ$ is calculated by the following formulas

$$\Delta_r G_m^\circ (298 \text{ K}) = \Delta_r H_m^\circ (298 \text{ K}) - T \Delta_r S_m^\circ (298 \text{ K}) \quad (2)$$

$$\Delta_r H_m^\circ (298 \text{ K}) = \sum_B \nu_B \Delta_f H_m^\circ (B, 298 \text{ K}) \quad (3)$$

$$\Delta_r S_m^\circ (298 \text{ K}) = \sum_B \nu_B \Delta_f S_m^\circ (B, 298 \text{ K}) \quad (4)$$

As shown in Figure 19a and Table 5, reactions (4) and (5) have lower $\Delta_r G_m^\circ$ than reactions (1)–(3), meaning that K₂S or K₂S₂ is difficult to form because of the larger energy barrier. In this case, S is more likely to be converted to K₂S₃ during discharging and then reversibly converted to S during charging. The specific capacity of K–S batteries is lower than that of Li–S and RT Na–S batteries. In future studies, advanced catalysts should be developed to lower the energy barrier and promote the formation of the final product K₂S to improve the specific capacity/specific energy density of K–S batteries.

K-metal anodes (KMAs) have a higher theoretical specific capacity (687 mAh g⁻¹) compared with other anode materials of LIBs, which has attracted a great attention. However, the electrochemical behavior and performance of K-metal anodes (KMAs) have remained unexplored areas for many years, with challenges equal to or greater than those of LMAs and SMAs. Fortunately, considerable research experience on Li-metal

Table 5. The calculated $\Delta_r G_m^\ominus$ for following reactions.

	Reaction equation	$\Delta_r G_m^\ominus$ [kJ mol ⁻¹]
1	2K + 5S → K ₂ S ₅	-115.90
2	2K + 4S → K ₂ S ₄	-115.31
3	2K + 3S → K ₂ S ₃	-112.10
4	2K + 2S → K ₂ S ₂	-79.22
5	2K + S → K ₂ S	-38.02

anodes can provide guidance for the research of KMAs and avoid unnecessary detours. Designing a conductive host for K metal is an effective method to stabilize the K-metal anode. First, the conductive host can encapsulate the active K, separating its contact with electrolyte and reducing side reactions. Second, the conductive host can provide space to buffer the volume change during electrochemical cycling, thus improving the interfacial stability. Third, the conductive host with high surface area can provide fast transfer channels for electrons and ions, and prevent the growth of K dendrites by reducing the local current densities. Liu and co-workers have designed a 3D copper current collector (3D-Cu) that functionalizes the Cu with partially reduced graphene oxide (denoted as rGO@3D-Cu) to create a potassiophilic surface.^[220] Potassiophilic versus potassiphobic experiments show that molten K can rapidly wet the rGO@3D-Cu, but cannot wet the pristine unfunctionalized 3D-Cu. The rGO@3D-Cu achieves a unique synergy through interfacial and geometry. The rGO layer on the surface can promote the growth of 2D layer-by-layer metal film at early stage of electroplating, while the 3D-Cu framework can reduce the current density and avoid the formation of dendrites. As a result, the symmetric rGO@3D-Cu cells exhibit stable cycling at 0.1–2 mA cm⁻², while the symmetric 3D-Cu cells failure when the current is increased to 0.5 mA cm⁻². In addition, the half-cells are stable at 0.5 mA cm⁻² for 10 000 min (100 cycles), and at 1 mA cm⁻² for 5000 min.

Carbon-based hosts are more attractive than metallic hosts due to their advantages of lightweight, abundant resources, low cost, flexibility and good electrochemical stability. Qin et al. have used an aligned carbon nanotube membrane (ACM) as host for KMA.^[221] The ACM has the following advantage. First, the aligned structure of ACM provides strong capillary forces, which improves the wettability to molten K, and provides a large pore-volume space to store molten K. Second, the robust ACM host retains its original structure after molten metal infusion, achieving physically encapsulation of K metal and buffering the volume change during the electrochemical cycling. Third, the large surface area of ACM host leads to a lower local current density and inhibits the uneven deposition of K. Finally, the inert carbonaceous substrate is a lightweight current collector, which is of great significance to improve the overall capacity of electrode. As a result, the Na symmetrical cell with the K-ACM anode shows a stable plating/stripping process with low polarization (0.1 V) in traditional carbonate-based electrolytes. In the full cell assembled with the K-ACM anode and Prussian blue cathode, the growth of dendrites is inhibited and the anode can exhibit excellent stability (more than 10 000 min at current density of 2 mA cm⁻²).

Another strategy for modifying metal anodes is to regulate nucleation of the metal. As discussed in Sections 2.2.1 and 3.2.1, the chemical properties of the material surface also influence its wettability to molten K, and affect the initial nucleation, nucleation density and subsequent growth kinetics of Na during the cycling. In order to modify the wettability and the nucleation of Na, it is necessary to introduce heteroatomic functional group into host. Li et al. have compared the original electrochemical deposition behavior of K metal on three different substrates including puffed millet (PM), PM/NiO and Cu by testing the overpotential and calculating the Gibbs free energies.^[222] The result shows that NiO acts as nucleation site to reduce the nucleation barrier for the homogeneously deposition of K metal and avoid the growth of dendrites, and forms a well-knit root structure to accommodate K metal by combining with PM. After a large number of K metal is deposited, the PM/NiO/K electrode remains stable and exhibits excellent electrochemical performance, with high CE (>99.8% in average) for more than 200 cycles in symmetric cells. Tang et al. have successfully constructed a MXene-based host for KMAs.^[223] The K metal is encapsulated into a titanium-deficient nitrogen-containing MXene/carbon nanotube freestanding scaffold. On the one hand, the rapid K⁺ diffusion and high conductivity in the scaffold reduce the local current density and promote the uniform ionic flux during electrochemical cycling. On the other hand, according to the results of experimental and DFT calculations, the potassiophilic MXene sheets can induce the nucleation of K, which is uniformly deposited on the scaffold upon cycling. As a result, the constructed anode can exhibit a high CE (98.6%), low overpotential (6 mV) and excellent cyclic stability (>1000 h) without dendrites growth during electrochemical cycling. Compared with bare metal potassium anode, the electrochemical performance of K–S full batteries can be significantly improved by using the MXene-based KMA.

4.2. Ca–S Batteries

Ca–S batteries have been studied due to the natural abundance and high melting point of Ca.^[224] See and Seshadri proposed the prototype Ca–S battery but Ca plating cannot be carried out during charging because of the formation of passivation films on the Ca-metal anode (CMA) in common organic electrolytes.^[10a] Ponrouch et al. have prepared Ca-based batteries with an electrolyte composed of Ca(BF₄)₂ salts and carbonate-base solvent for reversible electroplating/stripping of Ca at a high temperature.^[225] Subsequently, Wang et al. have prepared a Ca(BH₄)₂-based electrolyte suitable for RT Ca-based batteries.^[226] Ca alkoxyborate salt has also been proposed to promote the reversible electroplating/stripping of Ca at RT and research of Ca–S batteries has so far focused on electrolyte optimization and the energy-storage mechanism.^[227]

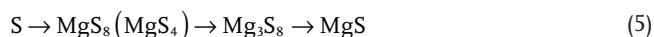
Antonio et al. have demonstrated the reversible activity in a proof-of-concept RT Ca–S battery.^[10b] The Ca–S battery composed of a simple cathode of S on an activated carbon cloth with a fluorinated alkoxyborated-based electrolyte shows medium-term cyclic stability with low polarization. The electrochemical mechanism of the Ca–S battery system is investigated by in situ and ex situ spectroscopic techniques (XPS and XAS) (Figure 19b). By

analyzing the surface and bulk of the samples, evolution of S and Ca species in the battery is determined and information about the decomposition products formed during charging and discharging is obtained. The electrochemical species are composed of 80% CaS and 20% short-chain Ca polysulfides (CaPSs, including CaS₂ and CaS₃) after discharging to 0.5 V. During charging, a mixture composed of 8% CaS and 92% long-chain CaPSs is recovered, indicating that the reversible transformation of S species occurs during discharging and charging. The different S species are also determined by separate analysis of the multivariate curve using least square based on in situ XAS. The trend indicates that shorter CaPSs are formed during discharging but no radical CaPSs can be observed in large quantities from the Ca–S battery. All in all, the mechanism of the Ca–S battery is similar to that of Li–S and RT Na–S batteries. The amount of S decreases implying that the CaPSs species are not retained by the carbon support. Even after combining S with the carbon host, reduction of S species does not change significantly and therefore, considering that the reaction is similar to that of the Li–S batteries, electrochemical catalysis is an effective way to improve the electrochemical properties of Ca–S batteries. In the future, more research about cathode, anode and electrolyte with catalytic effect should be carried out to enhance the electrochemical stability and kinetics of Ca–S batteries.

4.3. Mg–S Batteries

As an advanced energy-storage system, Mg–S batteries can store two valence electrons per Mg atom thus producing a high theoretical specific capacity of 2205 mAh g⁻¹ and volumetric capacity of 3833 Ah L⁻¹. In addition, Mg metal is less reactive than Li metal in both air and organic electrolytes rendering Mg–S batteries safer. However, several challenges hinder the development of Mg–S batteries, for instance, the incompatibility between Mg²⁺ and organic electrolytes, high polarization, low CE, and fast capacity fading resulting from the shuttle effect of intermediates. Substantial efforts have been made to match S cathodes with feasible electrolytes to achieve rapid and reversible electroplating/stripping of Mg.^[228]

Mg–S batteries have a similar electrochemical reaction pathway as Li–S and RT Na–S batteries. During discharging, elemental S is reduced to soluble intermediates and then the final product precipitates on the cathode.^[1,228] Xu et al. have used Mg(HMDS)₂-AlCl₃ as the electrolyte in Mg–S batteries and studied the electrochemical mechanism during charging and discharging by in situ x-ray absorption spectroscopy.^[229] As shown in Figure 19c, the major electrochemical process consists of three steps as shown in the following



During discharging, the first step is a rapid solid–liquid phase reaction from S to MgS₈/MgS₄ which is reduced slowly to Mg₃S₈ and eventually MgS. The third step is more sluggish because it is a solid–solid reaction. During charging, only a small amount of MgS is oxidized to form Mg₃S₈ and most of the MgS and Mg₃S₈ cannot be reduced back to long-chain Mg polysulfides (MgPSs) or elemental S.

Similar to other M–S batteries, the challenges of the S cathode in Mg–S batteries can be tackled by combining S with the carbon matrix.^[230] Xu et al. have used TiS₂ as a catalyst to accelerate conversion from MgS to high order MgPSs in Mg–S batteries and solve the challenge posed by rapid capacity decay.^[229] However, the Mg–S batteries have relatively low specific capacity and cyclic stability. Catalysts can be introduced into the carbon host to catalyze transformation of S species and improve the conductivity, capacity, and cyclic stability of the S cathode. Sun et al. have synthesized carbon-confined Co in a mesoporous carbon matrix (MesoCo@C) by in situ sulfurization.^[48] During injection of molten S, the in situ sulfurization process occurs due to the high surface energy of nanosized Co particles followed by oxidation by melting S to form CoS_x. CoS_x not only inherits the conductivity and large binding energy of MgPSs, but also improves the kinetics of the multistage S/S²⁻ redox reactions. The MesoCo@C/S shows a high initial capacity of 830 mAh g⁻¹ at 0.1 C and excellent cyclic stability with a high reversible capacity of 280 mAh g⁻¹ at 0.2 C after 400 cycles. Zhao et al. have prepared a Co₃S₄@MXene heterostructure as a host in high-performance Mg–S batteries that are compatible with the common APC electrolyte.^[50] The MXene nanosheets provide a continuous conductive framework for rapid electron transfer and the terminal negative F atom of MXene blocks the S species from reacting with the nucleophilic electrolyte. Meanwhile, Co₃S₄ on the surface of MXene forms sulfophilic sites for the intermediates to accelerate conversion of MgPSs. As a result, the Mg–S battery consisting of the Co₃S₄@MXene/S has a high specific capacity of 1220 mAh g⁻¹ as well as cyclic stability. These works reveal that catalytic effect can improve the electrochemical performance of Ca–S batteries.

4.4. Al–S Batteries

Al–S batteries can store valence electrons and have high specific gravimetric capacity of 2980 mAh g⁻¹ and volumetric capacity of 8050 mAh g⁻¹. Ionic-liquid (IL)-based electrolytes can be used to realize reversible electroplating/stripping of Al in discharging and charging.^[231] The Al–S battery with an Al-metal anode (AMA) and an ionic liquid electrolyte is not vulnerable to burn even if the battery package is damaged.

The research of Al–S battery dates back to 1993. The prototype Al–S battery consists of a high concentration aqueous alkaline electrolyte, polysulfide catholyte with carbon textile as a current collector, and an AMA.^[232] However, feasible deposition and dissolution of Al cannot be achieved due to the amphoteric nature of Al. Fortunately, AlCl₃-based ILs as electrolytes can be used to achieve reversible Al electroplating/stripping in rechargeable Al batteries.^[224,233] Cohn et al. have designed a rechargeable Al–S battery using a nonaqueous IL electrolyte and more advances have been made in recent years.^[224,234] Wang et al. have used 1-ethyl-3-methylimidazolium chloride (EMICl)/AlCl₃ (1:1.3) IL as an electrolyte to prepare Al–S batteries that show a high capacity of 1000 mAh g⁻¹ for 20 cycles. Gao et al. have reported that the electrochemical reaction of S with Al occurs in the solid state, because elemental S, intermediate Al polysulfides (AlPSs, including S₆²⁻ and S₄²⁻ species), and final product (Al₂S₃) hardly dissolve in ILs.^[235] The

insolubility and insulating nature of these substances give rise to a high kinetic barrier during electrochemical cycling of Al–S batteries.

Research of Al–S batteries and the related cathode materials has been limited. The C/S composite can improve the electrochemical properties of Al–S batteries but the slow dynamic response and short lifetime of Al–S batteries are serious hurdles. Guo et al. have prepared Cu nanoparticles-decorated microporous carbon by direct carbonization as a host of S in Al–S batteries.^[51] The strong interaction between Cu and S and excellent conductivity of Cu improve the reaction kinetics of S and Al, utilization of S, and the specific capacity. Guo et al. have used Co^{II,III} as an electrochemical catalyst in the S host to reduce the overpotential and improve capacity retention as well as rate performance of Al–S batteries (Figure 19d).^[10f] The electrocatalytic effects on the electrochemical reaction of S are observed from Co^{II,III} supported carbon matrix and dispersed in the ILs electrolyte. During discharging and charging, Co ions are transferred to Co sulfides with the valance states changed to Co^{II,III}. Consequently, the Al–S battery comprising the Co supported carbon matrix has a low overpotential of 0.8 V and high specific capacity of 500 mAh g⁻¹ after 200 cycles. This study suggests the good potential of using electrochemical catalysts to improve the electrochemical characteristics of Al–S batteries.

Up to now, the study of these M–S batteries is still in its infancy and little work has been done. This is mainly due to the harsh synthesis conditions for K–S batteries and the mismatch between multivalenced metal ions and electrolyte. However, due to the advantages of these M–S batteries such as ultrahigh specific capacity and low-cost, further research on these M–S batteries needs to be carried out to realize their practical applications. With the development of the Li–S and RT Na–S batteries, many novelty characterization technologies have been successfully applied to the basic research and many fundamental principles have revealed. These research method and advanced characterization technologies can also be transplanted to the research of other M–S batteries, which will greatly promote the development of these M–S batteries.

5. Practical Applications

In the past, LIBs have dominated the markets such as portable electronics and electric vehicles due to their superior performance. However, the commercial LIBs are approaching theoretical limits in terms of gravimetric and volumetric energy density, which cannot meet the intense demand of the market. M–S batteries are a promising alternative to LIBs due to their high energy density and cheap raw materials.^[236] However, the current research on M–S batteries is mainly focused on coin-cell, and there are few studies on pouch cells or packaged batteries. And studies on the effect of catalysts on the performance of bag or box cells are also scarce. To the best of our knowledge, only about 15 papers have discussed the assembly of pouch cell Li–S batteries using S cathode with catalyst.

Compared to the different cell formats, including cylindrical and prismatic-hardcase, pouch cells seem to be superior to maximize the specific energy due to the light cell packaging. Unlike

the coin cells commonly assembled in the laboratory, pouch cell contains a large number of pole pieces with abundant active substances via lamination process, causing many serious problems which greatly weaken the performance of batteries.^[236a,237] First, the formation of dendrites and the cracks in the reformation of SEI layer during electrochemical cycling lead to the loss of electrolyte.^[238] Second, the thick S cathode and the lean electrolyte condition lead to poor reaction kinetics, which seriously affects the utilization of S. Compared with the coin cell, the shuttle effect of pouch cells is more stronger during electrochemical cycling because much more S molecules take part in the conversion of S species, resulting in capacity decay and low CE. In addition, the problems of metal anode such as Li metal powdering and the formation of Li dendrite and dead Li causing the failure of pouch cell are more serious compared with the shuttle effect. Finally, when the overcharge voltage rises to 4.2 V, the temperature of the battery rise rapidly and the electrolyte oxidizes. The heat accumulated inside the cell causes the decomposition of electrolytes and/or active materials, resulting in thermal runaway. Based on the above discussion, reasonable design of cathode loading, electrolyte amount and anode thickness are of great significance to optimize the electrochemical performance on the full cell level. In this section, we discuss the development of catalysts toward the practical application of Li–S batteries.

5.1. Cathodes

Up to now, the research on the role of catalyst in the conversion of LiPSs is still in its infancy, and a comprehensively fundamental understanding of the catalytic mechanism is needed to maximize the potential of Li–S batteries. Most of the research on Li–S battery catalysts is focused on exploiting new materials with excellent electrochemical performance, rather than the practical application of catalysts. Fortunately, this has been changed in the past few years. Shao et al. have synthesized Fe single-atom embedded N-doped mesoporous hollow carbon sphere (Fe-N/MHCS) as multieffect nanoreactors for S.^[58b] Due to the electrocatalysis of single-atom Fe, the cathode displays a high areal capacity of 6.4 mAh cm⁻² and a high capacity retention of 81.7% after 100 cycles under the high S loading of 5.4 mg cm⁻² and low electrolyte/S (E/S) ratio of 8 μ L mg⁻¹. The pouch cell assembled under the high S loading of 2 mg cm⁻² and low E/S ratio of 6 μ L mg⁻¹ also has a high initial capacity of 459 mAh (corresponding to specific discharge capacity of 1257 mAh g⁻¹) at 0.2 C. In addition, a high capacity of 354 mAh as well as a high capacity retention of 77.1% are remained after 200 cycles. The electrochemical performance of the pouch cell undoubtedly confirms that the Fe-N/MHCS loaded with S has great practical application potential in high specific energy and long lifetime Li–S batteries.

It is worth noting that SACs are always highly unstable and tend to aggregate due to their high-surface free energy. Moreover, the cost of electrodes is a vital factor affecting their commercial application. Although the SACs can maximum the use of each atom, their manufacturing process are complex and time-consuming, which increases the cost and discourages the mass production of SACs. The low-cost bimetallic alloy catalysts

have also been used for S cathodes in Li–S batteries.^[239] He et al. have proposed a cost-effective hexagonal close-packed (hcp)-phase Fe–Ni alloy acting as electrocatalyst for accelerating LiPSs conversion in Li–S batteries.^[240] To fully demonstrate its potential for commercial application, a pouch cell with Fe–Ni/S cathode is tested under the realistic conditions required for practical Li–S batteries. The pouch cell assembled with a S loading of 4.1 mg cm⁻² is measured under a low E/S ratio of 4.5 μL mg⁻¹. Surprisingly, the pouch cell shows excellent cyclic stability and remains stable over 66 cycles. Furthermore, the capacity of Fe–Ni/S cathode retains stable after 30 days, while the capacity of C/S cathode shows a huge loss, indicating that the self-discharge problem is significantly mitigated in the Fe–Ni alloy. In addition, the polyoxometalates (POMs), a kind of atomically well-defined metal-oxide clusters, are ideal molecular systems to explore the trapping of single-metal atom.^[241] It has been used as a trapper for LiPSs, and thus improving the electrochemical performance of Li–S batteries. Recently, Lei et al. have proposed a single-dispersed molecular cluster catalyst composite ({Co₄W₁₈}/rGO) consisting of a polyoxometalate framework ([Co₄(PW₉O₃₄)₂]¹⁰⁻) and multilayer reduced graphene oxide.^[15] A single-electrode pouch cell based on winding single-side-coat {Co₄W₁₈}/rGO/S cathode is assembled with a S loading of 3.6 mg cm⁻² and an lean electrolyte condition (5 μL mg⁻¹). The pouch cell shows a high reversible capacity of 795 mAh g⁻¹ after 100 cycles at 0.2 C, demonstrating that the {Co₄W₁₈}/rGO has great potential for practical application.

Naturally, an excess of electrolyte and Li are good for the cycle life of cell, but not good for the energy density of cell. An excess of Li and electrolyte have a significant impact on the volume and weight of cell. In most test environment (E/S > 4 μL mg⁻¹, ratio of anode and cathode (N/P) > 4), Li–S batteries not only have low specific energy value less than 100 Wh kg⁻¹, but also have high cost of raw materials. To achieve the goal of 300 Wh kg⁻¹, the E/S ratio must be less than 4 μL mg⁻¹ and the areal capacity should be at least 6 mAh cm⁻². Zhao et al. have designed a catalytic S host by embedding polar ZnS nanoparticles and Co–N–C SAC double-end binding sites into a highly oriented macroporous conductive framework (3d-omsh/ZnS, Co–N–C).^[58a] A 100 mg-level pouch cell is firstly fabricated and then cycled at a current density of 0.2 A g⁻¹. The cell shows a specific capacity of over 800 mAh g⁻¹ with a high capacity retention ratio of 80.32%. Besides, pouch cells with 200 mg S loading on different host materials are also assembled and tested. Compared with other hosts, the pouch cell with 3d-omsh/ZnS, Co–N–C/S cathode provides an excellent cyclic stability and CE close to 100% within 20 cycles. To further demonstrate the potential for application, an A-h-level pouch cell with 3d-omsh/ZnS, Co–N–C host materials is assembled. It is noteworthy that the Li metal is only 100% excess (corresponding to an anode/cathode capacity ratio of 2.6), and the E/S ratio is controlled at 4 μL mg⁻¹. What's more, the S loading is increased to 1.2 g with a double-side coating (corresponding to 6 mg cm⁻²). The constructed pouch cell shows a high capacity of 1200 mAh g⁻¹ at 41.67 mA g⁻¹ and a high practical specific energy of 317 Wh kg⁻¹, indicating a high S utilization under the lean electrolyte and high S loading conditions. When the E/S ratio is reduced to 2.5 μL mg⁻¹, the specific energy of the pouch cell further increases to 352.4 Wh kg⁻¹. In addition, the A-h-level Li–S

pouch cell still provides high CE (>95%) and stable cycling performance at the current density of 83.33 mA g⁻¹. This work has greatly shortened the gap between the high-performance of Li–S batteries and their realization for practical application.

5.2. Anodes

It is well known that the LMA is also an important part of the practical application of Li–S batteries. Recently, Zhang et al. have reported an advanced LMA with an electronic-modulation layer consisting of the electronic densities modulated CeO₂ and conductive and interconnected N-doped carbon nanotubes networks (SDMECO@HINC) for Li–S batteries.^[58d] The Schottky defects can regulate the 4f-center electron structure of the catalyst and provide a large number of active sites to accelerate the Li transport kinetics. DFT calculation and experimental results show that due to Schottky defects, the electron density is redistributed and affected, providing a large number of active catalytic centers with stronger ion diffusion capability to guide the horizontal Li deposition, thus avoiding the formation of dendrites. This artificial electronic-modulation layer can significantly decrease the desolvation, nucleation, and diffusion barrier. When the current density is 0.5 mA cm⁻², the catalytic modulation of SDMECO@HINC on the LMA makes the diffusion and plating behaviors of Li atoms much easier, and the overpotentials stabilize at 11 mV, which is lower than that of pristine LMA (19 mV). Even when the current density reaches 2 mA cm⁻², the overpotential of SDMECO@HINC modified LMA remains at 100 mV within 700 h. The rebuilt interfacial electron structure by Schottky defects is also beneficial to the adsorption of S species and accelerates their conversion. As a result, the pouch cell consists of SDMECO@HINC modified cathode and anode can provide a high initial specific capacity of 1053 mAh g⁻¹ at 0.1 C (corresponding to an energy density of 2264 Wh kg⁻¹) and outstanding cyclic stability (energy density stabilizes at 1050 Wh kg⁻¹ after 100 cycles). This work demonstrates a promising potential for realizing high-safety and long-cycling Li–S batteries.

5.3. Functional Separators

The realization of advanced functions in flexible and wearable electronics, like smart textiles or rolled-up touch screens, requires batteries seamlessly built into these soft products.^[58e,242] Therefore, preparing batteries with both high energy density and excellent flexibility is urgent. In the past several decades, the tremendous development of cutting-edge material has enabled Li–S batteries to combine high energy density, long cycle life, and good flexibility.^[243] Zhang et al. have prepared the flake-like cobalt vanadium oxide (CVO) via the solvothermal method and used it to modify the separator to improve the electrochemical performance of Li–S batteries.^[58f] The chemical bonds of V–S and Li–O cause the strong chemical interaction between the CVO and LiPSs, which effectively confines the LiPS generated. At the same time, the active Co sites ensure the fast kinetic conversion of the anchored LiPSs

and accelerate their reversible redox reactions, thus providing outstanding cycling stability of Li–S batteries based on the CVO modified separator. In particular, the CVO layer covering the surface of the separator does not damage the mechanical properties of the separator, and the modified separator can be used directly in soft-packaged batteries. The CV curves of the soft-packaged batteries assembled at different bending states show a similar shape to the case of the coin cell. It also shows similar charge resistance even in different bending states, indicating that the batteries have good stability in the electrochemical process. The assembled soft-packaged battery can deliver a high capacity of 952 mAh g⁻¹ under no bending strains and 865.8 mAh g⁻¹ with a bending diameter of 2.0 cm at 1.0 C. When the assembled soft-packaged battery returns to the initial flat state after successively bent to the diameters of 3.0 and 2.0 cm, a reversible capacity of 796 mAh g⁻¹ is delivered after 100 cycles, further demonstrating the electrochemical stability. This work provides a method to design active material decorative separators to improve the electrochemical performance of practical Li–S batteries.

Reasonable and effective regulation is necessary to simultaneously improve the performance of LMA and S cathode, which can be achieved by using a modified separator. In this case, Zhou et al. have prepared Pt single-atoms (SAs)-regulated heterostructure of In₂S₃/Ti₃C₂ binary nanosheets (Pt SAs/In₂S₃/Ti₃C₂) modified separator for dendrite-free and dynamic-enhanced Li–S batteries.^[58e] This separator not only can stabilize the Li plating/stripping on LMA at a high current density of 5 mA cm⁻² but also can suppress the shuttle effect and accelerate the conversion of LiPSs during the electrochemical cycling. To reveal the practical application possibility of the Pt SAs/In₂S₃/Ti₃C₂ modified separator, the researchers have assembled the soft-packaged batteries (3.0 cm × 3.0 cm) using a super P@S as cathode with an S mass loading of ≈6.4 mg cm⁻², Li strip on Cu foil as anode and the appropriate ether-based electrolyte (DME/DOL, E/S = 10 μL mg⁻¹). The CV curves of the soft-packaged batteries are similar to those of the corresponding coin-type cells, and their redox peaks almost overlap at different bending angles. The flexible soft-packaged Li–S battery can provide a high initial capacity of 5.54 mAh cm⁻² at 0.2 C. Besides, the soft-packaged battery has no obvious capacity fading when continuously charged and discharged under different degrees of bending. After 300 cycles, the soft-packaged battery has ultrahigh capacity retention of 89.3% (areal capacity of 4.95 mAh cm⁻²), demonstrating that the Pt SAs/In₂S₃/Ti₃C₂ modified separator can be practically used as a separator in flexible Li–S batteries.

To achieve the widely application of advanced Li–S technology, each component of the battery needs to be furtherly performed under practical condition. The test data from the coin cell cannot be derived for determining characteristics relevant to application-oriented development, such as energy density and power capability. Besides, the effect of pressure on pouch cells also needs to be further investigated. What's more, some new problems will appear during the fundamental research and need to be overcome regarding both lab cell and prototype cell. Finally, for M–S batteries, the research roadmap of Li–S batteries can provide reference for the practical application of other M–S batteries.^[59d]

6. Conclusion and Prospective

The current understanding of the catalytic effects of high-performance M–S batteries are described and summarized based on recent publications in the past several years. The research background and challenges of M–S batteries are described from the viewpoint of the working mechanisms of Li–S and RT Na–S batteries as well as challenges confronting the design of the anode and cathode. Recent progress pertaining to different types of catalytic materials including metal-based nanomaterials, metal compounds and heterostructures is summarized. The proper structural design can achieve high cyclic stability and high electrochemical reaction rates for cathode and anode materials in Li–S and RT Na–S batteries. Advanced electrolyte systems with catalytic effects for M–S batteries are described and finally, future development of catalytic effects for next-generation M–S batteries is discussed.

In the metal–S batteries, the sluggish redox reaction of S is a key problem limiting their electrochemical performance. Unlike traditional adsorbents and mediators, catalysts can simultaneously adsorb soluble intermediates and accelerate the conversion of polysulfides. Based on recent research studies of the catalytic effects in Li–S and RT Na–S batteries, it is suspected that the intermediates are first anchored by catalysts. Then, the catalytic active sites on the surface of the catalyst effectively reduces the reaction barrier of polysulfides conversion, which greatly improves the conversion kinetics of polysulfides. Therefore, the ideal catalyst medium should have excellent electrical conductivity, large active surface, as many active sites as possible and appropriate affinity for intermediates, thus improving the redox kinetics of S cathode. Coupling with the design of the electrode structure and electrolyte, the electrochemical characteristics such as the cyclic stability and rates are further improved. For example, although TiO₂ adsorbs strongly on NaPSs to alleviate the shuttle effect, its poor electron conductivity limits electrochemical conversion. Hence, introduction of TiO₂ to a porous carbon host with high electron conductivity can mitigate the shuttle effect of NaPSs while improving the rate performance of RT Na–S batteries. Moreover, due to the similar reaction mechanism of Li–S batteries, the problems of S cathode for other M–S batteries including shuttle effect of intermediates and large volume change also mainly prevent their development. So far, the electrocatalyst used for advanced S cathode in Li–S and RT Na–S batteries can also be transplanted into other M–S systems to realize high-performance M–S batteries. In addition, the development of RT Na–S batteries and other M–S batteries lag behind the Li–S batteries. Advanced medium hosts and characterization techniques in Li–S batteries can be transplanted into these M–S battery systems, which is helpful to develop high-performance M–S batteries and reveal their basic reaction mechanisms.

Up to now, introducing a conductive host and regulating nucleation are two directions in solving the problems of LMAs (or SMAs). The conductive host can buffer the volume change and inhibit the dendrite growth of Li (or Na) via the scattering of deposited Li⁺ (or Na⁺) flux and local charge density. As for regulating the nucleation and deposition behaviors, the interfacial barrier is weakened and Li⁺ (Na⁺) can be deposited uniform on the LMAs (or SMAs), which significantly keep the stable of LMAs (or SMAs). The host materials with high affinity can

adsorb Li^+/Na^+ , and the adsorbed Li^+/Na^+ tends to diffuse to the surface of the host first and then uniformly deposit on its surface. So far, the development of LMAs and SMAs are still in infancy and many challenges need to be solved. In addition, the natural difference between Na and Li causes the fundamental mechanisms of dendrite growth in LMAs and SMAs are different, which determines the strategy of their development are distinguishable. In this case, the in situ technique, Cyto-TEM, and other advanced characterization technique as well as theoretical calculation are urgently needed to reveal the interface structures and behaviors in LMAs and SMAs. In addition, since recapturing “dead Li/Na” can improve the performance of Li–S or RT Na–S batteries, strategies for capturing “dead Li/Na” also need to be developed. For example, developing advanced electrolyte systems and host materials that can utilize “dead Li/Na.”

A suitable electrolyte solution of intermediates can promote the reactivity of S cathode. But the solution capability of intermediates also needs to be controlled because it damages the performance of Li–S and RT Na–S batteries. Besides, adjusting the formation of CEI and SEI films can effectively buffer the diffusion of intermediates and the corrosion of metal anodes, significantly improving the electrochemical properties of Li–S and RT Na–S batteries. What's more, some compounds can improve the reaction kinetic of batteries. However, the unclear formation mechanism of CEI and SEI causes their component cannot be quantified, increasing the difficulty of the electrolyte design. The problems of electrolyte are more serious in other M–S batteries, resulting in their development are much slower than Li–S or RT Na–S batteries. Although some electrolytes with excellent performance have been developed by researchers, the reaction mechanism between electrolytes, additives and intermediates needs to be further studied in these systems. As mentioned above, it is necessary to study how to recycle the “dead metal” via electrolyte in order to improve the utilization of metal anodes.

In addition, there are some other issues that need to be addressed. Firstly, although the catalytic effects in M–S batteries have been investigated, complete understanding of the catalytic effects in M–S batteries needs more research. Through the development of advanced in situ characterization techniques, it is expected to reveal the mechanism existing in M–S batteries deeply in the near future. Secondly, heterostructured materials can realize adsorption and conversion of polysulfide intermediates, but their use in M–S batteries have been limited until recently. By designing heterostructure catalysts with excellent performance and studying the preparation method of heterostructure catalysts, the performance of M–S batteries can be further improved. Thirdly, an advanced electrolyte with the desirable catalytic effects is crucial to the battery system and must be optimized to achieve the best electrochemical stability and kinetics on S and metal anodes, but research in this area is still lacking and our understanding of the mechanism is still inadequate. Therefore, it is necessary to combine advanced characterization technology to systematically study the catalytic effect of electrolyte in order to maximize the performance of the battery. Fourthly, the development of catalyst materials for M–S batteries has mainly focused on Li–S and RT Na–S batteries and other types of M–S batteries have not been investigated as much, especially K–S batteries. It is necessary to design suitable

catalysts to overcome the energy barrier in the electrochemical process and promote the transformation of K_2S_3 to K_2S_2 and K_2S in the discharging process and improve the charging and discharging capacities of K–S batteries. Fifthly, the nature of the catalysts is very important to the application of M–S batteries. Since the structure affects the electrochemical performance of M–S batteries, it must be investigated and optimized systematically and comprehensively. Sixthly, although catalytic effect can improve the electrochemical performance of cathode and anode, it is still necessary to regulate the ratio of different components (such as electrolyte/S or anode/cathode) or other parameters to realize the practical application of M–S full batteries. Finally, how to control the cost of M–S batteries is the key factor affecting their practical application. As we discussed above, the SACs can maximum the use of each atom, causing great concern among researchers in many fields. However, their complex and time-consuming manufacturing process increase the cost and discourage the mass production of SACs. Moreover, the high-surface free energy of SACs makes the material highly unstable, which leads to the aggregation of metal atoms and reduces the stability of M–S batteries. Conversely, the low-cost, well-developed and simple synthesized bimetallic alloys can also provide good electrochemical performance for M–S batteries. Therefore, the low-cost bimetallic alloys loaded on conductive frameworks as hosts or directly acted as 3D current collectors maybe a better choice for electrode in M–S batteries. In addition, the traditional metal nitrides have gained commercial application in many fields due to their natural electrical conductivity, excellent stability, low-cost and mature preparation process. Since the traditional metal nitrides have good adsorption ability and catalytic effect on polysulfides, they are another superior choice as catalyst materials for M–S batteries. In the future, research on low-cost catalysts will need to be carried out further to meet possible commercialization needs.

Acknowledgements

L.Z. and J.Z. contributed equally to this work. This work was financially supported by the Science and Technology Innovation Commission of Shenzhen (JCYJ20180507182047316), Shenzhen Excellent Science and Technology Innovation Talent Training Project – Outstanding Youth Project (RCJC20200714114435061), Shenzhen – Hong Kong Innovative Collaborative Research and Development Program (SGLH20181109110802117 and CityU 9240014), and Shenzhen – Hong Kong Technology Cooperation Funding Scheme (TCFS) (GHP/149/20SZ and CityU 9440296).

Conflict of Interest

The authors declare no conflict of interest.

Keywords

catalytic effect, electrolytes, metal anodes, metal–sulfur batteries, sulfur cathodes

Received: May 23, 2022

Revised: July 7, 2022

Published online: October 31, 2022

- [1] X. D. Hong, J. Mei, L. Wen, Y. Y. Tong, A. J. Vasileff, L. Q. Wang, J. Liang, Z. Q. Sun, S. X. Dou, *Adv. Mater.* **2019**, *31*, 1802822.
- [2] a) M. Armand, J. M. Tarascon, *Nature* **2008**, *451*, 652; b) B. Dunn, H. Kamath, J. M. Tarascon, *Science* **2011**, *334*, 928; c) B. W. Zhang, T. Sheng, Y. D. Liu, Y. X. Wang, L. Zhang, W. H. Lai, L. Wang, J. P. Yang, Q. F. Gu, S. L. Chou, H. K. Liu, S. X. Dou, *Nat. Commun.* **2018**, *9*, 4082.
- [3] a) J. Liang, F. Li, H.-M. Cheng, *Energy Storage Mater.* **2017**, *7*, A1; b) M. Sathiya, G. Rouse, K. Ramesha, C. P. Laisa, H. Vezin, M. T. Sougrati, M. L. Doublet, D. Foix, D. Gonbeau, W. Walker, A. S. Prakash, M. Ben Hassine, L. Dupont, J. M. Tarascon, *Nat. Mater.* **2013**, *12*, 827; c) G. Q. Tan, F. Wu, Y. F. Yuan, R. J. Chen, T. Zhao, Y. Yao, J. Qian, J. R. Liu, Y. S. Ye, R. Shahbazian-Yassar, J. Lu, K. Amine, *Nat. Commun.* **2016**, *7*, 11774; d) J. A. Rogers, T. Someya, Y. G. Huang, *Science* **2010**, *327*, 1603.
- [4] a) Q. Q. Lu, Y. L. Jie, X. Q. Meng, A. Omar, D. Mikhailova, R. G. Cao, S. H. Jiao, Y. Lu, Y. L. Xu, *Carbon Energy* **2021**, *3*, 957; b) C. Chu, R. Li, F. Cai, Z. Bai, Y. Wang, X. Xu, N. Wang, J. Yang, S. Dou, *Energy Environ. Sci.* **2021**, *14*, 4318.
- [5] a) X. C. Lu, B. W. Kirby, W. Xu, G. S. Li, J. Y. Kim, J. P. Lemmon, V. L. Sprenkle, Z. G. Yang, *Energy Environ. Sci.* **2013**, *6*, 299; b) Z. Y. Wen, Y. Y. Hu, X. W. Wu, J. D. Han, Z. H. Gu, *Adv. Funct. Mater.* **2013**, *23*, 1005.
- [6] X. L. Ji, K. T. Lee, L. F. Nazar, *Nat. Mater.* **2009**, *8*, 500.
- [7] C. P. Yang, Y. X. Yin, Y. G. Guo, L. J. Wan, *J. Am. Chem. Soc.* **2015**, *137*, 2215.
- [8] a) X. Liu, Y. Li, X. Xu, L. Zhou, L. Q. Mai, *J. Energy Chem.* **2021**, *61*, 104; b) X. W. Yu, A. Manthiram, *Adv. Funct. Mater.* **2020**, *30*, 2004084.
- [9] a) G. M. Zhou, E. Paek, G. S. Hwang, A. Manthiram, *Nat. Commun.* **2015**, *6*, 7760; b) G. L. Xia, L. J. Zhang, X. W. Chen, Y. Q. Huang, D. L. Sun, F. Fang, Z. P. Guo, X. B. Yu, *Energy Storage Mater.* **2018**, *14*, 314; c) L. Zeng, Y. Yao, J. Shi, Y. Jiang, W. Li, L. Gu, Y. Yu, *Energy Storage Mater.* **2016**, *5*, 50; d) P. X. Xiong, X. P. Han, X. X. Zhao, P. X. Bai, Y. Liu, J. Sun, Y. H. Xu, *ACS Nano* **2019**, *13*, 2536; e) Y. Liu, W. G. Wang, J. Wang, Y. Zhang, Y. S. Zhu, Y. H. Chen, L. J. Fu, Y. P. Wu, *Chem. Commun.* **2018**, *54*, 2288; f) X. M. Yuan, B. Zhu, J. K. Feng, C. G. Wang, X. Cai, R. M. Qin, *J. Power Sources* **2020**, *480*, 228874; g) L. Lin, C. K. Zhang, Y. Z. Huang, Y. P. Zhuang, M. J. Fan, J. Lin, L. S. Wang, Q. S. Xie, D. L. Peng, *Small* **2022**, 2107368.
- [10] a) K. A. See, J. A. Gerbec, Y. S. Jun, F. Wudl, G. D. Stucky, R. Seshadri, *Adv. Energy Mater.* **2013**, *3*, 1056; b) A. Scafuri, R. Berthelot, K. Pirnat, A. Vizintin, J. Bitenc, G. Aquilanti, D. Foix, R. Dedryvere, I. Arcon, R. Dominko, L. Stievano, *Chem. Mater.* **2020**, *32*, 8266; c) Q. L. Zou, Y. Sun, Z. J. Liang, W. W. Wang, Y. C. Lu, *Adv. Energy Mater.* **2021**, *11*, 2101552; d) Y. Xu, Y. X. Zhao, S. Y. Zhao, J. F. Zhang, J. Li, J. H. Guo, Y. G. Zhang, *Energy Storage Mater.* **2021**, *42*, 513; e) X. W. Yu, M. J. Boyer, G. S. Hwang, A. Manthiram, *Chem* **2018**, *4*, 586; f) Y. Guo, Z. Q. Hu, J. W. Wang, Z. Q. Peng, J. F. Zhu, H. X. Ji, L. J. Wan, *Angew. Chem., Int. Ed.* **2020**, *59*, 22963.
- [11] A. X. Wang, X. F. Hu, H. Q. Tang, C. Y. Zhang, S. Liu, Y. W. Yang, Q. H. Yang, J. Y. Luo, *Angew. Chem., Int. Ed.* **2017**, *56*, 11921.
- [12] L. Y. Du, Q. Wu, L. J. Yang, X. Wang, R. C. Che, Z. Y. Lyu, W. Chen, X. Z. Wang, Z. Hu, *Nano Energy* **2019**, *57*, 34.
- [13] S. Zhang, X. Ao, J. Huang, B. Wei, Y. Zhai, D. Zhai, W. Deng, C. Su, D. Wang, Y. Li, *Nano Lett.* **2021**, *21*, 9691.
- [14] W. G. Lim, Y. Mun, A. Cho, C. S. Jo, S. Lee, J. W. Han, J. Lee, *ACS Nano* **2018**, *12*, 6013.
- [15] J. Lei, X. X. Fan, T. Liu, P. Xu, Q. Hou, K. Li, R. M. Yuan, M. S. Zheng, Q. F. Dong, J. J. Chen, *Nat. Commun.* **2022**, *13*, 202.
- [16] W. Yao, C. Tian, C. Yang, J. Xu, Y. Meng, I. Manke, N. Chen, Z. Wu, L. Zhan, Y. Wang, R. Chen, *Adv. Mater.* **2022**, *34*, 2106370.
- [17] Y. Lu, J. L. Qin, T. Shen, Y. F. Yu, K. Chen, Y. Z. Hu, J. N. Liang, M. X. Gong, J. J. Zhang, D. L. Wang, *Adv. Energy Mater.* **2021**, *11*, 2101780.
- [18] J. He, A. Bhargava, A. Manthiram, *ACS Energy Lett.* **2022**, *7*, 583.
- [19] T. Wang, D. Luo, Y. Zhang, Z. Zhang, J. Wang, G. Cui, X. Wang, A. Yu, Z. Chen, *ACS Nano* **2021**, *15*, 19457.
- [20] Z. Du, Y. Guo, H. Wang, J. Gu, Y. Zhang, Z. Cheng, B. Li, S. Li, S. Yang, *ACS Nano* **2021**, *15*, 19275.
- [21] Q. Zhang, R. J. Gao, Z. X. Li, B. H. Zhou, A. D. Tang, J. Wang, J. J. Zou, H. M. Yang, *Small* **2022**, *18*, 2105661.
- [22] W. H. Wu, X. Y. Li, L. L. Liu, X. B. Zhu, Z. J. Guo, W. Guo, Q. Han, J. L. He, Y. Zhao, *J. Mater. Chem. A* **2022**, *10*, 1433.
- [23] J. Pu, Z. Wang, P. Xue, K. Zhu, J. Li, Y. Yao, *J. Energy Chem.* **2021**, *68*, 762.
- [24] H. Lin, H. Shi, Z. Wang, Y. Mu, S. Li, J. Zhao, J. Guo, B. Yang, Z.-S. Wu, F. Liu, *ACS Nano* **2021**, *15*, 17327.
- [25] X. Zhou, P. Zeng, H. Yu, C. M. Guo, C. Q. Miao, X. W. Guo, M. F. Chen, X. Y. Wang, *ACS Appl. Mater. Interfaces* **2022**, *14*, 1157.
- [26] D. Q. He, J. N. Liu, B. X. Zhang, M. Wang, C. N. Liu, Y. T. Huo, Z. H. Rao, *Chem. Eng. J.* **2022**, *427*, 131711.
- [27] Y. Ren, Q. Zhai, B. Wang, L. Hu, Y. Ma, Y. Dai, S. Tang, X. Meng, *Chem. Eng. J.* **2022**, *439*, 135535.
- [28] Q. Gu, Y. Qi, W. Hua, T. Shang, J. Chen, L. Jiang, L. Li, M. Lu, Y. Zhang, X. Liu, Y. Wa, B. Zhang, *J. Energy Chem.* **2022**, *69*, 490.
- [29] H. Ye, L. Ma, Y. Zhou, L. Wang, N. Han, F. Zhao, J. Deng, T. Wu, Y. Li, J. Lu, *Proc. Natl. Acad. Sci. USA* **2017**, *114*, 13091.
- [30] L. Zeng, J. Zhu, M. Liu, P. Zhang, *RSC Adv.* **2021**, *11*, 6798.
- [31] H. Shin, D. Kim, H. J. Kim, J. Kim, K. Char, C. T. Yavuz, J. W. Choi, *Chem. Mater.* **2019**, *31*, 7910.
- [32] S. Haldar, M. Wang, P. Bhauriyal, A. Hazra, A. H. Khan, V. Bon, M. A. Isaacs, A. De, L. Shupletsov, T. Boenke, J. Grothe, T. Heine, E. Brunner, X. Feng, R. Dong, A. Schneemann, S. Kaskel, *J. Am. Chem. Soc.* **2022**, *144*, 9101.
- [33] Z. C. Yan, J. Xiao, W. H. Lai, L. Wang, F. Gebert, Y. X. Wang, Q. F. Gu, H. Liu, S. L. Chou, H. K. Liu, S. X. Dou, *Nat. Commun.* **2019**, *10*, 4793.
- [34] A. Ghosh, A. Kumar, T. Dos, A. Ghosh, S. Chakraborty, M. Kar, D. R. MacFarlane, S. Mitra, *Adv. Funct. Mater.* **2020**, *30*, 2005669.
- [35] Z. C. Yan, Y. R. Liang, W. B. Hua, X. G. Zhang, W. H. Lai, Z. Hu, W. L. Wang, J. Peng, S. Indris, Y. X. Wang, S. L. Chou, H. K. Liu, S. X. Dou, *ACS Nano* **2020**, *14*, 10284.
- [36] W. Z. Bao, C. E. Shuck, W. X. Zhang, X. Guo, Y. Gogotsi, G. X. Wang, *ACS Nano* **2019**, *13*, 11500.
- [37] W. Y. Du, Y. K. Wu, T. T. Yang, B. S. Guo, D. Y. Liu, S. J. Bao, M. W. Xu, *Chem. Eng. J.* **2020**, *379*, 122359.
- [38] S. P. Zhang, Y. Yao, X. J. Jiao, M. Z. Ma, H. J. Huang, X. F. Zhou, L. F. Wang, J. T. Bai, Y. Yu, *Adv. Mater.* **2021**, *33*, 2103846.
- [39] Z. P. Huang, B. Song, H. Zhang, F. Feng, W. L. Zhang, K. Lu, Q. W. Chen, *Adv. Funct. Mater.* **2021**, *31*, 2100666.
- [40] L. F. Wang, H. Y. Wang, S. P. Zhang, N. Q. Ren, Y. Wu, L. Wu, X. F. Zhou, Y. Yao, X. J. Wu, Y. Yu, *ACS Nano* **2021**, *15*, 15218.
- [41] Y. R. Qi, Q. J. Li, Y. K. Wu, S. J. Bao, C. M. Li, Y. M. Chen, G. X. Wang, M. W. Xu, *Nat. Commun.* **2021**, *12*, 6347.
- [42] Q. J. Yang, T. T. Yang, W. Gao, Y. R. Qi, B. S. Guo, W. Zhong, J. Jiang, M. W. Xu, *Inorg. Chem. Front.* **2020**, *7*, 4396.
- [43] S. C. Wu, Y. H. Huang, C. R. Liao, S. Y. Tang, T. Y. Yang, Y. C. Wang, Y. J. Yu, T. P. Perng, Y. L. Chueh, *Nano Energy* **2021**, *90*, 106590.
- [44] X. L. Ge, H. X. Di, P. Wang, X. G. Miao, P. Zhang, H. Y. Wang, J. Y. Ma, L. W. Yin, *ACS Nano* **2020**, *14*, 16022.
- [45] Q. Zhao, Y. X. Hu, K. Zhang, J. Chen, *Inorg. Chem.* **2014**, *53*, 9000.
- [46] X. Yu, A. Manthiram, *Energy Storage Mater.* **2018**, *15*, 368.
- [47] Z. Li, B. P. Vinayan, T. Diemant, R. J. Behm, M. Fichtner, Z. Zhao-Karger, *Small* **2020**, *16*, 2001806.
- [48] J. Sun, C. Deng, Y. J. Bi, K. H. Wu, S. M. Zhu, Z. R. Xie, C. L. Li, R. Amal, J. Luo, T. B. Liu, W. Wang, *ACS Appl. Energy Mater.* **2020**, *3*, 2516.
- [49] Z. Zhao-Karger, R. Liu, W. Dai, Z. Li, T. Diemant, B. P. Vinayan, C. B. Minella, X. Yu, A. Manthiram, R. J. Behm, M. Ruben, M. Fichtner, *ACS Energy Lett.* **2018**, *8*, 2005.

- [50] Q. N. Zhao, R. H. Wang, Y. X. Zhang, G. S. Huang, B. Jiang, C. H. Xu, F. S. Pan, *J. Magnes. Alloy* **2021**, 9, 78.
- [51] Y. Guo, H. C. Jin, Z. K. Qi, Z. Q. Hu, H. X. Ji, L. J. Wan, *Adv. Funct. Mater.* **2019**, 29, 1807676.
- [52] H. Yang, L. Yin, J. Liang, Z. Sun, Y. Wang, H. Li, K. He, L. Ma, Z. Peng, S. Qiu, C. Sun, H.-M. Cheng, F. Li, *Angew. Chem., Int. Ed.* **2018**, 57, 1898.
- [53] W. Chu, X. Zhang, J. Wang, S. Zhao, S. Liu, H. Yu, *Energy Storage Mater.* **2019**, 22, 418.
- [54] D. Zhang, X. Zhang, B. Wang, S. He, S. Liu, M. Tang, H. Yu, *J. Mater. Chem. A* **2021**, 9, 8966.
- [55] J. Z. Sheng, Q. Zhang, M. S. Liu, Z. Y. Han, C. Li, C. B. Sun, B. Chen, X. W. Zhong, L. Qiu, G. M. Zhou, *Nano Lett.* **2021**, 21, 8447.
- [56] a) Y. Y. Liu, M. M. Han, Q. Z. Xiong, S. B. Zhang, C. J. Zhao, W. B. Gong, G. Z. Wang, H. M. Zhang, H. J. Zhao, *Adv. Energy Mater.* **2019**, 9, 1803935; b) X. L. Huang, Y. X. Wang, S. L. Chou, S. X. Dou, Z. M. M. Wang, *Energy Environ. Sci.* **2021**, 14, 3757.
- [57] K. Zhu, C. Wang, Z. Chi, F. Ke, Y. Yang, A. Wang, W. Wang, L. Miao, *Front. Energy Res.* **2019**, 7, 123.
- [58] a) C. Zhao, G. L. Xu, Z. Yu, L. Zhang, I. Hwang, Y. X. Mo, Y. Ren, L. Cheng, C. J. Sun, Y. Ren, X. Zuo, J. T. Li, S. G. Sun, K. Amine, T. Zhao, *Nat. Nanotechnol.* **2021**, 16, 166; b) Q. Shao, L. Xu, D. Guo, Y. Su, J. Chen, *J. Mater. Chem. A* **2020**, 8, 23772; c) B. Yu, F. Ma, D. J. Chen, K. Srinivas, X. J. Zhang, X. Q. Wang, B. Wang, W. L. Zhang, Z. G. Wang, W. D. He, Y. F. Chen, *J. Mater. Sci. Technol.* **2021**, 90, 37; d) J. Zhang, R. He, Q. Zhuang, X. J. Ma, C. Y. You, Q. Q. Hao, L. G. Li, S. Cheng, L. Lei, B. Deng, X. F. Li, H. Z. Lin, J. Wang, *Adv. Sci.* **2022**, 2202244; e) C. Zhou, M. Li, N. T. Hu, J. H. Yang, H. Li, J. W. Yan, P. Y. Lei, Y. P. Zhuang, S. W. Guo, *Adv. Funct. Mater.* **2020**, 16, 1907153; f) L. L. Zhang, F. Wan, H. M. Cao, L. L. Liu, Y. J. Wang, Z. Q. Niu, *Small* **2020**, 16, 1907153.
- [59] a) Y. Z. Song, W. L. Cai, L. Kong, J. S. Cai, Q. Zhang, J. Y. Sun, *Adv. Energy Mater.* **2020**, 10, 1901075; b) H. L. Ye, J. Y. Lee, *Small Methods* **2020**, 4, 1900864; c) L. Wang, W. X. Hua, X. Wan, Z. Feng, Z. H. Hu, H. Li, J. T. Niu, L. X. Wang, A. S. Wang, J. Y. Liu, X. Y. Lang, G. Wang, W. F. Li, Q. H. Yang, W. C. Wang, *Adv. Mater.* **2022**, 34, 2110279; d) H. L. Ye, Y. G. Li, *Infomat* **2021**, 4, e12291.
- [60] R. P. Fang, S. Y. Zhao, Z. H. Sun, W. Wang, H. M. Cheng, F. Li, *Adv. Mater.* **2017**, 29, 1606823.
- [61] J. M. Zheng, D. P. Lv, M. Gu, C. M. Wang, J. G. Zhang, J. Liu, J. Xiao, *J. Electrochem. Soc.* **2013**, 160, A2288.
- [62] a) Z. W. Seh, W. Y. Li, J. J. Cha, G. Y. Zheng, Y. Yang, M. T. McDowell, P. C. Hsu, Y. Cui, *Nat. Commun.* **2013**, 4, 1331; b) G. Babu, K. Ababtain, K. Y. S. Ng, L. M. R. Arava, *Sci. Rep.* **2015**, 5, 8763; c) Y. J. Li, J. M. Fan, M. S. Zheng, Q. F. Dong, *Energy Environ. Sci.* **2016**, 9, 1998; d) G. Zhou, H. Tian, Y. Jin, X. Tao, B. Liu, R. Zhang, Z. W. Seh, D. Zhuo, Y. Liu, J. Sun, J. Zhao, C. Zu, D. S. Wu, Q. Zhang, Y. Cui, *Proc. Natl. Acad. Sci. USA* **2017**, 114, 840; e) C. P. Yang, Y. G. Yao, S. M. He, H. Xie, E. Hitz, L. B. Hu, *Adv. Mater.* **2017**, 29, 1702714; f) Z. Z. Du, X. J. Chen, W. Hu, C. H. Chuang, S. Xie, A. J. Hu, W. S. Yan, X. H. Kong, X. J. Wu, H. X. Ji, L. J. Wan, *J. Am. Chem. Soc.* **2019**, 141, 3977; g) G. M. Zhou, S. Y. Wang, T. S. Wang, S. Z. Yang, B. Johannessen, H. Chen, C. W. Liu, Y. S. Ye, Y. C. Wu, Y. C. Peng, C. Liu, S. P. Jiang, Q. F. Zhang, Y. Cui, *Nano Lett.* **2020**, 20, 1252; h) Y. W. Sun, J. Q. Zhou, H. Q. Ji, J. Liu, T. Qian, C. L. Yan, *ACS Appl. Mater. Interfaces* **2019**, 11, 32008; i) Y. Gu, H. Y. Xu, X. G. Zhang, W. W. Wang, J. W. He, S. Tang, J. W. Yan, D. Y. Wu, M. S. Zheng, Q. F. Dong, B. W. Mao, *Angew. Chem., Int. Ed.* **2019**, 58, 3092; j) L. Zhang, J. Y. Bi, Z. K. Zhao, Y. X. Wang, D. B. Mu, B. R. Wu, *Electrochim. Acta* **2021**, 370, 137759; k) P. B. Zhai, T. S. Wang, H. N. Jiang, J. Y. Wan, Y. Wei, L. Wang, W. Liu, Q. Chen, W. W. Yang, Y. Cui, Y. J. Gong, *Adv. Mater.* **2021**, 33, 2006247.
- [63] a) X. L. Ji, L. F. Nazar, *J. Mater. Chem.* **2010**, 20, 9821; b) Y. X. Yin, S. Xin, Y. G. Guo, L. J. Wan, *Angew. Chem., Int. Ed.* **2013**, 52, 13186; c) L. F. Nazar, M. Cuisinier, Q. Pang, *MRS Bull.* **2014**, 39, 436.
- [64] K. A. See, M. Leskes, J. M. Griffin, S. Britto, P. D. Matthews, A. Emly, A. Van der Ven, D. S. Wright, A. J. Morris, C. P. Grey, R. Seshadri, *J. Am. Chem. Soc.* **2014**, 136, 16368.
- [65] a) Q. Wang, J. M. Zheng, E. Walter, H. L. Pan, D. P. Lv, P. J. Zuo, H. H. Chen, Z. D. Deng, B. Y. Liaw, X. Q. Yu, X. Q. Yang, J. G. Zhang, J. Liu, J. Xiao, *J. Electrochem. Soc.* **2015**, 162, A474; b) D. Zheng, X. R. Zhang, C. Li, M. E. McKinnon, R. G. Sadok, D. Y. Qu, X. Q. Yu, H. S. Lee, X. Q. Yang, D. Y. Qu, *J. Electrochem. Soc.* **2015**, 162, A203.
- [66] X. J. Gao, X. F. Yang, M. S. Li, Q. Sun, J. N. Liang, J. Luo, J. W. Wang, W. H. Li, J. W. Liang, Y. L. Liu, S. Z. Wang, Y. F. Hu, Q. F. Xiao, R. Y. Li, T. K. Sham, X. L. Sun, *Adv. Funct. Mater.* **2019**, 29, 1806724.
- [67] a) H. J. Peng, J. Q. Huang, M. Q. Zhao, Q. Zhang, X. B. Cheng, X. Y. Liu, W. Z. Qian, F. Wei, *Adv. Funct. Mater.* **2014**, 24, 2772; b) J. Ma, Z. Fang, Y. Yan, Z. Z. Yang, L. Gu, Y. S. Hu, H. Li, Z. X. Wang, X. J. Huang, *Adv. Energy Mater.* **2015**, 5, 1500046; c) Y. H. Xu, Y. Wen, Y. J. Zhu, K. Gaskell, K. A. Cychosz, B. Eichhorn, K. Xu, C. S. Wang, *Adv. Funct. Mater.* **2015**, 25, 4312; d) Z. Li, J. T. Zhang, Y. M. Chen, J. Li, X. W. Lou, *Nat. Commun.* **2015**, 6, 8850; e) S. Q. Chen, X. D. Huang, H. Liu, B. Sun, W. K. Yeoh, K. F. Li, J. Q. Zhang, G. X. Wang, *Adv. Energy Mater.* **2014**, 4, 1301761.
- [68] Z. Li, L. X. Yuan, Z. Q. Yi, Y. M. Sun, Y. Liu, Y. Jiang, Y. Shen, Y. Xin, Z. L. Zhang, Y. H. Huang, *Adv. Energy Mater.* **2014**, 4, 1301473.
- [69] L. Peng, Z. Wei, C. Wan, J. Li, Z. Chen, D. Zhu, D. Baumann, H. Liu, C. S. Allen, X. Xu, A. I. Kirkland, I. Shakir, Z. Almutairi, S. Tolbert, B. Dunn, Y. Huang, P. Sautet, X. Duan, *Nat. Catal.* **2020**, 3, 762.
- [70] X. Zhou, R. J. Meng, N. Zhong, S. F. Yin, G. Q. Ma, X. Liang, *Small Methods* **2021**, 5, 2100571.
- [71] M. L. Yu, S. Zhou, Z. Y. Wang, Y. W. Wang, N. Zhang, S. Wang, J. J. Zhao, J. S. Qiu, *Energy Storage Mater.* **2019**, 20, 98.
- [72] a) T. Z. Hou, W. T. Xu, X. Chen, H. J. Peng, J. Q. Huang, Q. Zhang, *Angew. Chem., Int. Ed.* **2017**, 56, 8178; b) J. M. Zheng, J. Tian, D. X. Wu, M. Gu, W. Xu, C. M. Wang, F. Gao, M. H. Engelhard, J. G. Zhang, J. Liu, J. Xiao, *Nano Lett.* **2014**, 14, 2345.
- [73] Z. Y. Han, S. Y. Zhao, J. W. Xiao, X. W. Zhong, J. Z. Sheng, W. Lv, Q. F. Zhang, G. M. Zhou, H. M. Cheng, *Adv. Mater.* **2021**, 33, 2105947.
- [74] H. L. Ye, J. G. Sun, S. L. Zhang, H. B. Lin, T. R. Zhang, Q. F. Yao, J. Y. Lee, *ACS Nano* **2019**, 13, 14208.
- [75] H. F. Xu, R. M. Hu, Y. Z. Zhang, H. B. Yan, Q. Zhu, J. X. Shang, S. B. Yang, B. Li, *Energy Storage Mater.* **2021**, 43, 212.
- [76] a) G. M. Liang, J. X. Wu, X. Y. Qin, M. Liu, Q. Li, Y. B. He, J. K. Kim, B. H. Li, F. Y. Kang, *ACS Appl. Mater. Interfaces* **2016**, 8, 23105; b) X. Chen, H. J. Peng, R. Zhang, T. Z. Hou, J. Q. Huang, B. Li, Q. Zhang, *ACS Energy Lett.* **2017**, 2, 795; c) Z. Li, J. T. Zhang, X. W. Lou, *Angew. Chem., Int. Ed.* **2015**, 54, 12886; d) J. Balach, J. Linnemann, T. Jaumann, L. Giebeler, *J. Mater. Chem. A* **2018**, 6, 23127; e) X. Liu, J. Q. Huang, Q. Zhang, L. Q. Mai, *Adv. Mater.* **2017**, 29, 25; f) A. Singh, V. Kalra, *J. Mater. Chem. A* **2019**, 7, 11613.
- [77] Y. C. Yan, T. Y. Lei, Y. Jiao, C. Y. Wu, J. Xiong, *Electrochim. Acta* **2018**, 264, 20.
- [78] H. J. Peng, Z. W. Zhang, J. Q. Huang, G. Zhang, J. Xie, W. T. Xu, J. L. Shi, X. Chen, X. B. Cheng, Q. Zhang, *Adv. Mater.* **2016**, 28, 9551.
- [79] L. Zhang, Z. X. Chen, N. C. Dongfang, M. X. Li, C. Z. Diao, Q. S. Wu, X. Chi, P. L. Jiang, Z. D. Zhao, L. Dong, R. C. Che, K. P. Loh, H. B. Lu, *Adv. Energy Mater.* **2018**, 8, 1802431.
- [80] L. Kong, X. Chen, B. Q. Li, H. J. Peng, J. Q. Huang, J. Xie, Q. Zhang, *Adv. Mater.* **2018**, 30, 1705219.

- [81] Y. Huang, L. Lin, C. Zhang, L. Liu, Y. Li, Z. Qiao, J. Lin, Q. Wei, L. Wang, Q. Xie, D. L. Peng, *Adv. Sci.* **2022**, *9*, 2106004.
- [82] Y. L. Pan, L. L. Gong, X. D. Cheng, Y. Zhou, Y. B. Fu, J. Feng, H. Ahmed, H. P. Zhang, *ACS Nano* **2020**, *14*, 5917.
- [83] Q. P. Wu, Z. G. Yao, X. J. Zhou, J. Xu, F. H. Cao, C. L. Li, *ACS Nano* **2020**, *14*, 3365.
- [84] a) Z. Yuan, H. J. Peng, T. Z. Hou, J. Q. Huang, C. M. Chen, D. W. Wang, X. B. Cheng, F. Wei, Q. Zhang, *Nano Lett.* **2016**, *16*, 519; b) G. Babu, N. Masurkar, H. Al Salem, L. M. R. Arave, *J. Am. Chem. Soc.* **2017**, *139*, 171; c) H. B. Lin, L. Q. Yang, X. Jiang, G. C. Li, T. R. Zhang, Q. F. Yao, G. W. Zheng, J. Y. Lee, *Energy Environ. Sci.* **2017**, *10*, 1476; d) Z. H. Sun, J. Q. Zhang, L. C. Yin, G. J. Hu, R. P. Fang, H. M. Cheng, F. Li, *Nat. Commun.* **2017**, *8*, 14627.
- [85] a) C. Q. Shang, G. R. Li, B. B. Wei, J. Y. Wang, R. Gao, Y. Tian, Q. Chen, Y. G. Zhang, L. L. Shui, G. F. Zhou, Y. F. Hu, Z. W. Chen, X. Wang, *Adv. Energy Mater.* **2021**, *11*, 2003020; b) Y. Zhong, X. H. Xia, F. Shi, J. Y. Zhan, J. P. Tu, H. J. Fan, *Adv. Sci.* **2016**, *3*, 1500286; c) Z. Y. Xing, G. R. Li, S. Sy, Z. W. Chen, *Nano Energy* **2018**, *54*, 1.
- [86] Y. S. Zhou, W. Guo, T. Li, *Ceram. Int.* **2019**, *45*, 21062.
- [87] L. L. Zhang, X. Chen, F. Wan, Z. Q. Niu, Y. J. Wang, Q. Zhang, J. Chen, *ACS Nano* **2018**, *12*, 9578.
- [88] S. F. Ng, M. Y. L. Lau, W. J. Ong, *Adv. Mater.* **2021**, *33*, 2008654.
- [89] Y. M. Shi, B. Zhang, *Chem. Soc. Rev.* **2016**, *45*, 1529.
- [90] S. Z. Huang, Y. V. Lim, X. M. Zhang, Y. Wang, Y. Zheng, D. Z. Kong, M. Ding, S. Y. A. Yang, H. Y. Yang, *Nano Energy* **2018**, *51*, 340.
- [91] Y. X. Yang, Y. R. Zhong, Q. W. Shi, Z. H. Wang, K. N. Sun, H. L. Wang, *Angew. Chem., Int. Ed.* **2018**, *57*, 15549.
- [92] J. F. Pang, J. M. Sun, M. Y. Zheng, H. Q. Li, Y. Wang, T. Zhang, *Appl. Catal. B: Environ.* **2019**, *254*, 510.
- [93] R. B. Levy, M. Boudart, *Science* **1973**, *181*, 547.
- [94] a) Y. L. Wu, X. R. Zhu, P. R. Li, T. Zhang, M. Li, J. Deng, Y. Huang, P. Ding, S. X. Wang, R. Zhang, J. Lu, G. Lu, Y. F. Li, Y. G. Li, *Nano Energy* **2019**, *59*, 636; b) F. Zhou, Z. Li, X. Luo, T. Wu, B. Jiang, L. L. Lu, H. B. Yao, M. Antonietti, S. H. Yu, *Nano Lett.* **2018**, *18*, 1035.
- [95] W. L. Li, K. Chen, Q. C. Xu, X. Y. Li, Q. Zhang, J. Weng, J. Xu, *Angew. Chem., Int. Ed.* **2021**, *60*, 21512.
- [96] a) Y. Cao, Y. Fang, X. Y. Lei, B. H. Tan, X. Hu, B. J. Liu, Q. L. Chen, *J. Hazard. Mater.* **2020**, *387*, 122021; b) Y. H. Zhou, K. Maleski, B. Anasori, J. O. Thostenson, Y. K. Pang, Y. Y. Feng, K. X. Zeng, C. B. Parker, S. Zauscher, Y. Gogotsi, J. T. Glass, C. Y. Cao, *ACS Nano* **2020**, *14*, 3576; c) T. Yun, H. Kim, A. Iqbal, Y. S. Cho, G. S. Lee, M. K. Kim, S. J. Kim, D. Kim, Y. Gogotsi, S. O. Kim, C. M. Koo, *Adv. Mater.* **2020**, *32*, 1906769; d) X. L. Zhang, J. F. Li, J. B. Li, L. Han, T. Lu, X. J. Zhang, G. Zhu, L. K. Pan, *Chem. Eng. J.* **2020**, *385*, 123394.
- [97] a) D. Guo, F. W. Ming, H. Su, Y. Q. Wu, W. Wahyudi, M. L. Li, M. N. Hedhili, G. Sheng, L. J. Li, H. N. Alshareef, Y. X. Li, Z. P. Lai, *Nano Energy* **2019**, *61*, 478; b) C. F. Zhang, L. F. Cui, S. Abdolhosseinzadeh, J. Heier, *Infomat* **2020**, *2*, 613; c) B. Li, H. F. Xu, Y. Ma, S. B. Yang, *Nanoscale Horiz.* **2019**, *4*, 77.
- [98] a) X. B. A. Liu, X. F. Shao, F. Li, M. W. Zhao, *Appl. Surf. Sci.* **2018**, *455*, 522; b) H. Lin, D. D. Yang, N. Lou, S. G. Zhu, H. Z. Li, *Ceram. Int.* **2019**, *45*, 1588; c) V. Shukla, N. K. Jena, S. R. Naqvi, W. Luo, R. Ahuja, *Nano Energy* **2019**, *58*, 877.
- [99] Z. Li, B. Y. Guan, J. T. Zhang, X. W. Lou, *Joule* **2017**, *1*, 576.
- [100] T. H. Zhou, W. Lv, J. Li, G. M. Zhou, Y. Zhao, S. X. Fan, B. L. Liu, B. H. Li, F. Y. Kang, Q. H. Yang, *Energy Environ. Sci.* **2017**, *10*, 1694.
- [101] J. L. Yang, S. X. Zhao, Y. M. Lu, X. T. Zeng, W. Lv, G. Z. Cao, *Nano Energy* **2020**, *68*, 104356.
- [102] Z. Shi, M. Li, J. Sun, Z. Chen, *Adv. Energy Mater.* **2021**, *11*, 2100332.
- [103] W. Cai, Y. Song, Y. Fang, W. Wang, S. Yu, H. Ao, Y. Zhu, Y. Qian, *Nano Res.* **2020**, *13*, 3315.
- [104] C. L. Dai, J. M. Lim, M. Q. Wang, L. Y. Hu, Y. M. Chen, Z. Y. Chen, H. Chen, S. J. Bao, B. L. Shen, Y. Li, G. Henkelman, M. W. Xu, *Adv. Funct. Mater.* **2018**, *28*, 1704443.
- [105] Y. P. Liu, S. Y. Ma, L. F. Liu, J. L. Koch, M. Rosebrock, T. R. Li, F. Bettels, T. He, H. Pfnur, N. C. Bigall, A. Feldhoff, F. Ding, L. Zhang, *Adv. Funct. Mater.* **2020**, *30*, 2002462.
- [106] Z. H. Shen, M. Q. Cao, Z. L. Zhang, J. Pu, C. L. Zhong, J. C. Li, H. X. Ma, F. J. Li, J. Zhu, F. Pan, H. G. Zhang, *Adv. Funct. Mater.* **2020**, *30*, 1906661.
- [107] H. Zhang, Y. Zhou, C. G. Li, S. L. Chen, L. Liu, S. W. Liu, H. M. Yao, H. Q. Hou, *Carbon* **2015**, *95*, 388.
- [108] C. G. Hu, L. M. Dai, *Adv. Mater.* **2019**, *31*, 1804672.
- [109] a) J. Y. Wang, G. R. Li, D. Luo, Y. G. Zhang, Y. Zhao, G. F. Zhou, L. L. Shui, X. Wang, Z. W. Chen, *Adv. Energy Mater.* **2020**, *10*, 2002076; b) D. Q. He, J. T. Meng, X. Y. Chen, Y. Q. Liao, Z. X. Cheng, L. X. Yuan, Z. Li, Y. H. Huang, *Adv. Funct. Mater.* **2021**, *31*, 2001201; c) G. H. Liu, D. Luo, R. Gao, Y. F. Hu, A. P. Yu, Z. W. Chen, *Small* **2020**, *16*, 2001089.
- [110] D. Luo, G. R. Li, Y. P. Deng, Z. Zhang, J. D. Li, R. L. Liang, M. Li, Y. Jiang, W. W. Zhang, Y. S. Liu, W. Lei, A. P. Yu, Z. W. Chen, *Adv. Energy Mater.* **2019**, *9*, 1900228.
- [111] M. Zhao, H. J. Peng, Z. W. Zhang, B. Q. Li, X. Chen, J. Xie, X. Chen, J. Y. Wei, Q. Zhang, J. Q. Huang, *Angew. Chem., Int. Ed.* **2019**, *58*, 3779.
- [112] C. Zhu, S. Fu, Q. Shi, D. Du, Y. Lin, *Angew. Chem., Int. Ed.* **2017**, *56*, 13944.
- [113] Z. Luo, X. Qiu, C. Liu, S. Li, C. Wang, G. Zou, H. Hou, X. Ji, *Nano Energy* **2021**, *79*, 105507.
- [114] C. P. Yang, Y. X. Yin, S. F. Zhang, N. W. Li, Y. G. Guo, *Nat. Commun.* **2015**, *6*, 8058.
- [115] Q. B. Yun, Y. B. He, W. Lv, Y. Zhao, B. H. Li, F. Y. Kang, Q. H. Yang, *Adv. Mater.* **2016**, *28*, 6932.
- [116] L. H. Pan, Z. F. Luo, Y. T. Zhang, W. L. Chen, Z. H. Zhao, Y. Y. Li, J. Wan, D. D. Yu, H. Y. He, D. Y. Wang, *ACS Appl. Mater. Interfaces* **2019**, *11*, 44383.
- [117] Y. J. Fang, S. L. Zhang, Z. P. Wu, D. Y. Luan, X. W. Lou, *Sci. Adv.* **2021**, *7*, eabg63626.
- [118] Z. Wang, Z. Yu, B. L. Wang, Z. W. Guo, N. Wang, Y. G. Wang, Y. Y. Xia, *J. Mater. Chem. A* **2019**, *7*, 22930.
- [119] J. Zhao, G. M. Zhou, K. Yan, J. Xie, Y. Z. Li, L. Liao, Y. Jin, K. Liu, P. C. Hsu, J. Y. Wang, H. M. Cheng, Y. Cui, *Nat. Nanotechnol.* **2017**, *12*, 993.
- [120] T. Zhou, J. D. Shen, Z. S. Wang, J. Liu, R. Z. Hu, L. Z. Ouyang, Y. Z. Feng, H. Liu, Y. Yu, M. Zhu, *Adv. Funct. Mater.* **2020**, *30*, 1909159.
- [121] X. Y. Yue, J. Bao, S. Y. Yang, R. J. Luo, Z. Shadike, X. Q. Yang, Y. N. Zhou, *Nano Energy* **2020**, *71*, 104614.
- [122] C. C. Zhao, X. Yao, H. Yang, X. X. Jiao, L. N. Wang, *Compos. Commun.* **2021**, *26*, 100789.
- [123] L. Yu, Q. Su, B. Li, L. Huang, G. Du, S. Ding, W. Zhao, M. Zhang, B. Xu, *Chem. Eng. J.* **2022**, *429*, 132479.
- [124] X. R. Chen, B. Q. Li, C. Zhu, R. Zhang, X. B. Cheng, J. Q. Huang, Q. Zhang, *Adv. Energy Mater.* **2019**, *9*, 1901932.
- [125] F. H. Guo, C. Wu, H. Chen, F. P. Zhong, X. P. Ai, H. X. Yang, J. F. Qian, *Energy Storage Mater.* **2020**, *24*, 635.
- [126] a) R. Zhang, S. W. Wen, N. Wang, K. Q. Qin, E. Z. Liu, C. S. Shi, N. Q. Zhao, *Adv. Energy Mater.* **2018**, *8*, 1800914; b) Q. Wang, C. K. Yang, J. J. Yang, K. Wu, L. Y. Qi, H. Tang, Z. Y. Zhang, W. Liu, H. H. Zhou, *Energy Storage Mater.* **2018**, *15*, 249.
- [127] a) Z. Wang, H. Shi, S. T. Yang, Z. J. Cai, H. Q. Lu, L. T. Jia, M. Z. Hu, H. He, K. B. Zhou, *J. Alloy Compd.* **2021**, *888*, 161553; b) X. J. Shen, G. Y. Zhao, X. B. Yu, H. H. Huang, M. Wang, N. Q. Zhang, *J. Mater. Chem. A* **2021**, *9*, 21695; c) C. Yu, Y. Du, R. H. He, Y. Ma, Z. H. Liu, X. Y. Li, W. Luo, L. Zhou, L. Q. Mai, *ACS Appl. Energy Mater.* **2021**, *4*, 3905.

- [128] Y. L. Lin, S. Huang, L. Zhong, S. J. Wang, D. M. Han, S. Ren, M. Xiao, Y. Z. Meng, *Energy Storage Mater.* **2021**, *34*, 128.
- [129] D. Zhou, D. Shanmukaraj, A. Tkacheva, M. Armand, G. X. Wang, *Chem* **2019**, *5*, 2326.
- [130] L. Wang, Y. Ye, N. Chen, Y. Huang, L. Li, F. Wu, R. Chen, *Adv. Funct. Mater.* **2018**, *28*, 1800919.
- [131] a) M. Hagen, D. Hanselmann, K. Ahlbrecht, R. Maca, D. Gerber, J. Tubke, *Adv. Energy Mater.* **2015**, *5*, 1401986; b) L. Carbone, J. Peng, M. Agostini, M. Gobet, M. Devany, B. Scrosati, S. Greenbaum, J. Hassoun, *ChemElectroChem* **2017**, *4*, 209.
- [132] a) A. Jozwiuk, B. B. Berkes, T. Weiss, H. Sommer, J. Janek, T. Brezesinski, *Energy Environ. Sci.* **2016**, *9*, 2603; b) Y. Mikhaylik, I. Kovalev, R. Schock, K. Kumaresan, J. Xu, J. Affinito, *ECS Trans.* **2010**, *25*, 23.
- [133] a) H.-S. Ryu, H.-J. Ahn, K.-W. Kim, J.-H. Ahn, K.-K. Cho, T.-H. Nam, J.-U. Kim, G.-B. Cho, *J. Power Sources* **2006**, *163*, 201; b) J.-W. Choi, J.-K. Kim, G. Cheruvally, J.-H. Ahn, H.-J. Ahn, K.-W. Kim, *Electrochim. Acta* **2007**, *52*, 2075; c) S. Kim, Y. Jung, H. S. Lim, *Electrochim. Acta* **2004**, *50*, 889.
- [134] N. Azimi, W. Weng, C. Takoudis, Z. C. Zhang, *Electrochem. Commun.* **2013**, *37*, 96.
- [135] S. R. Chen, Z. X. Yu, M. L. Gordin, R. Yi, J. X. Song, D. H. Wang, *ACS Appl. Mater. Interfaces* **2017**, *9*, 6959.
- [136] S. Zhang, K. Ueno, K. Dokko, M. Watanabe, *Adv. Energy Mater.* **2015**, *5*, 1500117.
- [137] a) J. Gao, M. A. Lowe, Y. Kiya, H. D. Abruna, *J. Phys. Chem. C* **2011**, *115*, 25132; b) T. Yim, M. S. Park, J. S. Yu, K. J. Kim, K. Y. Im, J. H. Kim, G. Jeong, Y. N. Jo, S. G. Woo, K. S. Kang, I. Lee, Y. J. Kim, *Electrochim. Acta* **2013**, *107*, 454.
- [138] L. Shi, Y. G. Liu, W. K. Wang, A. B. Wang, Z. Q. Jin, F. Wu, Y. S. Yang, *J. Alloy Compd.* **2017**, *723*, 974.
- [139] E. Markevich, G. Salitra, D. Aurbach, *ACS Energy Lett.* **2017**, *2*, 1337.
- [140] E. Markevich, G. Salitra, A. Rosenman, Y. Talyosef, F. Chesneau, D. Aurbach, *Electrochem. Commun.* **2015**, *60*, 42.
- [141] H. Shin, M. Baek, A. Gupta, K. Char, A. Manthiram, J. W. Choi, *Adv. Energy Mater.* **2020**, *10*, 2001456.
- [142] H. Kim, F. X. Wu, J. T. Lee, N. Nitta, H. T. Lin, M. Oschatz, W. I. Cho, S. Kaskel, O. Borodin, G. Yushin, *Adv. Energy Mater.* **2015**, *5*, 1401792.
- [143] G. C. Yan, X. H. Li, Z. X. Wang, H. J. Guo, W. J. Peng, Q. Y. Hu, *J. Solid State Electr.* **2016**, *20*, 507.
- [144] a) F. X. Wu, J. T. Lee, N. Nitta, H. Kim, O. Borodin, G. Yushin, *Adv. Mater.* **2015**, *27*, 101; b) F. Wu, J. Qian, R. J. Chen, J. Lu, L. Li, H. M. Wu, J. Z. Chen, T. Zhao, Y. S. Ye, K. Amine, *ACS Appl. Mater. Interfaces* **2014**, *6*, 15542.
- [145] D. Aurbach, E. Pollak, R. Elazari, G. Salitra, C. S. Kelley, J. Affinito, *J. Electrochem. Soc.* **2009**, *156*, A694.
- [146] S. S. Zhang, *J. Power Sources* **2016**, *322*, 99.
- [147] S. Kim, Y. M. Kwon, K. Y. Cho, S. Yoon, *Electrochim. Acta* **2021**, *391*, 138927.
- [148] W. D. Zeng, M. M. C. Cheng, S. K. Y. Ng, *Electrochim. Acta* **2019**, *319*, 511.
- [149] Z. Lin, Z. C. Liu, W. J. Fu, N. J. Dudney, C. D. Liang, *Adv. Funct. Mater.* **2013**, *23*, 1064.
- [150] S. L. Li, W. F. Zhang, J. F. Zheng, M. Y. Lv, H. Y. Song, L. Du, *Adv. Energy Mater.* **2021**, *11*, 2000779.
- [151] a) Y. S. Su, A. Manthiram, *Nat. Commun.* **2012**, *3*, 1166; b) P. Zeng, L. W. Huang, X. L. Zhang, R. X. Zhang, L. Wu, Y. G. Chen, *Chem. Eng. J.* **2018**, *349*, 327; c) B. Moorthy, S. Kwon, J. H. Kim, P. Ragupathy, H. M. Lee, D. K. Kim, *Nanoscale Horiz.* **2019**, *4*, 214; d) T. Y. Lei, W. Chen, W. Q. Lv, J. W. Huang, J. Zhu, J. W. Chu, C. Y. Yan, C. Y. Wu, Y. C. Yan, W. D. He, J. Xiong, Y. R. Li, C. L. Yan, J. B. Goodenough, X. F. Duan, *Joule* **2018**, *2*, 2091; e) T. Z. Zhuang, J. Q. Huang, H. J. Peng, L. Y. He, X. B. Cheng, C. M. Chen, Q. Zhang, *Small* **2016**, *12*, 381; f) R. Xu, Y. Z. Sun, Y. F. Wang, J. Q. Huang, Q. Zhang, *Chin. Chem. Lett.* **2017**, *28*, 2235.
- [152] Z. B. Cheng, H. Pan, J. Q. Chen, X. P. Meng, R. H. Wang, *Adv. Energy Mater.* **2019**, *9*, 1901609.
- [153] C. L. Song, G. H. Li, Y. Yang, X. J. Hong, S. Huang, Q. F. Zheng, L. P. Si, M. Zhang, Y. P. Cai, *Chem. Eng. J.* **2020**, *381*, 122701.
- [154] X. M. Yu, W. X. Chen, J. J. Cai, X. Lu, Z. P. Sun, *J. Colloid Interface Sci.* **2022**, *610*, 407.
- [155] J. Zhu, J. Roscow, S. Chandrasekaran, L. Deng, P. Zhang, T. He, K. Wang, L. Huang, *ChemSusChem* **2020**, *13*, 1275.
- [156] H. Pan, Y.-S. Hu, L. Chen, *Energy Environ. Sci.* **2013**, *6*, 2338.
- [157] J. Y. Hwang, S. T. Myung, Y. K. Sun, *Chem. Soc. Rev.* **2017**, *46*, 3529.
- [158] X. W. Yu, A. Manthiram, *ChemElectroChem* **2014**, *1*, 1275.
- [159] C. W. Park, J. H. Ahn, H. S. Ryu, K. W. Kim, H. J. Ahn, *Electrochem. Solid State* **2006**, *9*, A123.
- [160] Y. X. Wang, J. P. Yang, W. H. Lai, S. L. Chou, Q. F. Gu, H. K. Liu, D. Y. Zhao, S. X. Dou, *J. Am. Chem. Soc.* **2016**, *138*, 16576.
- [161] C. Ye, H. Jin, J. Shan, Y. Jiao, H. Li, Q. Gu, K. Davey, H. Wang, S. Z. Qiao, *Nat. Commun.* **2021**, *12*, 7195.
- [162] B. W. Zhang, T. Sheng, Y. X. Wang, S. L. Chou, K. Davey, S. X. Dou, S. Z. Qiao, *Angew. Chem., Int. Ed.* **2019**, *58*, 1484.
- [163] Y. P. Liu, S. Y. Ma, M. Rosebrock, P. Rusch, Y. Barnscheidt, C. Q. Wu, P. F. Nan, F. Bettels, Z. H. Lin, T. R. Li, B. H. Ge, N. C. Bigall, H. Pfnur, F. Ding, C. F. Zhang, L. Zhang, *Adv. Sci.* **2022**, *9*, 2105544.
- [164] W. H. Lai, H. Wang, L. R. Zheng, Q. Jiang, Z. C. Yan, L. Wang, H. Yoshikawa, D. Matsumura, Q. Sun, Y. X. Wang, Q. F. Gu, J. Z. Wang, H. K. Liu, S. L. Chou, S. X. Dou, *Angew. Chem., Int. Ed.* **2020**, *59*, 22171.
- [165] R. Jayan, M. M. Islam, *J. Phys. Chem. C* **2021**, *125*, 4458.
- [166] Q. R. Ma, W. Zhong, G. Y. Du, Y. R. Qi, S. J. Bao, M. W. Xu, C. M. Li, *ACS Appl. Mater. Interfaces* **2021**, *13*, 11852.
- [167] A. Kumar, A. Ghosh, A. Ghosh, A. Ahuja, A. Sengupta, M. Forsyth, D. R. MacFarlane, S. Mitra, *Energy Storage Mater.* **2021**, *42*, 608.
- [168] M. K. Aslam, I. D. Seymour, N. Katyal, S. Li, T. T. Yang, S. J. Bao, G. Henkelman, M. W. Xu, *Nat. Commun.* **2020**, *11*, 5242.
- [169] H. W. Liu, W. Pei, W. H. Lai, Z. C. Yan, H. L. Yang, Y. J. Lei, Y. X. Wang, Q. F. Gu, S. Zhou, S. L. Chou, H. K. Liu, S. X. Dou, *ACS Nano* **2020**, *14*, 7259.
- [170] X. F. Zhou, Z. X. Yu, Y. Yao, Y. Jiang, X. H. Rui, J. Q. Liu, Y. Yu, *Adv. Mater.* **2022**, *34*, 2200479.
- [171] a) Q. R. Ma, G. Y. Du, W. Zhong, W. Y. Du, S. J. Bao, M. W. Xu, C. M. Li, *J. Colloid Interface Sci.* **2020**, *578*, 710; b) R. X. Zhang, A. M. Esposito, E. S. Thornburg, X. Y. Chen, X. Y. Zhang, M. A. Philip, A. Magana, A. A. Gewirth, *ACS Appl. Mater. Interfaces* **2020**, *12*, 29285.
- [172] G. H. Qin, Y. T. Liu, P. Y. Han, S. X. Cao, X. Y. Guo, Z. Y. Guo, *Chem. Eng. J.* **2020**, *396*, 125295.
- [173] D. J. Li, B. B. Gong, X. L. Cheng, F. X. Ling, L. G. Zhao, Y. Yao, M. Z. Ma, Y. Jiang, Y. Shao, X. H. Rui, W. H. Zhang, H. Zheng, J. B. Wang, C. Ma, Q. B. Zhang, Y. Yu, *ACS Nano* **2021**, *15*, 20607.
- [174] A. Y. S. Eng, Y. Wang, D. T. Nguyen, S. Y. Tee, C. Y. J. Lim, X. Y. Tan, M. F. Ng, J. W. Xu, Z. W. Seh, *Nano Lett.* **2021**, *21*, 5401.
- [175] B. Lee, E. Paek, D. Mitlin, S. W. Lee, *Chem. Rev.* **2019**, *119*, 5416.
- [176] R. Dugas, A. Ponrouch, G. Gachot, R. David, M. R. Palacin, J. M. Tarascon, *J. Electrochem. Soc.* **2016**, *163*, A2333.
- [177] A. Rudola, D. Aurbach, P. Balaya, *Electrochem. Commun.* **2014**, *46*, 56.
- [178] Y. S. Hong, N. Li, H. S. Chen, P. Wang, W. L. Song, D. N. Fang, *Energy Storage Mater.* **2018**, *11*, 118.
- [179] Z. P. Li, K. J. Zhu, P. Liu, L. F. Jiao, *Adv. Energy Mater.* **2021**, *12*, 2100359.
- [180] a) S. Higashi, S. W. Lee, J. S. Lee, K. Takechi, Y. Cui, *Nat. Commun.* **2016**, *7*, 11801; b) M. Rosso, C. Brissot, A. Teysot, M. Dolle,

- L. Sannier, J. M. Tarascon, R. Bouchet, S. Lascaud, *Electrochim. Acta* **2006**, *51*, 5334.
- [181] a) I. W. Seong, C. H. Hong, B. K. Kim, W. Y. Yoon, *J. Power Sources* **2008**, *178*, 769; b) C. Brissot, M. Rosso, J. N. Chazalviel, P. Baudry, S. Lascaud, *Electrochim. Acta* **1998**, *43*, 1569.
- [182] S. Y. Wei, S. Choudhury, J. Xu, P. Nath, Z. Y. Tu, L. A. Archer, *Adv. Mater.* **2017**, *29*, 1605512.
- [183] Y. Yui, M. Hayashi, J. Nakamura, *Sci. Rep.* **2016**, *6*, 22406.
- [184] S. Choudhury, S. Y. Wei, Y. Ozhobes, D. Gunceler, M. J. Zachman, Z. Y. Tu, J. H. Shin, P. Nath, A. Agrawal, L. F. Kourkoutis, T. A. Arias, L. A. Archer, *Nat. Commun.* **2017**, *8*, 898.
- [185] W. Luo, C. F. Lin, O. Zhao, M. Noked, Y. Zhang, G. W. Rubloff, L. B. Hu, *Adv. Energy Mater.* **2017**, *7*, 1601526.
- [186] a) W. Liu, D. C. Lin, A. Pei, Y. Cui, *J. Am. Chem. Soc.* **2016**, *138*, 15443; b) W. Xu, J. L. Wang, F. Ding, X. L. Chen, E. Nasybutin, Y. H. Zhang, J. G. Zhang, *Energy Environ. Sci.* **2014**, *7*, 513; c) K. Nishikawa, T. Mori, T. Nishida, Y. Fukunaka, M. Rosso, *J. Electroanal. Chem.* **2011**, *661*, 84; d) H. Sano, H. Sakaebe, H. Senoh, H. Matsumoto, *J. Electrochem. Soc.* **2014**, *161*, A1236.
- [187] S. Liu, S. Tang, X. Y. Zhang, A. X. Wang, Q. H. Yang, J. Y. Luo, *Nano Lett.* **2017**, *17*, 5862.
- [188] a) Y. Y. Lu, Q. Zhang, M. Han, J. Chen, *Chem. Commun.* **2017**, *53*, 12910; b) Y. L. Xu, A. S. Menon, P. Harks, D. C. Hermes, L. A. Haverkate, S. Unnikrishnan, F. M. Mulder, *Energy Storage Mater.* **2018**, *12*, 69.
- [189] W. Liu, P. Y. Li, W. W. Wang, D. Zhu, Y. G. Chen, S. L. Pen, E. Paek, D. Mitlin, *ACS Nano* **2018**, *12*, 12255.
- [190] a) J. L. Liang, W. W. Wu, L. Xu, X. H. Wu, *Carbon* **2021**, *176*, 219; b) N. Mubarak, F. Rehman, J. X. Wu, M. Ihsan-Ul-Haq, Y. Li, Y. H. Zhao, X. Shen, Z. T. Luo, B. L. Huang, J. K. Kim, *Nano Energy* **2021**, *86*, 106132.
- [191] a) Y. Y. Xie, J. X. Hu, Z. X. Han, T. S. Wang, J. Q. Zheng, L. Gan, Y. Q. Lai, Z. A. Zhang, *Energy Storage Mater.* **2020**, *30*, 1; b) H. Wang, T. T. Jiang, B. Y. Wang, L. M. Zhang, D. Z. Kong, T. T. Xu, J. H. Zhang, Z. F. Zhang, X. J. Li, Y. Wang, *J. Power Sources* **2021**, *507*, 230294; c) Z. W. Sun, H. C. Jin, Y. D. Ye, H. Y. Xie, W. S. Jia, S. Jin, H. X. Ji, *ACS Appl. Energy Mater.* **2021**, *4*, 2724; d) C. Lu, Z. X. Gao, B. Z. Liu, Z. X. Shi, Y. Y. Yi, W. Zhao, W. Y. Guo, Z. F. Liu, J. Y. Sun, *Adv. Funct. Mater.* **2021**, *31*, 2101233.
- [192] T. Z. Yang, T. Qian, Y. W. Sun, J. Zhong, F. Rosei, C. L. Yan, *Nano Lett.* **2019**, *19*, 7827.
- [193] Y. J. Li, P. Xu, J. R. Mou, S. F. Xue, S. M. Huang, J. H. Hu, Q. F. Dong, C. H. Yang, M. L. Liu, *Small Methods* **2021**, *5*, 2100833.
- [194] a) S. Tang, Y. Y. Zhang, X. G. Zhang, J. T. Li, X. Y. Wang, J. W. Yan, D. Y. Wu, M. S. Zheng, Q. F. Dong, B. W. Mao, *Adv. Mater.* **2019**, *31*, 1807495; b) J. A. Gu, Q. Zhu, Y. Z. Shi, H. Chen, D. Zhang, Z. G. Du, S. B. Yang, *ACS Nano* **2020**, *14*, 891.
- [195] Z. D. Wang, K. Lu, F. Xia, O. Dahunsi, S. Y. Gao, B. M. Li, R. Wang, S. T. Lu, W. Qin, Y. W. Cheng, X. H. Wu, *J. Mater. Chem. A* **2021**, *9*, 6123.
- [196] S. Y. Li, Q. L. Liu, J. J. Zhou, T. Pan, L. N. Gao, W. D. Zhang, L. Fan, Y. Y. Lu, *Adv. Funct. Mater.* **2019**, *29*, 1808847.
- [197] Y. Xu, E. Matios, J. M. Luo, T. Li, X. Lu, S. H. Jiang, Q. Yue, W. Y. Li, Y. J. Kang, *Nano Lett.* **2021**, *21*, 816.
- [198] Y. Z. Fang, Y. Zhang, K. Zhu, R. Q. Lian, Y. Gao, J. L. Yin, K. Ye, K. Cheng, J. Yan, G. L. Wang, Y. J. Wei, D. X. Cao, *ACS Nano* **2019**, *13*, 14319.
- [199] H. Ryu, T. Kim, K. Kim, J. H. Ahn, T. Nam, G. Wang, H. J. Ahn, *J. Power Sources* **2011**, *196*, 5186.
- [200] H. W. Liu, W. H. Lai, Y. J. Lei, H. L. Yang, N. N. Wang, S. L. Chou, H. K. Liu, S. X. Dou, Y. X. Wang, *Adv. Energy Mater.* **2022**, *12*, 2103304.
- [201] a) S. Wenzel, H. Metelmann, C. Raiss, A. K. Durr, J. Janek, P. Adelhelm, *J. Power Sources* **2013**, *243*, 758; b) R. Carter, L. Oakes, A. Douglas, N. Muralidharan, A. P. Cohn, C. L. Pint, *Nano Lett.* **2017**, *17*, 1863; c) Y. M. Chen, W. F. Liang, S. Li, F. Zou, S. M. Bhaway, Z. Qiang, M. Gao, B. D. Vogt, Y. Zhu, *J. Mater. Chem. A* **2016**, *4*, 12471.
- [202] D.-J. Lee, J.-W. Park, I. Hasa, Y.-K. Sun, B. Scrosati, J. Hassoun, *J. Mater. Chem. A* **2013**, *1*, 5256.
- [203] J. H. Zhou, Y. Yang, Y. C. Zhang, S. K. Duan, X. Zhou, W. Sun, S. M. Xu, *Angew. Chem., Int. Ed.* **2021**, *60*, 10129.
- [204] H. Y. Che, S. L. Chen, Y. Y. Xie, H. Wang, K. Amine, X. Z. Liao, Z. F. Ma, *Energy Environ. Sci.* **2017**, *10*, 1075.
- [205] A. Ponrouch, E. Marchante, M. Courty, J. M. Tarascon, M. R. Palacin, *Energy Environ. Sci.* **2012**, *5*, 8572.
- [206] P. Thomas, J. Ghanbaja, D. Billaud, *Electrochim. Acta* **1999**, *45*, 423.
- [207] H. Li, M. Zhao, B. Jin, Z. Wen, H. K. Liu, Q. Jiang, *Small* **2020**, *16*, 1907464.
- [208] T. F. Liu, X. K. Yang, J. W. Nai, Y. Wang, Y. J. Liu, C. T. Liu, X. Y. Tao, *Chem. Eng. J.* **2021**, *409*, 127943.
- [209] Q. B. Guo, S. Sun, K. I. Kim, H. S. Zhang, X. J. Liu, C. L. Yan, H. Xia, *Carbon Energy* **2021**, *3*, 440.
- [210] Y. Z. Wang, D. Zhou, V. Palomares, D. Shanmukaraj, B. Sun, X. Tang, C. S. Wang, M. Armand, T. Rojo, G. X. Wang, *Energy Environ. Sci.* **2020**, *13*, 3848.
- [211] A. Ghosh, S. Shukla, M. Monisha, A. Kumar, B. Lochab, S. Mitra, *ACS Energy Lett.* **2017**, *2*, 2479.
- [212] M. Kohl, F. Borrmann, H. Althues, S. Kaskel, *Adv. Energy Mater.* **2016**, *6*, 1502185.
- [213] Y. X. Ren, H. R. Jiang, T. S. Zhao, L. Zeng, C. Xiong, *J. Power Sources* **2018**, *396*, 304.
- [214] X. F. Xu, D. Zhou, X. Y. Qin, K. Lin, F. Y. Kang, B. H. Li, D. Shanmukaraj, T. Rojo, M. Armand, G. X. Wang, *Nat. Commun.* **2018**, *9*, 3870.
- [215] a) S. P. Zhang, Y. Yao, Y. Yu, *ACS Energy Lett.* **2021**, *6*, 529; b) T. X. Li, J. Xu, C. Y. Wang, W. J. Wu, D. W. Su, G. X. Wang, *J. Alloy. Compd.* **2019**, *792*, 797.
- [216] Y. X. Wang, B. Zhang, W. Lai, Y. Xu, S. L. Chou, H. K. Liu, S. X. Dou, *Adv. Energy Mater.* **2017**, *7*, 1602829.
- [217] C. Dong, H. Zhou, B. Jin, W. Gao, X. Lang, J. Li, Q. Jiang, *J. Mater. Chem. A* **2021**, *9*, 3451.
- [218] C. Z. Wang, K. H. Wu, J. Q. Cui, X. L. Fang, J. Li, N. F. Zheng, *Small* **2022**, *2106983*.
- [219] a) X. Lu, G. Li, J. Y. Kim, D. Mei, J. P. Lemmon, V. L. Sprenkle, J. Liu, *Nat. Commun.* **2014**, *5*, 4578; b) A. Eftekhari, Z. L. Jian, X. L. Ji, *ACS Appl. Mater. Interfaces* **2017**, *9*, 4404; c) J. Y. Hwang, H. M. Kim, C. S. Yoon, Y. K. Sun, *ACS Energy Lett.* **2018**, *3*, 540.
- [220] P. C. Liu, Y. X. Wang, Q. L. Gu, J. Nanda, J. Watt, D. Mitlin, *Adv. Mater.* **2020**, *32*, 1906735.
- [221] L. Qin, Y. Lei, H. W. Wang, J. H. Dong, Y. Y. Wu, D. Y. Zhai, F. Y. Kang, Y. Tao, Q. H. Yang, *Adv. Energy Mater.* **2019**, *9*, 1901427.
- [222] Y. Q. Li, L. Y. Zhang, S. F. Liu, X. L. Wang, D. Xie, X. H. Xia, C. D. Gu, J. P. Tu, *Nano Energy* **2019**, *62*, 367.
- [223] X. Tang, D. Zhou, P. Li, X. Guo, B. Sun, H. Liu, K. Yan, Y. Gogotsi, G. X. Wang, *Adv. Mater.* **2020**, *32*, 1906739.
- [224] Y. Yang, H. Y. Yang, X. R. Wang, Y. Bai, C. Wu, *J. Energy Chem.* **2022**, *64*, 144.
- [225] a) A. Ponrouch, M. R. Palacin, *Curr. Opin. Electrochem.* **2018**, *9*, 1; b) A. Ponrouch, C. Frontera, F. Barde, M. R. Palacin, *Nat. Mater.* **2016**, *15*, 169.
- [226] D. Wang, X. W. Gao, Y. H. Chen, L. Y. Jin, C. Kuss, P. G. Bruce, *Nat. Mater.* **2018**, *17*, 16.
- [227] a) Z. Y. Li, O. Fuhr, M. Fichtner, Z. Zhao-Karger, *Energy Environ. Sci.* **2019**, *12*, 3496; b) K. V. Nielson, J. Luo, T. L. Liu, *Batteries Supercaps* **2020**, *3*, 766; c) A. Shyamsunder, L. E. Blanc, A. Assoud, L. F. Nazar, *ACS Energy Lett.* **2019**, *4*, 2271.
- [228] a) M. Salama, Rosy, R. Attias, R. Yemini, Y. Gofer, D. Aurbach, M. Noked, *ACS Energy Lett.* **2019**, *4*, 436; b) L. Kong, C. Yan,

- J.-Q. Huang, M.-Q. Zhao, M.-M. Titirici, R. Xiang, Q. Zhang, *Energy Environ. Mater.* **2018**, *1*, 100.
- [229] Y. Xu, Y. F. Ye, S. Y. Zhao, J. Feng, J. Li, H. Chen, A. K. Yang, F. F. Shi, L. J. Jia, Y. Wu, X. Y. Yu, P. A. Glans-Suzuki, Y. Cui, J. H. Guo, Y. G. Zhang, *Nano Lett.* **2019**, *19*, 2928.
- [230] a) K. Itaoka, I. T. Kim, K. Yamabuki, N. Yoshimoto, H. Tsutsumi, *J. Power Sources* **2015**, *297*, 323; b) H. P. Du, Z. H. Zhang, J. J. He, Z. L. Cui, J. C. Chai, J. Ma, Z. Yang, C. S. Huang, G. L. Cui, *Small* **2017**, *13*, 1702277; c) X. J. Zhou, J. Tian, J. L. Hu, C. L. Li, *Adv. Mater.* **2018**, *30*, 1704166.
- [231] N. Jayaprakash, S. K. Das, L. A. Archer, *Chem. Commun.* **2011**, *47*, 12610.
- [232] a) S. Licht, D. Peramunage, *J. Electrochem. Soc.* **1993**, *140*, L4; b) D. Peramunage, R. Dillon, S. Licht, *J. Power Sources* **1993**, *45*, 311.
- [233] a) H. L. Wang, S. C. Gu, Y. Bai, S. Chen, N. Zhu, C. Wu, F. Wu, *J. Mater. Chem. A* **2015**, *3*, 22677; b) H. L. Wang, Y. Bai, S. Chen, X. Y. Luo, C. Wu, F. Wu, J. Lu, K. Amine, *ACS Appl. Mater. Interfaces* **2015**, *7*, 80; c) S. C. Gu, H. L. Wang, C. Wu, Y. Bai, H. Li, F. Wu, *Energy Storage Mater.* **2017**, *6*, 9.
- [234] G. Cohn, L. Ma, L. A. Archer, *J. Power Sources* **2015**, *283*, 416.
- [235] T. Gao, X. Li, X. Wang, J. Hu, F. Han, X. Fan, L. Suo, A. J. Pearse, S. B. Lee, G. W. Rubloff, K. J. Gaskell, M. Noked, C. Wang, *Angew. Chem., Int. Ed.* **2016**, *55*, 9898.
- [236] a) R. Y. Deng, M. Wang, H. Y. Yu, S. R. Luo, J. H. Li, F. L. Chu, B. Liu, F. X. Wu, *Energy Environ. Mater.* **2022**, *0*, 1; b) K. L. Zhu, C. Wang, Z. X. Chi, F. Ke, Y. Yang, A. B. Wang, W. K. Wang, L. X. Miao, *Front. Energy Res.* **2019**, *7*, 123; c) S. Dorfler, H. Althues, P. Hartel, T. Abendroth, B. Schumm, S. Kaskel, *Joule* **2020**, *4*, 539.
- [237] S. Walus, G. Offer, I. Hunt, Y. Patel, T. Stockley, J. Williams, R. Purkayastha, *Energy Storage Mater.* **2018**, *10*, 233.
- [238] H. Li, D. L. Chao, B. Chen, X. Chen, C. Chuah, Y. H. Tang, Y. Jiao, M. Jaroniec, S. Z. Qiao, *J. Am. Chem. Soc.* **2020**, *142*, 2012.
- [239] a) P. Zeng, C. Liu, X. F. Zhao, C. Yuan, Y. G. Chen, H. P. Lin, L. Zhang, *ACS Nano* **2020**, *14*, 11558; b) Z. S. Qiao, F. Zhou, Q. F. Zhang, F. Pei, H. F. Zheng, W. J. Xu, P. F. Liu, Y. T. Ma, Q. S. Xie, L. S. Wang, X. L. Fang, D. L. Peng, *Energy Storage Mater.* **2019**, *23*, 62; c) H. Y. Li, L. F. Fei, R. Zhang, S. L. Yu, Y. Y. Zhang, L. L. Shu, Y. Li, Y. Wang, *J. Energy Chem.* **2020**, *49*, 339.
- [240] J. He, A. Bhargava, A. Manthiram, *ACS Nano* **2021**, *15*, 8583.
- [241] R. J. Liu, C. Streb, *Adv. Energy Mater.* **2021**, *11*, 2101120.
- [242] a) R. F. Service, *Science* **2003**, *301*, 909; b) S. Bae, H. Kim, Y. Lee, X. Xu, J.-S. Park, Y. Zheng, J. Balakrishnan, T. Lei, H. R. Kim, Y. I. Song, Y.-J. Kim, K. S. Kim, B. Ozyilmaz, J.-H. Ahn, B. H. Hong, S. Iijima, *Nat. Nanotechnol.* **2010**, *5*, 574.
- [243] H. J. Peng, J. Q. Huang, Q. Zhang, *Chem. Soc. Rev.* **2017**, *46*, 5237.
- [244] G. Zhou, S. Wang, T. Wang, S.-Z. Yang, B. Johannessen, H. Chen, C. Liu, Y. Ye, Y. Wu, Y. Peng, C. Liu, S. P. Jiang, Q. Zhang, Y. Cui, *Nano Lett.* **2020**, *20*, 1252.



Linchao Zeng is a research assistant in Shenzhen Institutes of Advanced Technology, Chinese Academy of Sciences. He received a Ph.D. degree in 2016 from the University of Science and Technology of China. After obtaining his Ph.D. degree, he began to work as a postdoctoral researcher in Tsinghua University. His research interests mainly include synthesis and application of nanomaterials for lithium-ion batteries and sodium-ion batteries.



Guangmin Zhou is an associate professor in Tsinghua Shenzhen International Graduate School, Tsinghua University. He received his Ph.D. degree from Institute of Metal Research, Chinese Academy of Sciences in 2014 under the supervision of Prof. Hui-Ming Cheng and Prof. Feng Li, and then worked as a postdoc in UT Austin with Prof. Arumugam Manthiram during 2014–2015. After that, he was a postdoc fellow in the Department of Materials Science and Engineering at Stanford University with Prof. Yi Cui from 2015 to 2019. His research mainly focuses on the development of advanced energy-storage materials and devices.



Xue-Feng Yu received his Ph.D. degree in Physics from Wuhan University in 2008, and then worked at Wuhan University and City University of Hong Kong. He is currently a Professor and Director of Materials and Interfaces Center at Shenzhen Institute of Advanced Technology, Chinese Academy of Sciences. He leads an interdisciplinary research group focused on the synthesis and applications of nanomaterials. He has coauthored more than 100 publications in SCI-indexed journals with over 12 000 citations.